Title
Understanding Magnetism in Multiferroics

Author
Holcomb, Mikel Barry

Publication Date
2009

Peer reviewed|Thesis/dissertation

Understanding Magnetism in Multiferroics

by

Mikel Barry Holcomb

B.S. (Vanderbilt University) 2004
M.S. (University of California, Berkeley) 2006

A dissertation submitted in partial satisfaction of the

requirements for the degree of

Doctor of Philosophy

in

Physics

in the

Graduate Division

of the

University of California, Berkeley

Committee in charge:

Professor R. Ramesh, Chair
Professor Joel Moore
Professor Yuri Suzuki

Fall 2009

The dissertation of Mikel Barry Holcomb is approved:

Chair _____ Date: _____

Professor R. Ramesh

_____ Date: _____

Professor Joel Moore

_____ Date: _____

Professor Yuri Suzuki

University of California, Berkeley

Fall 2009

Understanding Magnetism in Multiferroics

by Mikel Barry Holcomb

Abstract

Understanding Magnetism in Multiferroics

by

Mikel Barry Holcomb

Doctor of Philosophy in Physics

University of California, Berkeley

Professor R. Ramesh, Chair

This dissertation details the study of electric and strain control of antiferromagnetism and ferromagnetism at room temperature using multiferroic $BiFeO_3$ thin films. Piezoelectric force microscopy and photoemission electron micrscopy techniques were used to correlate ferroelectric and antiferromagnetic domains. An angle-dependent dichroism intensity formula was established and applied to determine magnetic behavior. The effects of thickness and orientation on ferroelectric and magnetic properties in $BiFeO_3$ films were studied. These results were used in the making of a magnetoelectric-ferromagnet heterostructure in which electrically assisted exchange bias was observed. This toolbox of control parameters gives a very strong benefit for the making of new and improved devices, particularly in the computing industry where the traditional magnetic field controlled devices are reaching their limits.

Chair _____ Date: _____

Professor R. Ramesh

DEDICATIONS

There are a great number of people who have developed me into the scientist and teacher that I am today. I dedicate this dissertation to you. Let me point out a few of these people for whom I am particularly grateful.

I would like to thank my advisor Professor Ramesh whose never-ending passion for science has kept me motivated and encouraged me to push my limits.

I am grateful for the effort of many beamline scientists (Andreas Scholl, Jeff Kortright, Andrew Doran, Elke Arenholz, Arantxa Fraile-Rodriquez) whose expertise in their equipment and research field has allowed me the ability to quickly attain and analyze new experimental procedures. Andreas' tireless answering of so many of my questions has allowed exciting new science to take place.

I would like to thank so many teachers from high school (Henry County, Kentucky), undergraduate (Vanderbilt University), and graduate school for encouraging me to reach for the stars. Without your constant support, I may never have gained the self confidence that allows me progress in this fascinating field. Let me specifically thank Professor Sheldon (Vanderbilt) who encouraged my interest in undergraduate research by setting up interviews with the local professors. I was able to interview the professors and find out what research was right for me. I am very happy with my choice.

This leads me to thank my undergraduate advisor Professor Tolk. I appreciate his effort to fill in the background when others might say I was not yet ready for research due to still being too young. I am thankful for the experience he allowed me not only in the laboratory, but also dealing with grant writing and teaching. Also, there was nothing better than a party at the Tolk's house.

Another "teacher" I would like to thank is my mother. She taught me that I can do anything to which I put my mind. I appreciate her help in making my education possible even when it seemed above our means. She has always been available to me any time I have an issue which I seek her advice.

My husband should not be so far down on the list of people I would like to thank. He has allowed me not to go insane with his willingness to take care of a great deal of little things that pile up. He also has been gracious enough to let me practice important talks on him and to edit many of my writings. His help has allowed me to be much more efficient. He has also kept me very happy.

I would like to thank so many of my friends such as Seth, Steve-Steve, Dave R., Dave P., Joel, Allen, and Sarah for helping me learn how to talk to scientists not in my field and giving me much needed relaxation.

I am thankful to have had intriguing discussions with many scientists about my project and the future of the field. A few professors and scientists have gone out of their way to

have continued debate include Nicola Spaldin (UCSB), Joe Orenstein (UCB), Jo Stohr (Stanford), Jeff Kortright (ALS), and Robert Shelby (IBM Almaden).

There are many others that will go unnamed. Thank you for all of your support and guidance.

TABLE OF CONTENTS

LIST OF FIGURES

LIST OF SYMBOLS & ABBREVIATIONS

α – First order magnetoelectric coupling term

β – Higher order magnetoelectric coupling coefficient

γ – Higher order magnetoelectric coupling coefficient or interfacial energy

ε – Electric susceptibility

μ – Magnetic susceptibility

μ_0 – Vacuum permeability

μ_B – Bohr magnetron, equal to 9.274096 x 10-24 J/T

χ_e – Electric susceptibility

χ_m – Magnetic susceptibility

(x y z) – Miller indices for specific crystallographic plane

[x y z] – Miller indices for specific crystallographic direction

{x y z} – Miller indices for a family of equivalent crystallographic planes

<x y z> – Miller indices for a family of equivalent crystallographic directions

AEY – Auger electron yield

AFM – Antiferromagnet, Antiferromagnetic

ALS – Advanced Light Source

BFO – $BiFeO_3$

CMR – Colossal magnetoresistance

CoFe – $Co_{0.9}Fe_{0.1}$

E – Electric field

e^- – Electron

EB – Exchange bias

EELS – Electron energy loss spectroscopy

EXAFS – Extended x-ray absorption fine structure

F – Free energy of a system

Fe – Iron

FE – Ferroelectric

FM – Ferromagnet

H – Magnetic field

H_C – Coercive field

H_{EB} – Exchange bias field

HRTEM – High resolution transmission electron microscopy

IP – In-plane

L – Sampling depth

LSDA – Local spin density approximation

LSDA+U – Local spin density approximation plus a Hubbard U parameter

M – Magnetization

ME – Magnetoelectric

NEXAFS – Near-edge x-ray absorption fine structure

OOP – Out-of-plane

P – Percentage of ferroelectric contribution to dichroism in a multiferroic

PEEM – Photoemission electron microscopy

PFM – Piezoresponse force microscopy

PLD – Pulsed laser deposition

Q – Percentage of magnetic contribution to dichroism in a multiferroic

RSM – Reciprocal space map

SRO – $SrRuO_3$

STO – $SrTiO_3$

T_C – Ferroelectric or ferromagnetic Curie temperature

TEM – Transmission electron microscopy

TEY – Total electron yield

Ti – Titanium

T_N – Néel temperature of an antiferromagnet

XANES – X-ray absorption near-edge spectroscopy

XAS – X-ray absorption spectroscopy

XLD – X-ray linear dichroism

XMCD – X-ray magnetic circular dichroism

XMLD – X-ray magnetic linear dichroism

XRD – X-ray diffraction

ACKNOWLEDGEMENTS

I would like to extend my deepest thanks to my qualifying exam committee Professors Francis Hellman (Chair), Joel Moore and Yuri Suzuki and to Professors Joel Moore and Yuri Suzuki for serving on my dissertation committee.

I would like to thank all of the people in the Ramesh group. My work would not be possible without the assistance of many of my coworkers. Specifically, I thank Eddie Chu, Tommy Conry, Chan-Ho Yang for growing samples for me. I thank Lane Martin for not only growth of my samples but also of my scientific thought. I thank Helen He, Kate Jenkins, and Sanni Kehr for working late nights with me. I also own much credit to everyone who provided essential PFM support—Helen He, Nina Balke, Padraic Shafer, Jan Seidel, Pei-Ling Yang, and Florin Zavaliche (now at Seagate). Let me also thank post-docs Tong Zhao (now at Seagate) and Martin Gajek for passing on your expertise.

My research would have been much less fruitful and quite dull without the interaction with many collaborators. Since no man is an island nor can know everything, only through collaboration can we expect to answer the important questions of tomorrow. Throughout this work, data collected with the help of such collaborations will be presented. I would therefore like to specifically acknowledge the efforts of the following individuals and groups for help with measurements and understanding. Andreas Scholl, Jeffery B. Kortright, Elke Arenholz, and Andrew Doran from the Advanced Light Source at Lawrence Berkeley National Laboratory for help with experiments and interpretation

concerning work done on $BiFeO_3$, $PbZrTiO_3$, $LaSrMnO_3$, and many other materials. Arantxa Fraile-Rodriguez, Frithjof Nolting, Loic Joly, and Cinthia Piamonteze at the Swiss Light Source, Paul Scherrer Institut for help with photoemission studies on $Co/BiFeO_3$ and $BiFeO_3$ crystals and thin films. Amit Kumar and Professor Venkat Gopalan at Pennsylvania State University for fruitful discussions and interactions concerning $BiFeO_3$ as well as continued support and advice involving second harmonic generation. Nicola A. Spaldin at the University of California, Santa Barbara for priceless discussions about $BiFeO_3$, tireless modeling assistance, and professional development advice. Finally, and most importantly, Professor R. Ramesh – for your insistent guidance whether or not I asked for it or wanted it. You have made me scientifically and personally stronger than I ever thought possible.

Many thanks to the Department of Defense NDSEG Program for supporting the first three years of my studies and for support from the SRC NRI Hans J. Coufal Fellowship for support in my last two years. This work has been supported by the Director, Office of Basic Energy Sciences, Materials Science Division of the U.S. Department of Energy under Contract No. DE-AC02-05CH11231 and previous contracts, ONR-MURI under Grant No. E21-6RU-G4 and previous contracts, and the Western Institute of Nanoelectronics program.

Chapter 1: Complex Oxides and Their Complex Behavior

This chapter discusses some of the interesting properties and applications of complex oxides. Material order parameters that can be controlled, such as magnetism and ferroelectricity, are presented. Bismuth ferrite (BFO) is introduced as a system that has both order parameters and the potential for coupling between these properties. The central focus of this work--how to probe and control magnetism in model BFO films--is raised in terms of its greater impact on everyday life and the world of materials science. Finally, this chapter ends with a brief summary of the organization of this dissertation.

1.1 Complex Oxides

It is not common knowledge that complex oxides are an integral part of our daily lives. Complex oxides are used to reduce the toxic emission in our automobiles, allow us to check on the health of unborn babies by ultrasound, improve the performance of our computers and video game consoles, and much more. In addition to being among the most abundant minerals on earth, complex oxides give some of the most varied and interesting properties,[1] demonstrated by the table in Figure 1. These include their use as dielectric and superconducting materials. Some complex oxides exhibit colossal magnetoresistance (CMR), where enormous variations in resistance are produced by small magnetic field changes, which would be useful for new technologies such as read/write heads for high-capacity magnetic storage and spintronics.[2] Magnetic and ferroelectric properties are commonly exploited in power generation and computing.

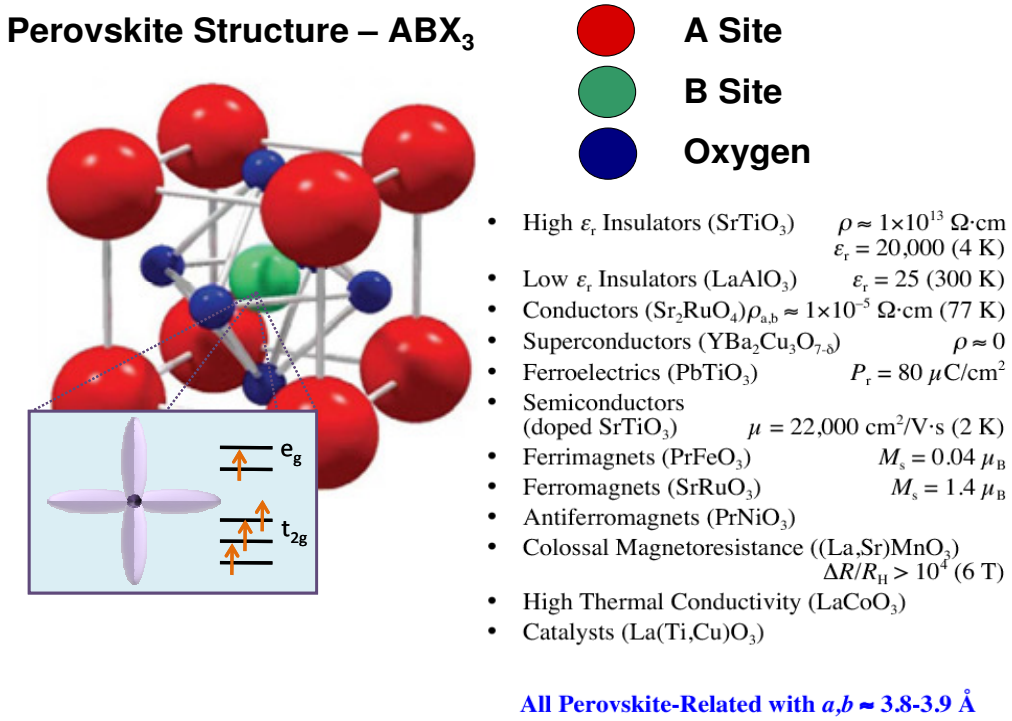

Figure 1 - Perovskite structure and variety of properties

Only recently has the research in the field of complex oxides flourished because these materials were long thought to be too complex to fully understand. This complexity comes from the strong coupling of charge, spin, and lattice dynamics, often resulting in very full phase diagrams.[2-3] Though the coupling may lead to complex behaviors, the actual structure may be much simpler to describe. One common structure of complex oxides is the perovskite form in Figure 1, where the A and B sites are typically different cations and X is an anion (usually oxygen) that bonds to both. In several complex oxide perovskites, this oxygen arrangement gives rise to a crystal field potential, hinders the free rotation of the electrons and the orbital angular momentum by introducing the crystal field splitting of the d orbitals.[3] For example, the crystal field splitting illustrated in Figure 1 shows the case for $LaMnO_3$ where Mn^{3+} has a d^4 configuration, meaning that there are 4 electrons (represented by arrows) in the d orbitals. Due to Hund's rule, all of these spins point in the same direction, resulting in a total spin of 2. This is only the very beginning of the story leading to the complexity in these systems. For a further discussion of the detailed physics involved in this broad class of materials, see Tokura *et. al*.[3]

1.2 Controlling Order Parameters

1.2.1 Ferroelectricity

A particularly interesting subclass of complex oxides is materials with controllable order parameters; for example, piezoelectric materials exhibit a response when in the presence of an electric field, as demonstrated by a linear (dielectric) response in Figure 2a. Ferroelectrics are a form of piezoelectric that remains polarized after the external electric

field is removed.[4-5] As is evident in the hysteresis loop in Figure 2b, these materials have a spontaneous polarization at zero field, which can be changed by application of an opposing electric field.[5-6] Thus, some companies have recently taken advantage of this hysteresis behavior to build low energy memory devices.[7] This hysteresis loop and resulting behavior will disappear when the material goes above its ferroelectric critical temperature T_c. Ferroelectrics are also commonly used to make tunable capacitors with high capacitance, which make excellent sensors for use in ultrasound systems, high quality infrared cameras, fire and vibration sensors, and even fuel injector.[8]

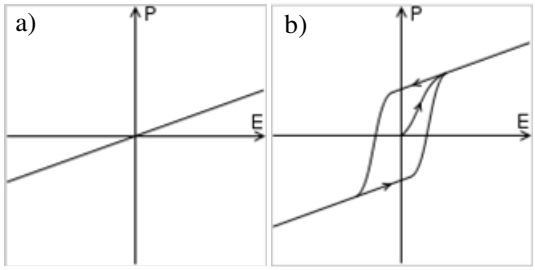

Figure 2 - Electric field dependence for a) dielectric and b) ferroelectric materials

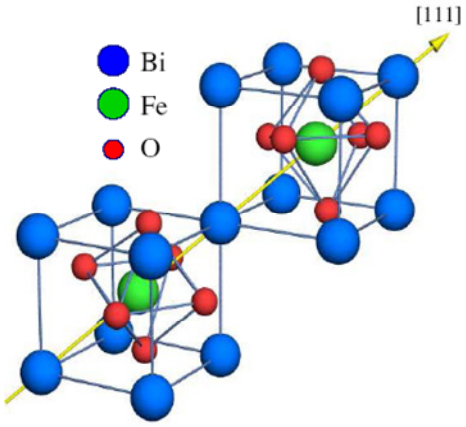

Figure 3 - Rhombohedral structure of BFO at room temperature

One ferroelectric that has recently received a great deal of attention is bismuth ferrite ($BiFeO_3$ or BFO). BFO is a rhombohedrally-distorted perovskite ferroelectric with large intrinsic polarization[9] and eight possible polarization directions occurring along the pseudocubic 111> body diagonals, one of which is shown in Figure 3. Growth techniques (discussed in Appendix A) have been established to easily select as many polarization directions as are desired for the application or experiment—all eight, four, two, or even a single ferroelectric domain. Growth techniques also allow a wide range of variance in other material parameters, such as strain, thickness, and

orientation. The ferroelectric ordering temperature of BFO is also quite high (~1100K), meaning that this material can perform well within a large range of temperatures.

The ferroelectric properties of BFO are most commonly studied by piezoelectric force microscopy (PFM). PFM is a well-established technique that can image the in-plane and out-of-plane projections of ferroelectric directions and can also switch the out-of-plane (OOP) polarization direction.[10-11] Thus, the polarization direction(s) of each of the domains can be easily distinguished and compared to magnetic measurements. For more details about PFM, please see Appendix B. Figure 4 is a typical in-plane image of BFO thin films taken by PFM. For BFO thicknesses ~ 100 nm, the width of the ferroelectric domains is ~ 150 nm. The white, brown, and black contrasts correspond to the in-plane projection of the ferroelectric domains. The domain stripes align along [100] and the projection of the ferroelectric directions are 45 degrees from the walls—pointing up, down, left and right in Figure 4.[12]

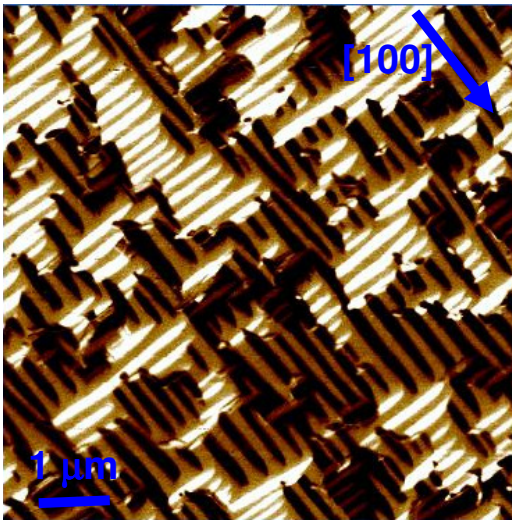

Figure 4 - In-plane PFM image of BFO thin film

1.2.2 Magnetism

Another order parameter that can be controlled is magnetism. The most commonly used and understood magnetic order is ferromagnetism. It parallels ferroelectricity; whereas a ferroelectric has a spontaneous polarization that can be changed by an applied electric

field, a ferromagnet has a spontaneous magnetization that can be controlled by an applied magnetic field. Ferromagnets are used for the memory in our computers, in power generation and any time one needs a permanent magnet, such as on a refrigerator. There are a large variety of methods for studying ferromagnets, such as superconducting quantum interface devices, neutron studies, and x-ray magnetic circular dichroism.[13]

A form of magnetism that is more difficult to study is antiferromagnetism. An antiferromagnet has no net magnetic moment. For example, BFO—in addition to its ferroelectric properties—is also a G-type antiferromagnet, meaning that the individual moments on each Fe-ion are aligned parallel within the pseudocubic {111} and antiparallel between adjacent {111}. In BFO, there is a weak canting of ~1 degree between the two sublattices (turned off in Figure 5a but on in Figure 5b), resulting in a small magnetization of ~0.05 μ_B per unit cell.[14] This small canting is allowed by the Dzyaloshinskii-Moriya interaction,[14] which results from the combined action of exchange interaction and spin-orbit coupling. Though antiferromagnets are less thoroughly understood, they still find valuable application in computing in the pinning of ferromagnetic directions called exchange bias. This concept will be discussed in Chapter 6.

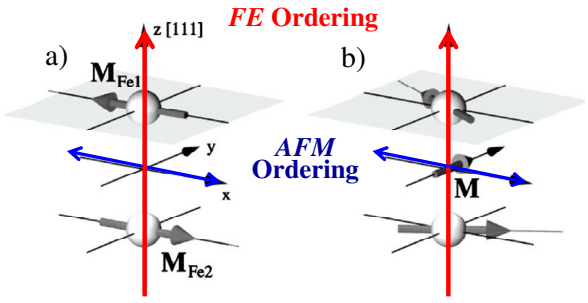

Figure 5 - Magnetic order in BFO with respect to the [111] ferroelectric direction

Since most magnetic characterization methods rely on measuring the net magnetic moment, there are very few techniques to study antiferromagnetism. Most of the techniques that do study antiferromagnetism are limited to averaging the magnetic information over the entire sample. Since neutrons are magnetic, and are able to easily penetrate through samples, reflected neutrons can be used to provide information about the magnetic properties of individual layers or depth profiling. Second harmonic generation probes the magnetic symmetry of antiferromagnetic materials, but averaged over a large spot size. One of the few techniques that allows for the measurement of local magnetic information is x-ray absorption studies; this method will be covered in greater detail in Chapter 2.

1.2.3 Multiferroics and Magnetoelectrics

A particularly interesting case occurs when both ferroelectricity and magnetism are present in the same material, creating one of a class of materials known as multiferroics. A multiferroic is defined as a material that has at least two of the three following properties—ferroelectricity, ferromagnetism, and ferroelasticity.[15-16] Similar to the other two order parameters, a ferroelastic has a spontaneous deformation that can be changed by an applied stress. Multiferroics often come from the group of the perovskite transition metal oxides, including rare-earth manganites and ferrites (e.g. $TbMnO_3$ and $HoMn_2O_5$). For example, BFO is a multiferroic that has all three ferroic properties at room temperature. Therefore, BFO has been used as a model to study the interesting physics and possible application that results from this trifecta of properties. In fact, BFO is the only known material that is both magnetic and ferroelectric at room temperature, making

it an ideal candidate for devices. After some thought, this scarcity of other room temperature multiferroics is not terribly surprising. Magnetic behavior requires partially filled d electrons, whereas ferroelectrics typically have empty or filled d orbitals.[17] Ferromagnets are often metallic, but ferroelectrics are insulators by definition. This point illustrates why antiferromagnetic ferroelectrics are more common.

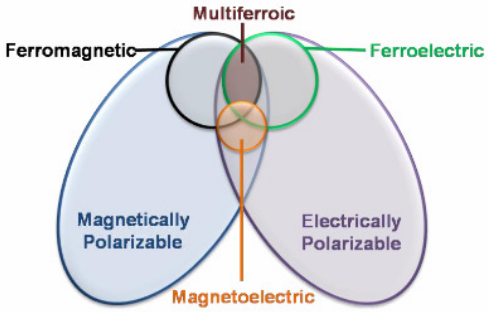

Figure 6 – Correlation of ferroelectric and magnetic ordering (adapted from Ref. 19)

One of the interesting results from the combination of both ferroelectricity and magnetism is the possibility for coupling between the order parameters, called magnetoelectric coupling.[18] Not all multiferroics exhibit this coupling and not all magnetoelectrics are multiferroic, however, there is some overlap between the two classes as demonstrated in Figure 6.[19] When this coupling exists, there exists the potential to control the magnetic properties of the sample with an electric field or the electric properties with a magnetic field. Mathematically, this can be seen from the expansion of the free energy for a material

$$F(\mathbf{E}, \mathbf{H}) = F_o - P_i^S E_i - M_i^S H_i - \tfrac{1}{2}\varepsilon_o\varepsilon_{ij}E_iE_j - \tfrac{1}{2}\mu_o\mu_{ij}H_iH_j - \tfrac{1}{2}\beta_{ijk}E_iH_jH_k - \tfrac{1}{2}\gamma_{ijk}H_iE_jE_k - \ldots \quad (1)$$

where **E** and **H** are the electric and magnetic field vectors, respectively [Fiebig]. Derivatives of the free energy give both the polarization

$$P_i(\mathbf{E}, \mathbf{H}) = -(\partial F/\partial E_i) = P_i^S + \varepsilon_o\varepsilon_{ij}E_j + \alpha_{ij}H_j + \tfrac{1}{2}\beta_{ijk}H_jH_k + \gamma_{ijk}H_iE_j - \ldots \quad (2)$$

and the magnetization

$$M_i(\mathbf{E}, \mathbf{H}) = -(\partial F/\partial H_i) = M_i^S + \mu_o\mu_{ij}H_j + \alpha_{ij}E_i + \tfrac{1}{2}\beta_{ijk}E_iH_j + \gamma_{ijk}E_jE_k + \ldots \quad (3)$$

where ε and μ are the electric and magnetic susceptibilities and α is the induction of magnetization by an electric field or polarization by a magnetic field. Though higher orders of ME effects are possible, the linear ME effect (α) is generally much larger. For example, bulk BFO is known to have no linear ME effect, due to a canceling of the magnetic order due to a spin spiral. In thin films, however, it is possible to discourage this canceling by proper control of the growth parameters, thus allowing a linear ME effect. This could potentially provide a dramatic improvement to the ME effect in BFO thin films.

Magnetoelectric coupling has many potential applications in computing, sensors, and energy scavenging.[20] For example, the 0's and 1's that make up the memory of computers are just magnetic domains. The magnetization direction within each domain is written by application of a magnetic field. However, there are many problems with using magnetic fields if we are going to continue to make computers smaller, faster and more energy efficient. Magnetic fields require a great deal of power to generate, and these fields can also be difficult to localize, limiting the minimum size of the bit and the memory density. Additionally, the speed that these magnetic fields are applied can only be reduced so far, since the ultrafast motion of spins excited by field pulses shorter than thermal relaxation times (~100 ps) are poorly understood. If one instead uses a material where the magnetism can be controlled electrically, many of these issues can be resolved.

1.3 Understanding and Controlling Magnetism

The goal of this work is to understand and control magnetism in BFO thin films. Though the magnetic order of bulk BFO has been well characterized, little work on thin films was attempted. This thesis describes how x-ray absorption measurements where used to determine the specific magnetic order on a range of thin films and study the effect of this order on a ferromagnetic layer on top of BFO. This work will further the understanding of magnetic ordering in antiferromagnets and their influence in exchange bias. The thesis is organized as described below. Chapter 2 details the physics behind the x-ray absorption technique utilized in this study. Chapter 3 describes how we and other groups were able to prove that not only are the magnetic and ferroelectric domains in both thin films and crystals of BFO coupled, but that they continue to be after perturbation with an electric field. Chapter 4 discusses how we can change the magnetic properties of BFO through film thickness and strain. The presented measurement techniques are applicable to understanding order parameters in a wide range of materials that are often difficult to measure. Chapter 5 investigates the role of different crystallographic orientations and how they affect both the understanding and control of the magnetic order parameter. In Chapter 6, the use of this collection of control parameters to electrically control ferromagnetism through coupling a ferromagnetic to magnetoelectric BFO thin films is explored. Chapter 7 serves as a summary chapter recapping the findings presented in each chapter and proposing future work in this area. Appendix A covers some of the important details concerning the growth of BFO films. Appendix B focuses on how PFM is used to understand the ferroelectric nature of BFO and other films.

Chapter 2: The Technique Behind Probing Magnetism—X-ray Absorption

This chapter explores the history, importance and physics behind x-ray absorption and dichroism. X-ray absorption spectroscopy, total electron yield, photoemission electron microscopy techniques are discussed. Advantages and disadvantages of several photoemission electron microscopes utilized in this work are compared. The origin of circular and linear dichroism is explored through example in NiO systems. Finally, the power of PEEM is demonstrated by the application of both circular and linear dichroism to study coupling between different materials.

2.1 Synchrotron Radiation History

Arguably the strongest resource for material characterization was not even originally intended for that purpose. A synchrotron is a type of particle accelerator which utilizes magnetic and electric fields to accelerate particles around nearly circular paths to speeds extremely close to the speed of light. Particle physicists have used particle accelerators to collide particles and learn about the dynamics and structure of matter, space and time. The problem (and opportunity) with accelerating particles to such high speeds is that the particles give off large amounts of radiation in the form of photons. Ivanenko and Pomeranchuk published their 1944 calculations showing that these energy losses would limit the energy obtainable by early particle accelerators, called betatrons. This predicted limitation prompted scientists such as Blewett to search for these energy losses, but little success over the years lead many to believe synchrotron radiation was not the source of the loss. A clever design by General Electric on another kind of particle accelerator, called a cyclotron, allowed the first observation of synchrotron radiation. The doughnut-shaped electron tube was made transparent in order to allow technicians to test an intriguing property for this type of accelerators called bunching. Instead, a bright arc of light was observed, which General Electric researchers quickly realized was coming from the electron beam. Langmuir is credited as first recognizing the arc as synchrotron radiation. After its discovery, several facilities introduced small beamlines to take advantage of the energy losses that were once considered a nuisance. Though synchrotron radiation was initially only a parasitic branch of particle accelerators claiming only a small percentage of the available beamtime, today dedicated facilities exist to foster the

growing demand for synchrotron measurement. It is intriguing to realize that even though synchrotron radiation is as old as the stars—for example causing the light we see from the Crab Nebula—only in the last several decades have we recognized and manipulated its opportunities.[21]

2.2 Polarized X-rays

The radiation that comes from the synchrotron has several advantages: it has much higher flux than can be achieved by standard laboratory techniques (also many orders of magnitude greater than the sun), its energy range is tunable within a ~1000 eV range, and the photons are polarized. There are two common methods to collect these photons: using a bending magnet or an undulator. Since both were employed for the following measurements, the differences between the two techniques should be considered. Bending or dipole magnets are commonly used in particle accelerators to inject or eject particles into or out of the accelerator. Bending magnets are cheaper to construct than undulators, though their flux is generally four orders of magnitude less than would be achieved from an undulator. Bending magnets can produce light that is linearly polarized and right or left circularly polarized. An elliptically polarizing undulator (EPU) produces these three polarizations as well; however, it can also rotate the light polarization by ninety degrees in fine steps if desired. Though this rotation of the light polarization is vital for some of the measurements presented in Chapter 4, many of the other measurements can be obtained without an EPU.

2.3 Experimental Techniques

2.3.1 X-ray Absorption Spectroscopy

One of the techniques that take advantage of the polarized x-rays provided by bending magnets and undulators is x-ray absorption spectroscopy (XAS), which is used for molecular and condensed matter physics, biology, chemistry, earth science and more. X-ray absorption spectra are taken by varying the energy of incident photons in a range (0.1 – 100 keV) where core electrons are excited. Depending on the quantum number (n=1, 2, and 3) of the excited electron, the spectra will have different names, respectively the K-, L-, and M-edges. This work will focus on the excitation of 2p electrons or the L-edge. There are two regions of XAS spectra that are commonly utilized. This work makes use of the dominant features called XANES (X-ray Absorption Near-Edge Spectroscopy) or NEXAFS (Near-edge X-ray Absorption Fine Structure) which, when used in combination, provide information on the local electronic states and their modification by local chemistry. The EXAFS (Extended X-ray Absorption Fine Structure) region is above the XANES region and occurs whenever the absorbing atom is closely surrounded by other atoms. For example, noble gases and monatomic vapors will exhibit no EXAFS. The EXAFS can provide radial locations, coordination numbers, atomic type differentiation, and disorder estimates for near neighbors surrounding the central absorbing atom.

2.3.2 Total Electron Yield

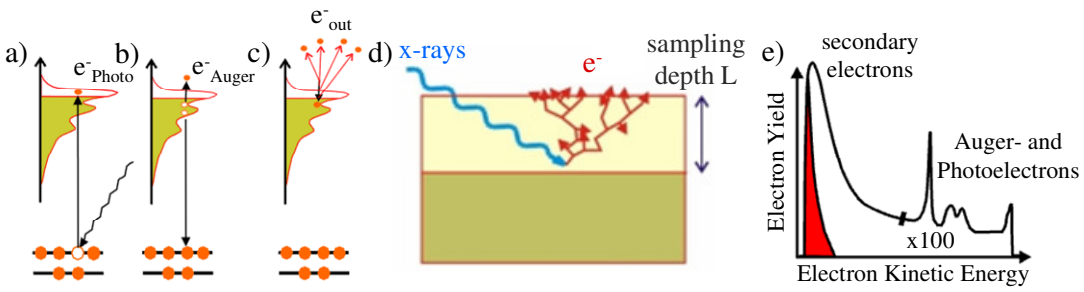

Figure 7 - Total electron yield description. a)-c) illustrate the excitation and decay of electrons in TEY. d) One x-ray creates several secondary electrons within the sampling depth L. e) These secondary electrons dominate the TEY intensity. (adapted from Ref. 22)

NEXAFS spectra and images are gathered by a technique called total electron yield (TEY), which is visualized in Figure 7. Instead of directly measuring the absorbed x-ray intensity, the photoelectrons that are created by the absorbed x-rays are observed. Absorption takes place when the core electrons are excited to empty states above the Fermi level (Figure 7a). These excited photoelectrons recombine with the core states by emitting a primary Auger electron (Figure 7b), with the intensity of these Auger electrons being a direct measure of the x-ray absorption. Auger electrons are used in a similar, extremely surface sensitive (too much so for some purposes) technique called Auger electron yield (AEY). Following the primary Auger electron emission, the photoelectron and Auger electron can be excited above the vacuum level—and thus emitted off of the sample—or lose energy through inelastic scattering due to their small mean free path (Figure 2c). In the latter case, a large number of secondary electrons are created for each photoelectron (Figure 2d); these secondary electrons dominate the TEY intensity as seen in Figure 2e. Electrons formed deep in the sample lose much of their energy through multiple scattering events and do not contribute significantly to the TEY. Thus, the

sampling depth for TEY is approximately ten nanometers, or five times greater than that of AEY measurements.[22]

2.3.3 Photoemission Electron Microscopy

Photoemission electron microscopy (PEEM) is a technique for collecting the TEY that spatially displays the intensity map of the collected photoelectrons. Though cathode-lens microscopy was introduced in the 1930s by Bruche et. al.,[23] PEEM has become a practical tool only recently due to current technological developments.[24] Much was learned from Bauer et. al.,[25] whose work in the very similar technique of low energy electron microscopy (LEED) spurred further growth with PEEM. The availability and increased use of high performance synchrotron radiation in the late 1980s, the development of ultrahigh vacuums in emission microscopy, and the success of electron yield based absorption spectroscopy were all helpful to the PEEM proposal of Tonner and Harp[26] and Engel et al.[27] a few years later.

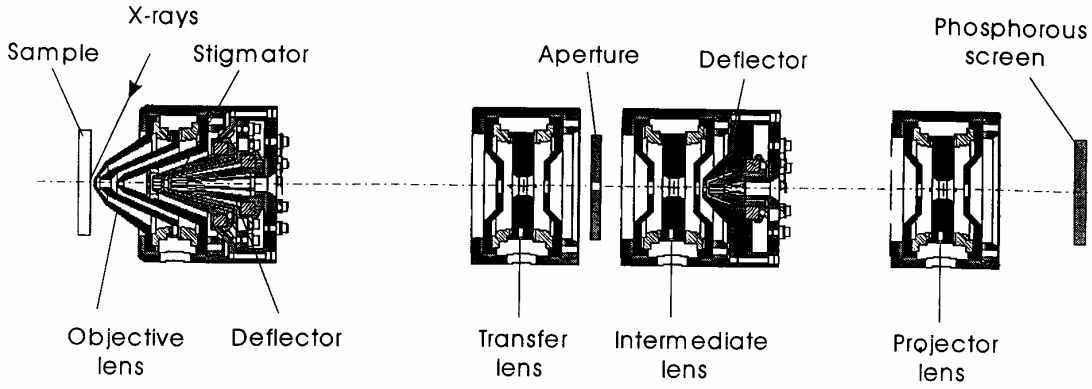

Figure 8 - Electron-optics of PEEM2 at the ALS

In PEEM measurements, the radiation of monochromatic x-rays with energies larger than the work function of the material of interest cause the emission of photoelectrons off of

the sample's surface. These electrons are accelerated into an electron-optical imaging device by an electric field. The optics (including objective, transfer, intermediate and projector lens) are used to image electrons onto a phosphor detector that converts them into visible light, which is finally read by a CCD camera. Figures 8 and 9 show the optical layout of beamline 7.3.1 at the Advanced Light Source (ALS) and the PEEM2 setup, respectively.[28]

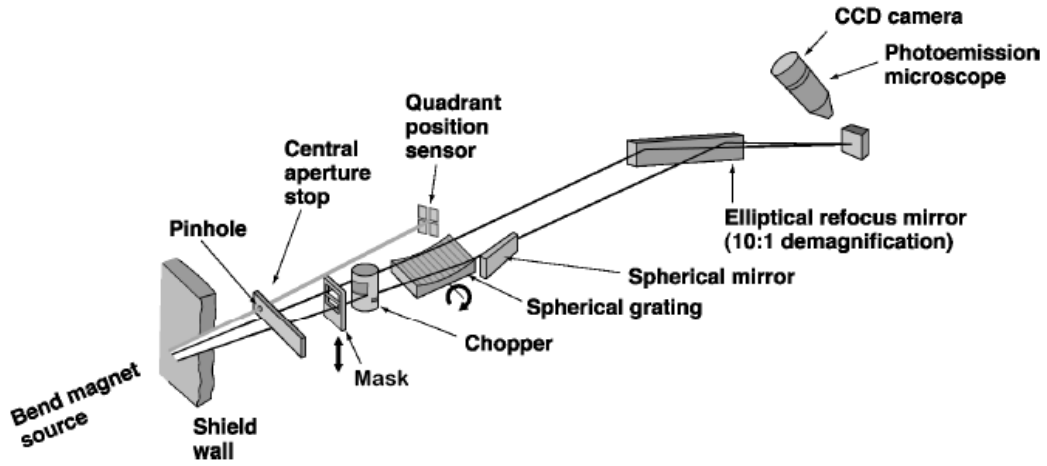

Figure 9 - Beamline setup at 7.3.1 at ALS

The PEEM work presented was completed at three different beamlines. PEEM2 was the only available PEEM for the first half of the work. This PEEM, which lies on the end of a bending magnet, has low flux, low resolution (~100 nm), and only horizontal linear light polarization. Later, access to the PEEM at the Swiss Light Source (SLS) allowed both sample and light polarization rotation, although slightly lower resolution (~150nm). Finally, an upgraded PEEM was brought online at the ALS (PEEM3). This PEEM has light polarization rotation and resolution down to ~20 nm, but access to it has been limited due to both great interest by the scientific community and several technical issues.

When planning experiments, careful attention was made to select the correct PEEM for the purpose, since they all have their own advantages and disadvantages.

2.4 X-ray Absorption Line Shape

2.4.1 The Golden Rule and Selection Rules

The importance of PEEM is intimately linked with the importance of XAS. Though XAS and PEEM do not offer the wonderful spatial resolution of some other techniques—such as transmission electron microscopy—they do present the ability to nondestructively measure magnetic moments with elemental and chemical specificity. The origin of this sensitivity is the conservation of energy and angular momentum. The x-ray absorption cross section for a material is governed by Fermi's Golden rule:

$$| < f | ez | i > |^2 \, \delta(E_f - E_i - \hbar\omega) \qquad (4)$$

where ez is the dipole operator. For the transition from the initial state $| i >$ to the final state $| f>$ to occur, the energy of the incoming x-ray has to be equal to the energy difference between two possible electronic states. This is energy conservation. We can also determine the intensity of the transition by calculating $|< f | H | i > |^2$, where H is the system's Hamiltonian. This can be calculatedly exactly, if the initial and final wave functions are known. But even in general, we can gain information as to the possible transitions from the symmetry of the dipole operator and its exchange properties with the spin operator S and the angular momentum L derived by spin-orbit coupling. For an unpolarized x-ray, absorption only occurs at $\Delta S = 0$, $\Delta L = \pm 1$. Only optical transitions that do not change the spin of the system but do change the angular momentum by one

are observed. This limits the number of possible transitions. There is another set of transition rules for polarized x-rays which are more important for the study of magnetic materials: the electronic states in these systems are not evenly populated and have different orientations, causing a dichroism effect. Dichroism refers to changes in the absorption of passing polarized light of different directions. The origin of the dichroism effect can be anisotropies in the charge or the spin in the material. The latter case is magnetic dichroism, which has been used to study magnetic materials for over a century in the magnetic optic Kerr effect. However, using x-rays to investigate this dichroism is a more recent approach.

2.4.2 Elemental Specificity

Additional advantages of XAS and PEEM include submonolayer surface sensitivity, the capability to investigate many nanometers of the surface of a material when combined with x-ray magnetic dichroism, and the ability to identify elements and their chemical state.[24] The usefulness of PEEM in elemental identification is due to the fact that the electron binding energy is highly dependent on the charge of the nucleus; even though the absorption line shapes are similar for several elements, they can be differentiated by the energy at which they occur. This can be seen in Figure 10, which shows the x-ray absorption spectra at

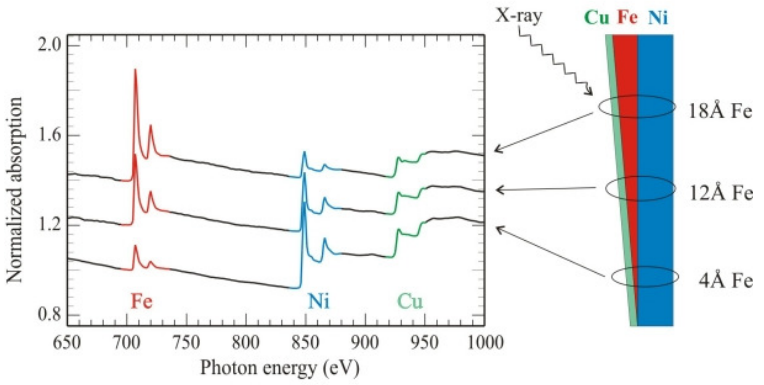

Figure 10 - Plot of total electron yield for wedge Cu/Fe/Ni sample[22]

various points along a wedge of copper, iron, and nickel. As the iron layer thickness is increased, the iron signal increases since there is more iron to probe, while the nickel signal decreases because of the limited electron escape depth of the TEY technique. The copper layer, which is above the iron layer, produces a constant signal, reflecting its constant thickness. X-ray absorption spectroscopy provides information on the chemical environment of the atoms and their magnetic state, since core electrons are excited in the absorption process into empty states above the Fermi energy. The electronic and magnetic properties of the empty valence levels are therefore probed.

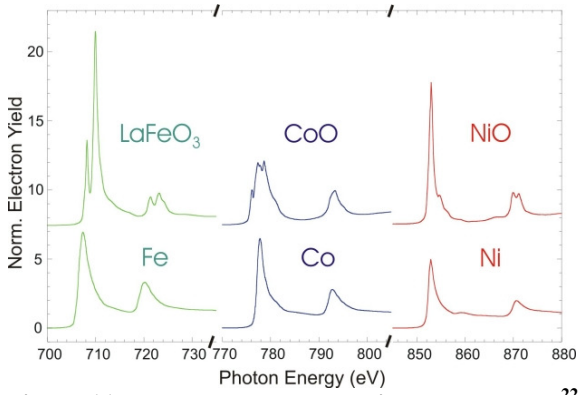

Figure 11 - L-edge x-ray absorption edge spectra[22]

The L-edge x-ray absorption edge spectra of Fe, Co, and Ni in the metallic as well as in an arbitrary oxidation state are shown in Figure 11. Magnetic properties of these materials are largely determined by the 3d valence electrons. The two principle peak clusters are the L_3 (left) and L_2 (right) absorption edges. L-edge absorption studies (2p to 3d transitions) best determine the d-shell properties, since x-ray absorption spectra are governed by dipole selection rules. The two spectra peaks originate from the spin orbit interaction of the 2p core shell, and their total intensity is proportional to the number of empty 3d valence states. The width of the empty d-bands can be determined by the distance between the metal spectra peaks (roughly 15 eV). Oxides exhibit a considerable amount of fine structure in their spectra, called multiplet structure. The reason for this is

that the empty oxide states are more localized than metal states and their energies are determined by crystal field and multiplet effects. Origins of multiplet effects are the spin and orbital momentum coupling of different 3d valence holes or electrons in the electronic ground state and the coupled states formed after x-ray absorption between the 3d valence holes and the 2p core hole.[28]

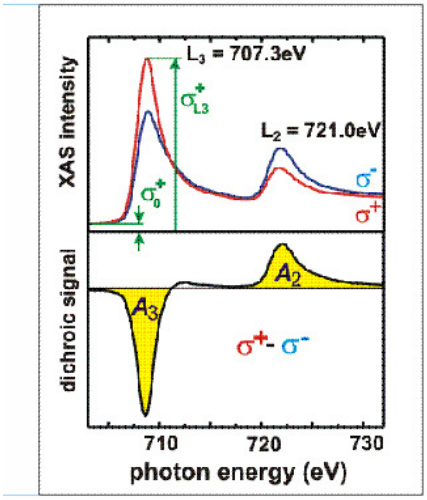

Figure 12 - Typical Fe XAS and XMCD[22]

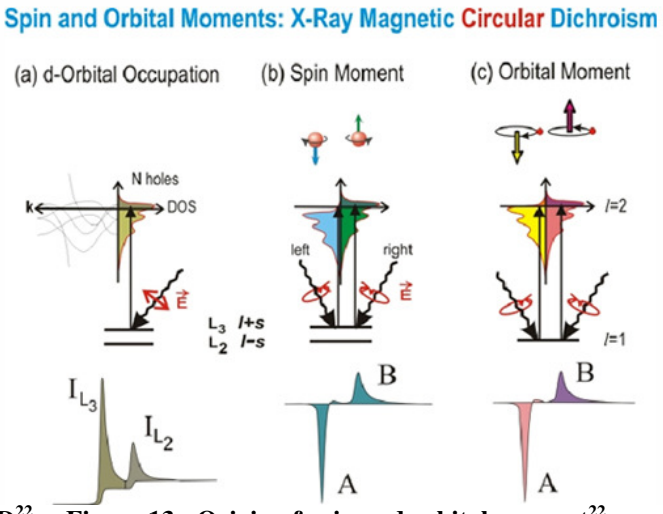

Figure 13 - Origin of spin and orbital moment[22]

2.4.3 X-ray Magnetic Circular Dichroism

Van der Laan predicted circular and linear x-ray magnetic dichroism (XMCD and XMLD) in 3d transition metals in 1991.[29] The TEY-XAS for two circular polarizations in red and blue for the L edge of iron is shown in Figure 12. The difference between the left and right circular absorption lines gives the XMCD signal. The areas under the A_2 and A_3 curves are a measure of the magnetic polarization with respect to the direction of the incident light. XMCD attracted more attention once the so-called sum-rules were established; these rules relate the intensity of the dichroism to the orbital and spin moments and the spin density.[30] One can even determine the absolute magnetic moments per atom if the number of holes is known.

The concepts behind the sum rules for XMCD spectroscopy are demonstrated in Figure 13.[28] The first sum rule relates the number of empty d states (maximum of ten) to the total intensity of the L_3 and L_2 resonances. The spin dependency of x-ray absorption can be used to determine the difference between the number of spin up and spin down holes (the absence of these electrons), and the spin imbalance of spin up and spin down electrons of a magnetic material gives rise to a spin moment. Incident left or right circularly polarized photons transfer angular momentum to excited photoelectrons, which take this momentum as spin or angular momentum or a combination.[28] If the photoelectron came from a spin-orbit split level, such as $p_{1/2}$ which is related to the L_2 edge, the partial or full transfer from angular momentum to spin occurs due to spin-orbit coupling. There is an opposite contribution for left circularly polarized photons with respect to right circularly polarized photons, meaning photoelectrons of opposite spins are created. Spin polarization will be opposite in the L_2 and L_3 edges since spin-orbit coupling in $p_{1/2}$ and $p_{3/2}$ are opposite. Electric dipole transition selection rules do not allow photoelectrons excited to d hole states from p shells to change spin, and thus the transition intensity is proportional to the number of d holes of the desired spin. The dichroism effect is maximized when the signal when the magnetization direction and photon spin are parallel is compared to when they are antiparallel. Through sum rules, the L_2 and L_3 intensities and differences can be linked to the number of d holes and the size of the spin and orbital magnetic moments. Additional information on the spin and orbital anisotropies of the material[31] is determined by changing the angle of the applied magnetic field relative to the sample.

2.4.4 X-ray Magnetic Linear Dichroism

Circular dichroism provides magnetic information for ferromagnetic materials, but gives no signal or data for antiferromagnetic materials. As mentioned before, very few techniques—particularly ones that provide information on the spin orientation—are available for antiferromagnets. X-ray magnetic linear dichroism (XMLD), which is a similar technique to XMCD, was developed by van der Laan in the 1980s and is best understood by example. Hendrik Ohldag et al. of the Stanford Synchrotron Radiation Laboratory investigated antiferromagnetic domains of an ultra thin layer of NiO on argon (100) and gold (111).[32-33] This was first done using the BESSY II storage ring in Berlin, but the experiment was later confirmed and improved upon using the PEEM2 system, as will be discussed in the next example. NiO is a G-type antiferromagnet, which means that it aligns ferromagnetically along its 111 planes and antiferromagnetically between adjacent planes. There are four different domains associated with the four different 111 planes, which split up further due to the threefold symmetry of the 111 planes. Twelve domains are characterized by antiferromagnetic axis A, which points parallel to the difference of the sublattice magnetizations.

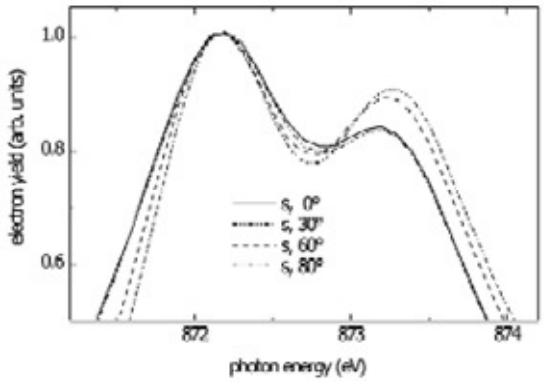

Figure 14 - L_2 linear Ni edge[32]

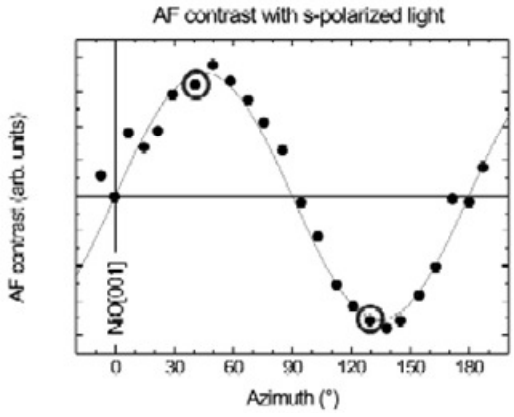

Figure 15 – Contrast vs. azimuthal angle[32]

Figure 14 shows the TEY of the nickel L_2 edge XMLD spectra for a 30 monolayer thick film. The XMLD effect is angle-dependent due to the preferential orientation of the antiferromagnetic axis A, which can be seen from the signals at different azimuthal orientations (Figures 14 and 15). In this case, peak A is larger than B when the electric field of the incident x-rays (E) is perpendicular to A, and smaller when parallel, as in many other films. As completed in Figure 16, AFM domains can be observed by dividing a PEEM image acquired at peak B by the image taken at peak A.[34] This division of images cancels most background noise.

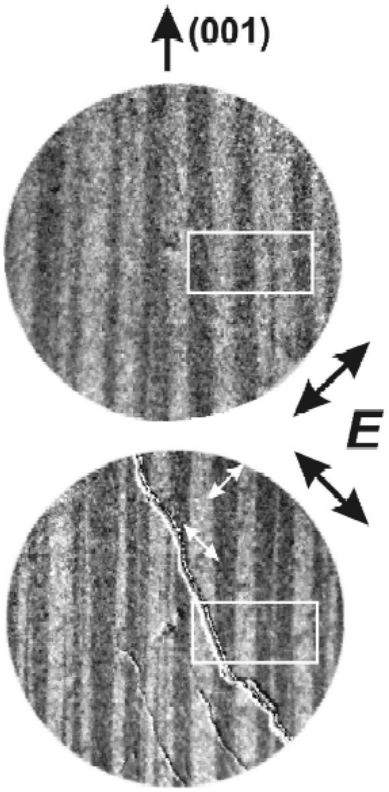

Figure 16 - XMLD image B/A[32]

The strong magnetic contrast in Figure 16 comes from magnetic domains with an in-plane projection of the antiferromagnetic axis either parallel (light) or perpendicular (dark) to the horizontal electric field vector, circled in Figure 15. Domains are not seen when the sample is rotated by forty-five degrees from parallel or perpendicular because the in-plane projection is equal for both orientations. Due to experimental geometry, domains rotated by 180 degrees about the surface normal can not be distinguished from each other. Figure 15 also reveals that the maximum contrast occurs when the electric field of the light is forty-five degrees from the [001] or [010] directions in the crystal

surface. Therefore, the magnetic moment directions shown in Figure 16 are roughly forty-degrees to the strip patterns, which has widths around 10 μm (larger than expected for epitaxial thin films).[35-36] Larger domain sizes will be useful in applications; we will explore one such example shortly.

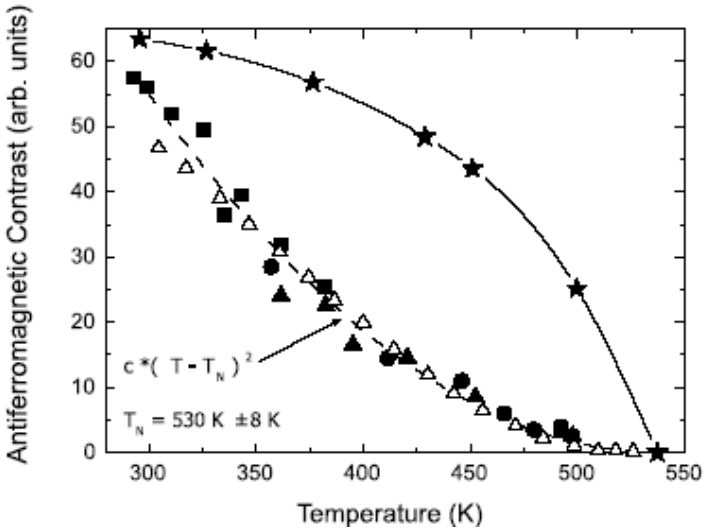

Figure 17 - NiO AFM contrast temperature dependence from Ni L_2-edge fine structure with superimposed theory curves.

Studies of the temperature dependence reveal that the image contrast is reduced at higher temperatures and can be reversed by cooling as seen in Figure 17. In this case, it is customary to assume that no chemical or diffusive processes are affecting the sample's surface magnetic state at these temperatures. Since the domain pattern is not changed, stresses from the bulk domains are the likely cause of the size and topology of the domains. The antiferromagnetic contrast has a parabolic temperature dependence, which disappears above the sample's Neel temperature of 530K. This agrees with low energy electron diffraction measurements of magnetic superstructure reflections, which also show a signal proportional to the square of the antiferromagnetic order parameter. This technique allows simultaneous determination of multiple antiferromagnetic domains as well as investigation into their origin.

2.4.5 Combining XMCD and XMLD

Though these techniques (XMCD and XMLD) are utilized to individually study ferromagnetic and antiferromagnetic domains, they can also be combined to study coupling between different materials. For example, Chapter 6 will discuss our study of the coupling between the electrically controllable antiferromagnetism of BFO and a ferromagnetic layer. There has recently been a great deal of experimental[37] and theoretical[38] interest in using standard antiferromagnetic thin films to pin the magnetization direction of a ferromagnetic layer, due in part to their usefulness in spin valve devices.[39] This effect is known as exchange bias and will be discussed further in Chapter 6. Even after extensive research, little is known about this effect since there are very few techniques that provide information on arrangement of magnetic moments near an interface. PEEM is a unique way to measure this kind of system since it is sensitive to the magnetic vectors in both the ferromagnet and the buried antiferromagnetic layers.[40]

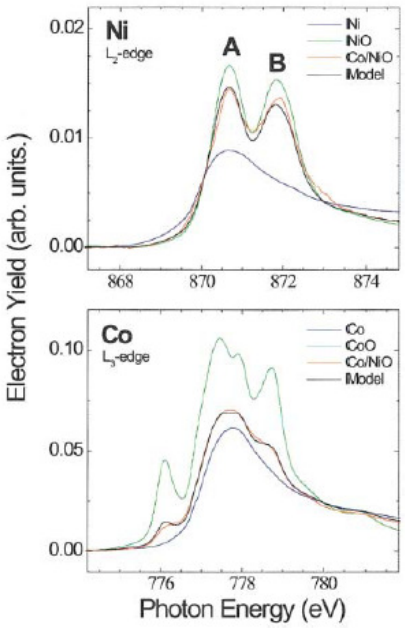

Figure 18 - L edges of Ni and Co for sample and metal and expected oxidation state[41]

Let us consider an example very similar to the previous antiferromagnet example. Ohldag et al. also studied the result of growing ferromagnetic cobalt *in situ* by electron beam evaporation on top of the antiferromagnet NiO.[41] The fine structure in the L-edges of Ni and Co in Figure 18, recorded by tuning to the appropriate energy (870 eV

and 780 eV respectively) allow one to distinguish between the metal and oxidation states. Also included in the graphs for comparison are the structures expected from Ni metal, Co metal, NiO, and CoO. This data shows evidence of interfacial diffusion effects which are likely to change the magnetic structure at the interface. For example, notice that the Ni edge signal looks more like the expected signal for Ni, rather than NiO. It is known that the material below is NiO, meaning the amount of NiO has been reduced at the interface with Co. This is likely due to uncompensated spins from an interface layer that is either ferromagnetic or ferrimagnetic. Linear dichroism was used to study the antiferromagnet NiO by dividing peaks A and B (as before), while circular dichroism was used to study the ferromagnet Co by dividing the images at the L3 and L2 peaks. The limited sampling depth and small thickness of Co combine to allow interface sensitivity. Using the photon energy at peak A emphasizes the Ni-metal component. By using circular polarization and dividing the resulting right and left circularly polarized images as shown in Figure 19, one can hunt for uncompensated spins. The signals in Figure 19 are the XMCD of Co (top), Ni (middle), and the XMLD of NiO (bottom). The ellipses on the left are a key for the domain orientations. It is

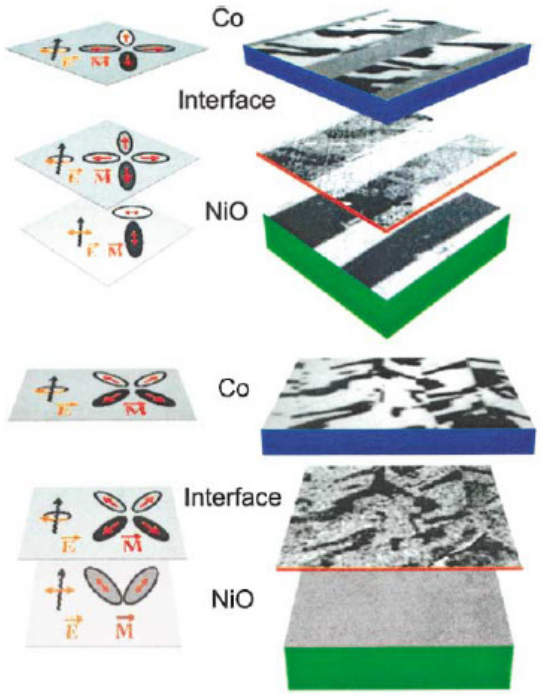

Figure 19 - XMCD of Co (top) and Ni (middle) and XMLD of NiO (bottom) with 45° rotation[41]

important to note that the antiferromagnetic domain walls are parallel to the in-plane [100] directions and the in-plane projection of the incident k vector is parallel to [110]. The two geometries given in Figure 19 are rotated 45 degrees from each other. Otherwise, the signals are from the same sample position. The middle image of the top orientation seems to be a superposition of the XMCD Co and XMLD Ni L edges. As the circular polarization at PEEM2 is not perfectly circularly polarized, there is a small component of linear polarization from the in-plane component of the circularly polarized x-rays. For this reason, we see the antiferromagnet NiO stripes in the XMCD Ni L edge. But if one rotates the sample by 45 degrees, the linear dichroisms goes away and thus so do the stripes. The FM Ni signal (middle) of the rotated sample now shows exactly the same domain patterns as Co does. Before deposition of Co the structure looked different, and therefore it can be surmised that the addition of Co creates and aligns uncompensated spins.

This is further supported by the increasing number of interfacial spins with increasing time in an annealing temperature of 600K, which is higher than the material's Neel temperature.

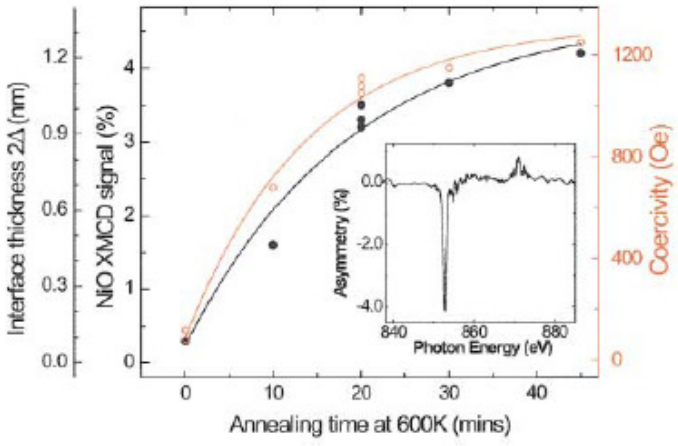

Figure 20 - XMCD, interface thickness, and coercivity

The time dependence of the circular dichroism asymmetry, magnetic interface thickness, and coercivity is shown in Figure 20. According to Ohldag et al.,[42] the asymmetry of the circular dichroism is defined by the L3 peak intensity (see the inset) which is a direct

measure of the Ni spin moment. The interfacial moment and thickness increase with time up to some saturation. This happens because the oxygen concentration at the interface, where this takes place, starts out large but decreases as the oxygen diffuses into the Co. The coercivity, measured by magneto-optical Kerr effect, does not go above 1350 Oe. It also follows the same pattern as the interface thickness, as shown in Figure 20.

Previous studies of exchange bias have considered several possible origins of the uncompensated spins, such as termination of the bulk structure,[43] spin-flop canting of AFM spins,[44] and defect-oriented effects.[45-46] Ohldag et al. instead show that in NiO/Co the existence of an interface layer creates uncompensated spins, which govern the coercivity increases and exchange bias. Annealing time increases the interface thickness and coupling strength. This example is clearly a good demonstration of the power of PEEM and x-ray absorption.

Current PEEM setups have the ability to resolve 20 - 1000 nm antiferromagnetic domains in thin films, which is an important capability for further understanding of the science of surface magnetism. The capability of PEEM to study both XMCD and XMLD makes it ideal for the examination of individual magnetic materials as well as ferromagnetic-antiferromagnetic interfaces to study exchange bias,[40] the interaction between a ferromagnetic and antiferromagnetic layer.[34] There is still much to learn about the surfaces and interfaces of magnetic materials. PEEM is an indispensable tool for this research due to its ability to simultaneously give information regarding magnetic

moments and the Neel temperature along with highly resolved images of magnetic domains.

Chapter 3: Electric Control of Antiferromagnetism

The possibility to electrically control magnetism is extremely interesting from both a physics and application perspective. This chapter discusses the existence of such coupling in BFO thin films. The chapter starts with a theoretical discussion on how such electrical control could occur. The possible ferroelectric switching mechanisms are introduced and illustrated through PFM measurements. PEEM is used as a tool to provide insight on the magnetic properties of BFO. PEEM's sensitivity to ferroelectricity as well as magnetism is introduced and investigated through thorough temperature dependence. Electrical control of magnetism is demonstrated by comparing as-grown and electrically switched PFM and PEEM images of BFO thin films. Finally, this work was confirmed by electrical control of magnetism in BFO crystals by Lebeugle *et. al*.

3.1 Theory of Electric Control of Magnetism in BFO

As discussed in sections 1.2.1-3, BFO is an excellent model system for the study of parameter coupling. Though BFO was known to be the only room temperature magnetic ferroelectric, there was no information on magnetoelectric coupling in these films—whether it was possible to electrically control magnetism or vice versa. Spaldin's LSDA calculations[14] were the first to strongly suggest that such multifunctional control could be possible in BFO films. These calculations found that (a) the energy was minimized when the antiferromagnetic axis lie in the plane perpendicular to the BFO polarization direction and (b) weak ferromagnetism (which has been observed in BFO films) is only allowed by symmetry when the magnetism lies in this perpendicular plane.

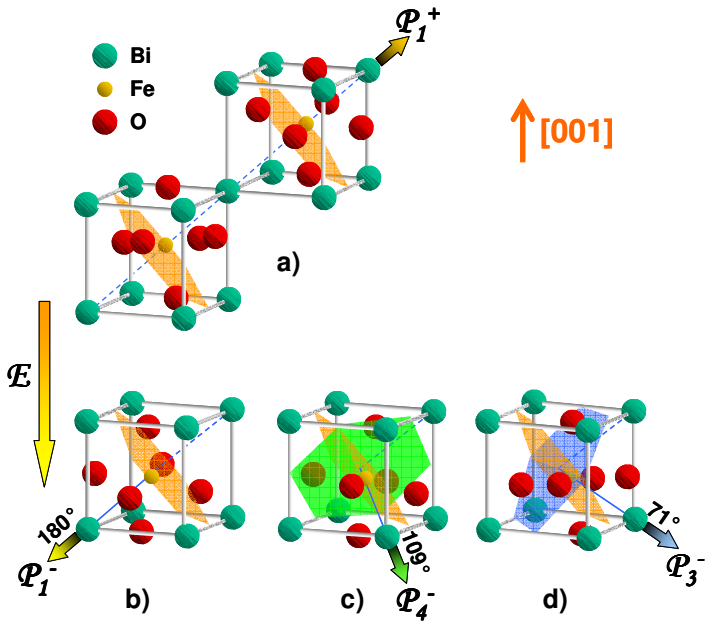

Figure 21 - Schematic diagram of (001)-oriented $BiFeO_3$ crystal structure and the ferroelectric polarization (bold arrows) and antiferromagnetic plane (shaded planes). a) Polarization with an up out-of-plane component before electrical poling. b) 180◦ polarization switching mechanism with the out-of-plane component switched down by an external electrical field. The antiferromagnetic plane does not change with the 180◦ ferroelectric polarization switching. 109◦ (c) and 71◦ (d) polarization switching mechanisms, with the out-of-plane component switched down by an external electrical field. The antiferromagnetic plane changes from the orange plane to the green and blue planes on 109◦ and 71◦ polarization switching respectively.

Perpendicular magnetism could potentially have a very interesting consequence for BFO films. If one can force the polarization direction to change to one of the other 111 body diagonals, the initial perpendicular plane is no long perpendicular and a new perpendicular magnetic plane should form, thereby controlling the magnetism. Control of the ferroelectric domains in BFO films is indeed possible by the application of a ~12 V vertical electric field using PFM. As demonstrated in Figure 21, application of a vertical electric field can result in three types of switching—180°, 109°, and 71°. In the case of 180° switching, the initial and resulting perpendicular magnetic plane are the same, so no change in magnetism is required. However, the 71° and 109° switching should result in a magnetic plane change.

3.2 Ferroelectric Switching of BFO

All three types of switching—180°, 109°, and 71°—are possible using PFM. Figure 22 shows PFM images taken in the same location before (a and b) and after (c and d) electric field poling of a 10 by 10 μm box. As described in Appendix B, the colors in the out-of-plane (a and c) and in-plane (b and d) images are used to determine the ferroelectric direction, the projections of which are shown by the

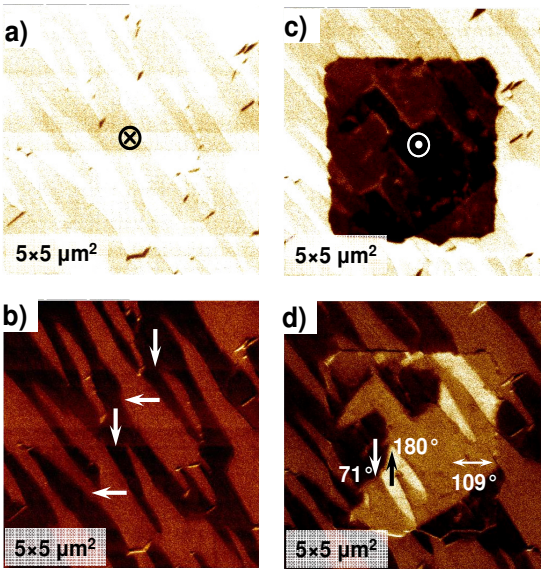

Switching mechanism	PFM with cantilever along ⟨110⟩	
	In-plane	Out-of-plane
71°	Unchanged light* Unchanged dark Unchanged white	White ↔ dark
109°	Light ↔ white Light ↔ dark	White ↔ dark
180°	Unchanged light* White ↔ dark	White ↔ dark

* Indiscernible without sample rotation.

Figure 22 - Out-of-plane (a) and in-plane (b) PFM images of the as-grown BFO film. Out-of-plane (c) and in-plane (d) PFM images taken after applying an electric field perpendicular to the film on the same area as in a and b. Different polarization switching mechanisms are described in the table.

arrows. By comparing the change in these ferroelectric directions due to poling, the switching mechanism can be determined (summarized by the table). All three types of switching are seen simultaneously in this sample.[12]

3.3 Angular Dependence

In order to confirm the electrical control of magnetism in BFO, the ferroelectric domains observed by PFM (Figure 23 a and b) were compared to domains imaged by PEEM (Figure 23 c and d) in the same location on the sample. As it is customary to rotate the sample by ninety degrees to get complete in-plane ferroelectric information (determination of left versus right projections for the brown contrast in Figure 23a), the same rotation is common in PEEM measurements. Since PEEM images (taken at the Fe L3 peaks) give different contrast for domains with magnetic projections horizontal or vertical, a ninety degree rotation should result in a reversal of contrast within the domains. This is the method that many researchers use to distinguish magnetic contrast from surface chemistry or roughness. This reversal is observed between Figures 23c and d. Comparison between the PFM and PEEM images of as-grown BFO also show a match between the domain structures.[47]

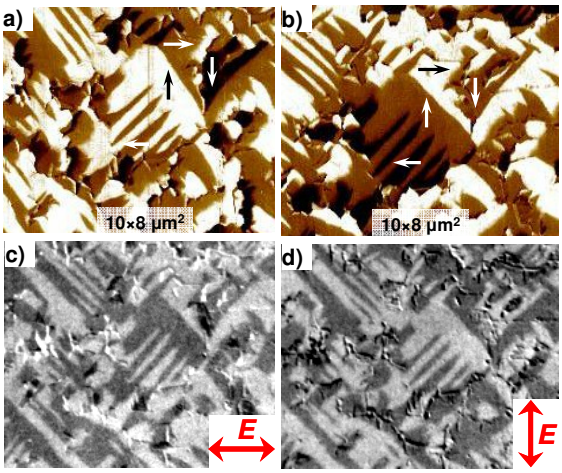

Figure 23 - In-plane PFM images before (a) and after (c) 90◦ in-plane rotation. The arrows show the direction of the in-plane component of ferroelectric polarization. PEEM images before (c) and after (d) 90◦ in-plane rotation between the two images. The arrows show the direction of x-ray polarization relative to the domain structure.

3.4 Ferroelectric Contrast in PEEM

Examining the data presented to this point, it is tempting to conclude that the magnetic domains match with the ferroelectric domains. This has not yet been proven, however; unfortunately, it was found that a dichroic contrast can also be observed due to ferroelectricity. In order to study the dichroic nature of ferroelectricity, consider a pure ferroelectric material periodically poled lithium niobate (PPNL).

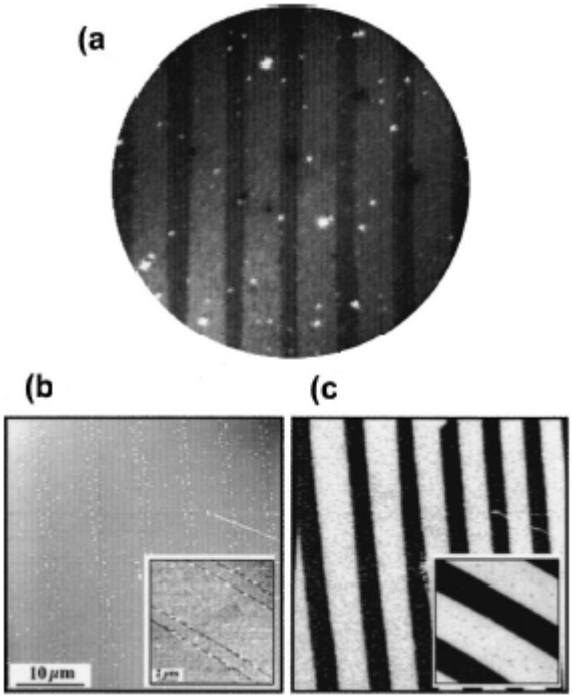

Figure 24 - (a) PEEM, (b) AFM and (c) PFM images of PPLN. The fields of view are 40 μm. Insets in (b) and (c) are 10x10 mm^2 and obtained from the same surface. In (b), the double lines remained at the negative domain boundary regions after the lithography process. In (c), the PFM image obtained from the same region of the AFM image shows that the marked regions are negative domains which are brighter and wider than the positive domains.[48]

As seen in Figure 24, a very similar approach to that employed for BFO was used to study the ferroelectric contribution to dichroism in PPNL single crystals. A PEEM image (a) is compared to the AFM (b) and PFM (c) images in PPNL with a periodicity of patterned domains ~6.8 μm. The bright spots in the image may be dust particles or other foreign materials.[48] The bright regions in the PEEM image are negative domains (domains with negative surface polarization charges), while the darker regions are positive domains.[48] Though the PEEM resolution is not quite as detailed, it is clear

that the PEEM image mimics the ferroelectric nature of PPNL observed by PFM. This result calls into question the previous findings; given the PPNL experimental results, the match between the BFO PFM and PEEM images could result from PEEM probing mainly the ferroelectric nature of the material. Eliminating this possibility requires the examination of the temperature dependence of the linear dichroism of BFO.[48]

3.5 Temperature Dependence

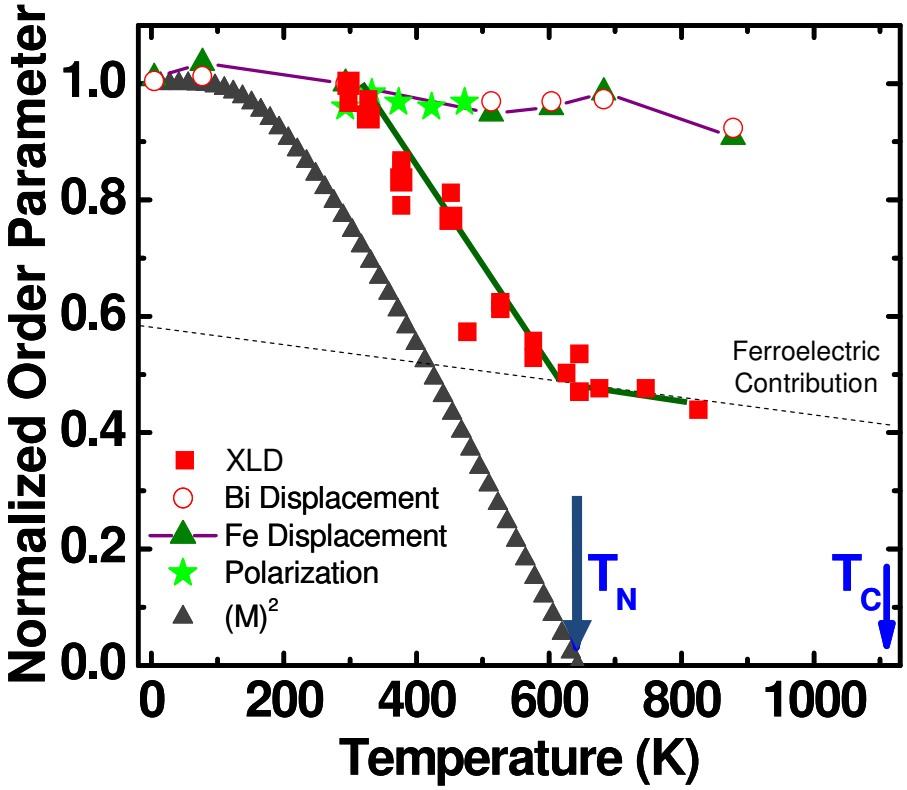

Figure 25 - Temperature dependence of normalized order parameters of $BiFeO_3$. The linear dichroism, out-of-plane lattice parameter and ferroelectric polarization are normalized to the values at room temperature; the Bi and Fe atom displacements and $\langle M^2 \rangle$ are normalized to the values at 0 K.

In order to understand the dichroic temperature dependence of a multiferroic, it is useful to discuss the temperature dependence of its two order parameters. The temperature

dependence of dichroism due to magnetism has been widely studied for antiferromagnets.[34] As seen by the black triangles in Figure 25, the dichroic contrast for a pure antiferromagnet goes as $<M^2>_T$, where M is the magnetic moment at a temperature T. Thus, there should be no magnetic contribution to dichroism above an antiferromagnet's Néel temperature (~640 K for BFO). On the other hand, the polarization contribution remains robust up until its critical temperature of 1100 K. It is known in bulk BFO that the order parameter for ferroelectricity does not change much below its Curie temperature, which is illustrated by the plots of Fe and Bi ionic displacements in Figure 25. To investigate the ferroelectric order parameter in the 600nm BFO film, also plotted is the temperature-dependent out-of-plane lattice parameter obtained from X-ray diffraction, and the ferroelectric polarization obtained using high-frequency ferroelectric pulse measurements. Similar to bulk BFO, the 600nm BFO film shows very little change in the ferroelectric order parameter from room temperature to 800 K and the order parameter change correlates with the high temperature XLD signal. A PFM measurement also confirms the existence of stable ferroelectricity in the BFO film up to 800 K (data not shown here). The bulk-like behavior of the order parameter is consistent with earlier first-principles computations[14,49] and with the fact that minimal lattice strain is expected in the 600 nm film.[50] Thus, a ferroelectric temperature dependence that stays approximately the same over the entire temperature range studied is expected, while the temperature dependence from magnetism should be strong but disappear above the Néel temperature.

We see elements of both order parameters in the dichroic temperature dependence of BFO. Figure 25 shows the measured results on five samples during both heating and cooling. In all cases the PEEM images were captured from the same area of the $BiFeO_3$ film after waiting thirty minutes at each temperature to allow thermal equilibration. The data on one of the samples were recorded on an electrically switched area (see later discussion) while the others were recorded on un-switched areas. We see that in all cases the linear dichroism signal drops rapidly on heating above room temperature, with only ~50% of the room-temperature XLD value remaining at the Néel temperature; this reduction is recovered on cooling. We therefore conclude that the high temperature XLD signal results from the ferroelectric ordering, and the signal below T_N from the sum of the antiferromagnetic and ferroelectric contributions. At room temperature, the magnetic and ferroelectric components are of roughly equal strength. The dichroism images from section 3.2 are not dominated by only ferroelectricity, but instead a roughly equivalent combination of ferroelectricity and magnetism, which can be separated through this angle and temperature dependent approach.

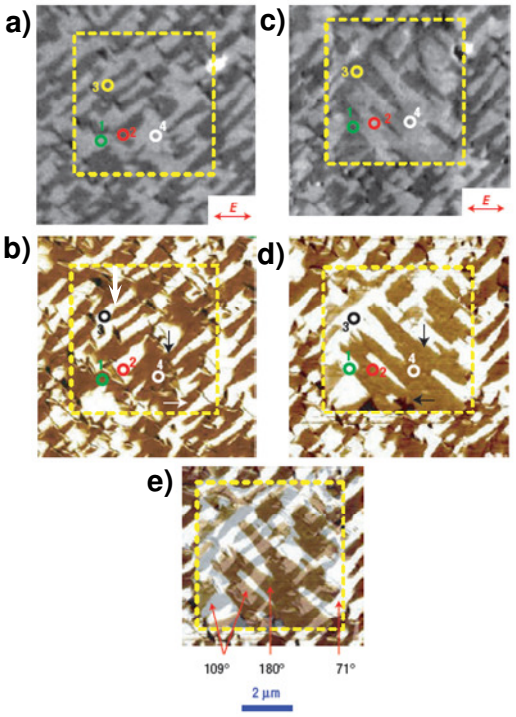

Figure 26 - PEEM images before (a) and after (b) poling. The arrows show the x-ray polarization direction. In-plane PFM images before (c) and after (d) poling. The arrows show the direction of the in-plane component of ferroelectric polarization. Regions 1 and 2 correspond to 109◦ ferroelectric switching, whereas 3 and 4 correspond to 71◦ and 180◦ switching, respectively. (e) A superposition of in-plane PFM scans shown in c and d used to identify the different switching.

3.6 Magnetoelectric Coupling

Having conclusively shown that the PEEM images contain contributions from both order parameters, we now return to the question of electric control of magnetism in BFO by comparing PFM and PEEM images of an area that has been poled. Figures 26a-b show our PEEM results for the BiFeO3 film before and after electrical poling, with the corresponding in-plane PFM results shown in Figure 26c-d. The poled area is outlined by dotted boxes in each figure. We know from the out-of-plane PFM images (not shown) that ferroelectric polarization switches under the applied bias of −12 V. As discussed before, to unambiguously identify the polarization direction in each domain, in-plane PFM scans have been taken along two orthogonal [110] directions (only one shown here). The different switching mechanisms are easily distinguished by superimposing the in-plane PFM images taken before (the grayscale image) and after (the colored image) electrical poling along the same direction, as shown in Figure 26e. The three possible switching mechanisms appear with different colors as marked in Figure 26e. This image serves as a guide to identifying regions that exhibit different switching mechanisms in Figure 26a–d. For example, regions 1 and 2 correspond to 109◦ switching, region 3 to 71◦ switching, and region 4 to 180◦ switching. Both 71◦ and 180◦ ferroelectric switching do not change the in-plane projection of the ferroelectric and antiferromagnetic order parameters (Figures 21b and 21d), and thus cannot be detected by a PEEM setup with a fixed x-ray polarization direction parallel to the sample surface. As a result, there is no observable contrast change in regions 3 and 4, although switching may have occurred. (Note that later discussion will show that the ferroelectric and antiferromagnetic coupling

in the 71◦ ferroelectric switching region can possibly exhibit a complicated behavior. The PEEM results at least confirm that the in-plane projection of the antiferromagnetic axis is not changed by the 71◦ ferroelectric switching.) The following discussion will focus on the regions with 109◦ ferroelectric switching. As can be seen in Fig. 5, the PEEM images from the same area track the changes in the PFM images in the region with 109◦ ferroelectric switching: the PEEM contrast reverses, either from bright to dark (region 1) or vice versa (region 2), on ferroelectric switching. Finally, note that the dichroism value (the difference in intensity between the dark and bright domains) and temperature dependence are unchanged by the electrical switching, confirming that the antiferromagnetic domains are switching with the ferroelectric domains; if the ferroelectric polarization switched without reorienting the antiferromagnetic axis, then the ferroelectric component of the XLD would change sign, whereas the antiferromagnetic component would not. As a result, the dichroism value in the switched area would have a smaller value and a different temperature dependence.

Pioneered by Ascher and co-workers on Boracite7 in 1960s, electric control of a magnetic domain has been reported on several materials, such as $YMnO_3$.[51] The research presented here, however, goes further than the earlier work in that it is (1) at room temperature; (2) on thin films, a more favorable system for applications; and (3) performed with an active control, unlike in the $YMnO_3$ case.[51] This is the first observation of ferroelectrically-induced antiferromagnetic switching at room temperature. Very recently, an exchange bias coupling between an antiferromagnetic $BiFeO_3$ layer and an adjacent ferromagnetic layer has been reported.[52] By combining the ability to

ferroelectrically control antiferromagnetism (as revealed in this work) and the capabilities of antiferromagnetic modulation of ferromagnetism,[52] an ultimate electric control of ferromagnetism can be achieved, as will be the topic of Chapter 6.

Recall that the first-principles calculation of the magnetocrystalline anisotropy in bulk $BiFeO_3$ predicted a six-fold degeneracy of the orientation of the antiferromagnetic sublattice magnetization within the [111] plane.[14] In such a case we would, in principle, expect to see many different antiferromagnetic domains within each ferroelectric domain with different projections of the antiferromagnetic order parameter on the polarization direction of the x-ray beam. However, in the PEEM measurements it seems that every ferroelectric domain coincides with only one antiferromagnetic domain. This could either mean that the six-fold degeneracy is broken in the films so that only one possible orientation of the antiferromagnetic axis with respect to the ferroelectric polarization occurs, or that we see only an effective projection of the antiferromagnetic axis, averaged over all six possible orientations because of the resolution limits of the PEEM. The six-fold degeneracy could be lifted, for example, by a small monoclinic strain, which could indeed occur in a BiFeO3 film grown on a (001) substrate; although the homogeneous strain in the 600-nm-thick films used in our experiments seems to be fully relaxed, a small inhomogeneous strain component could still persist. Furthermore, the degeneracy of the magnetization direction could also be lifted by other effects related to the presence of the surface and the substrate. The effect of strain and thickness and how they can be utilized to control magnetism will be the focus of Chapter 5.

3.7 Confirmation

Bragg peak	$\vec{P}, \vec{k}_1$	$\vec{P}, \vec{k}_2$	$\vec{P}, \vec{k}_3$	I_{obs}
$(\frac{1}{2}, \frac{-1}{2}, \frac{1}{2})$	**189**	122	122	**198(8)**
$(\frac{1}{2}, \frac{1}{2}, \frac{1}{2})$	**100**	100	100	**99(6)**
$(\frac{-1}{2}, \frac{1}{2}, \frac{1}{2})$	**122**	122	189	**116(6)**
$(\frac{1}{2}, \frac{1}{2}, \frac{-1}{2})$	**122**	189	122	**114(6)**
$(\frac{1}{2}, \frac{-3}{2}, \frac{1}{2})$	**113**	71	71	**111(11)**
$(\frac{3}{2}, \frac{-1}{2}, \frac{-1}{2})$	**71**	71	113	**83(8)**
$(\frac{-1}{2}, \frac{-1}{2}, \frac{3}{2})$	**71**	113	71	**83(8)**
$(\frac{-1}{2}, \frac{-3}{2}, \frac{-1}{2})$	**71**	61	61	**78(9)**
$(\frac{3}{2}, \frac{1}{2}, \frac{1}{2})$	**61**	61	71	**52(6)**
$(\frac{1}{2}, \frac{1}{2}, \frac{1}{2})$	**61**	71	61	**56(7)**

Bragg peak	$\vec{P}_0, \vec{k}_1$	$\vec{P}_{71}, \vec{k}'_1$	$\vec{P}_{71}, \vec{k}'_2$	$\vec{P}_{71}, \vec{k}'_3$	I_{obs}	I_{calc}
$(\frac{1}{2}, \frac{-1}{2}, \frac{1}{2})$	**189**	**100**	100	100	**158(7)**	**150**
$(\frac{1}{2}, \frac{1}{2}, \frac{1}{2})$	**100**	**189**	122	122	**145(6)**	**139**
$(\frac{-1}{2}, \frac{1}{2}, \frac{1}{2})$	**122**	**122**	122	189	**120(8)**	**122**
$(\frac{1}{2}, \frac{1}{2}, \frac{-1}{2})$	**122**	**122**	189	122	**112(9)**	**122**

Figure 27 - Table of Bragg intensities for BFO crystal before (top) and after (bottom) electric field poling[53]

In the year following the publication of the results presented in this chapter, the coupling between ferroelectricity and antiferromagnetism was confirmed for single crystals of BFO using neutron scattering measurements.[53] The single crystals grown by this group have only one as-grown ferroelectric direction, as opposed to the thin films discussed before. Due to the rhombohedral symmetry of the crystals, there are three equivalent propagation vectors for the magnetism: $k_1 = [\delta\ 0\ -\delta]$, $k_2 = [0\ \delta\ -\delta]$ and $k_3 = [-\delta\ \delta\ 0]$ where $\delta = 0.0045$. The same experiment completed for powder neutron diffraction would result in three different equally populated k domains, leading to a splitting of magnetic peaks along the three directions. Lebeugle *et. al*. measured the intensity distribution of the as-grown crystals around the four antiferromagnetic Bragg reflections of the (½, ½, ½) type. The top table in Figure 27 illustrates that prior to electric field poling all of the magnetic information lie along one direction (in bold), namely **k** = [1 0 -1]. However, after electric field poling when roughly half of the domains rotate by 71 degrees, the Bragg intensity becomes an average of the equivalent k_1 for the new polarization direction and the original k_1. No other k value is selected (k_2 or k_3), demonstrating that the magnetic order is coupled to the ferroelectric order in BFO crystals.

In this chapter, the existence of magnetoelectric coupling in BFO thin films was explored. We learned that electric control can be achieved theoretically by manipulating the magnetic plane perpendicular to the ferroelectric direction. By comparing PFM and PEEM images at the same locations, this control was confirmed experimentally in BFO thin films. Additionally, PEEM's sensitivity to ferroelectricity as well as magnetism was introduced and investigated through thorough temperature dependence. This electrical control of magnetism in BFO crystals was confirmed by Lebeugle *et. al*. This study is an excellent step in being able to manipulate magnetoelectric coupling; however, in order to fully benefit from this cross-parameter control, a detailed understanding of the individual order parameters and how they can be influenced is necessary. The ferroelectric properties of BFO are already well studied.[12] The full magnetic behavior as it varies with thickness will be the topic of the next chapter.

Chapter 4: Thickness Dependence of Magnetism in BFO

This chapter starts with a continuation of the discussion of BFO crystals, focusing on the details of the magnetic order. Significant differences in the polarization of thin films were discovered, prompting the investigation of the effect of thickness on ferroelectric and magnetic properties in BFO films. Angle- and temperature-dependent PEEM measurements in addition to dichroism modeling were utilized to discover a preferred magnetic [112]-type axis in thin films, as opposed to the easy magnetic plane observed in bulk. Finally, the reduction of ferroelectric polarization and magnetic is addressed for ultrathin BFO films.

4.1 Bulk BFO

Until recently, the only BFO measurements available were on bulk samples. The fact that bulk BFO exhibits ferroelectricity below 1100K and G-type antiferromagnetism below 643K has been known for several decades.[54-55] Though the understanding of details in ferroelectric order has progressed considerably in that time, research into the specifics of magnetic order has not been as successful, largely due to the scarcity of techniques available to study antiferromagnetism. Neutron measurements[53,56-57] revealed that the antiferromagnetic sublattices spiral with a period of ~62 nm as observed in Figure 28. Therefore, even the net magnetic moment resulting from canting will cancel in the bulk. The two diffraction satellites in Figure 28b indicate that the cycloid is along the [10-1] direction.

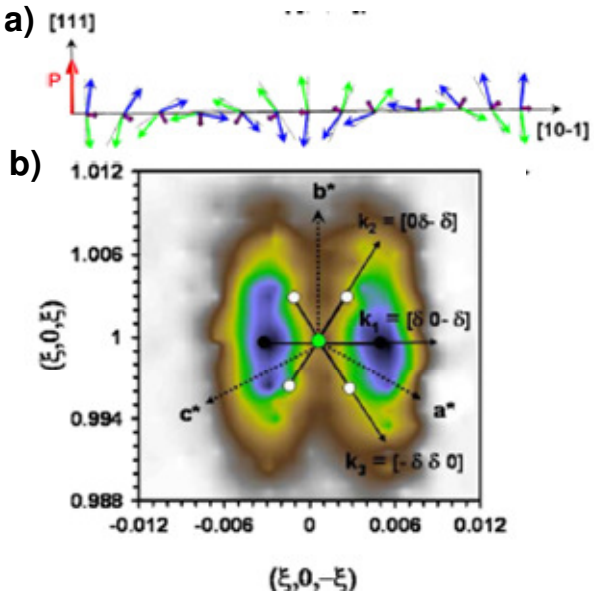

Figure 28 – (a) Schematic of spiraling of the antiferromagnetic order in BFO. (b) Neutron intensity around the (½, -½, ½) Bragg reflection.[53]

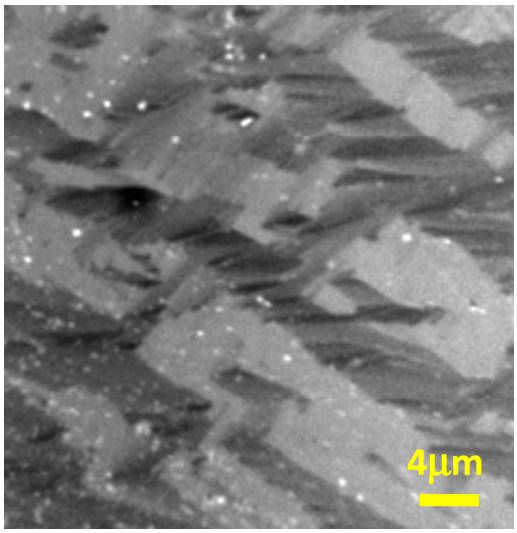

Figure 29 – PEEM image of BFO crystal reveals large FE stripes with magnetic variation

This spiraling magnetic order can also be observed by PEEM measurements. Figure 29 shows a PEEM image of a BFO crystal taken at the ALS PEEM2 microscope. Although most of the crystal appears to

have only one ferroelectric domain, there are regions where two ferroelectric variants with domain widths of several microns are observed. Within the stripe-like ferroelectric domains, there is variation of contrast which is believed to be the spiraling of the magnetic order. To verify this, the contrasts in the three boxes (B, C, and D) in Figure 30a were measured with the light polarization of the incident x-rays rotated from vertical (*s*-polarized) to horizontal (*p*-polarized). The detail behind these changes in contrast will be discussed in more detail for thin films later in this chapter, but some trends are already evident. Even within the same ferroelectric domain (boxes B and D), there are different angular dependencies (Figure 30b). Between ferroelectric domains, the difference is even greater, which is expected since the magnetism lies on difference planes, perpendicular to the two ferroelectric directions.

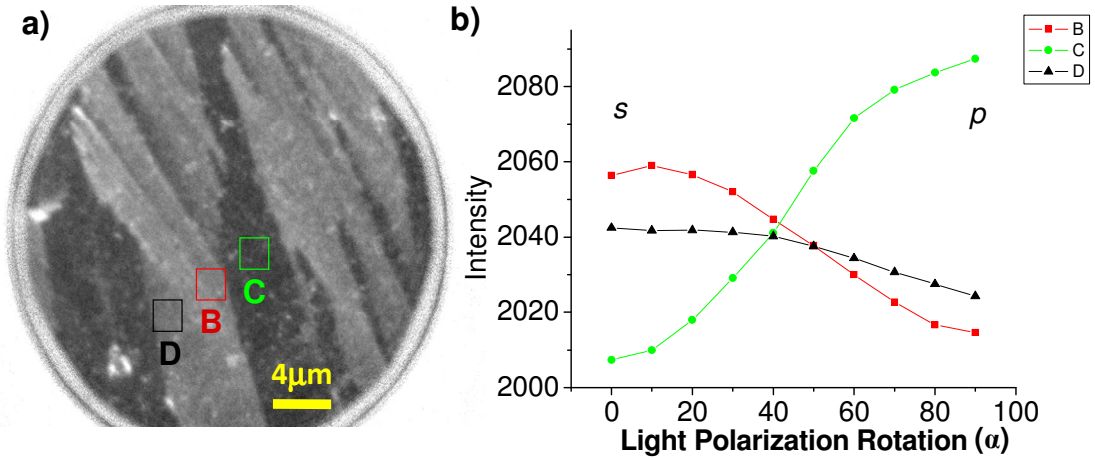

Figure 30 – (a) PEEM image showing the location of three areas for x-ray light polarized at α= 0°. (b) The angular contrast of these areas are shown through the light polarization rotation.

Spiraling magnetic order has an interesting consequence beyond the lack of net magnetic moment. The linear magnetoelectric effect is averaged to zero in bulk BFO due to the fact that the average value of the projection of the antiferromagnetic vector in the cycloidal

structure is zero.[58] Many believe that the linear magnetoelectric term—being the first order term—must be present in order to have strong coupling. The cycloidal structure does not prevent manifestation of the quadratic magnetoelectric effect.[59] There is at least one way to allow a linear effect: the spin cycloidal structure that prevents the linear magnetoelectric effect from being observed can be destroyed by high magnetic field.[60] Application of high magnetic field (~20 Tesla) can induce a phase transition from a spatially-modulated spin structure to one with a homogeneous spin order.[58] However, it seems unlikely that such a high field would be useful for energy saving applications of magnetoelectrics.

4.2 BFO Thin Films

4.2.1 Discovering Differences Between Thin and Thick Films

The lack of a linear magnetoelectric effect in bulk BFO led many to believe that strong magnetoelectric coupling would not be possible for this material. Some researchers decided to search for new materials despite the fact that no other room temperature magnetic ferroelectric was known. Others looked for more exotic approaches, such as interface magnetoelectricity by combining two or more materials, but they have met with limited success so far. Most recently, new research on BFO has shown that it may still be a viable candidate material for magnetoelectric coupling.

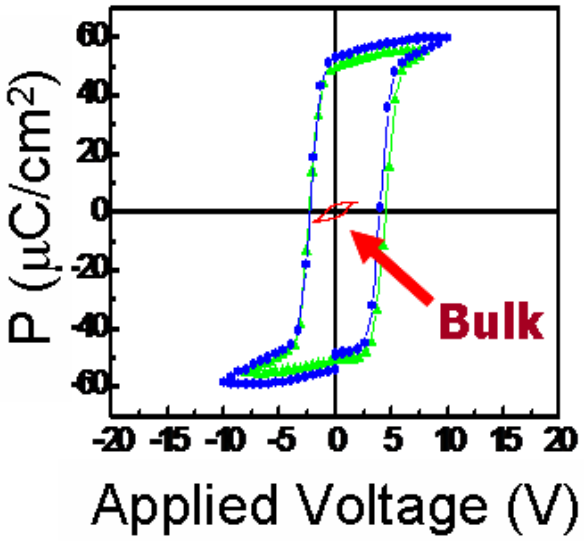

Figure 31 – Recent understanding of ferroelectric hysteresis curves for 200 nm thick BFO films and crystals.

The Ramesh group discovered that BFO thin films, though still ferroelectric and antiferromagnetic, possess important differences from their sister crystals shown in Figure 31. It was recently believed that the bulk BFO spontaneous polarization P_s was only 3.5 microcoulombs per square centimeter ($\mu C/cm^2$) along the (001) direction, whereas BFO thin films have a P_s of approximately 55 $\mu C/cm^2$.[61] Today, it is known that *high-quality* crystals and films have the same large P_s, illustrating the importance of first-rate growth and characterization to certify material excellence. This actual value is big enough to rival some of the best known ferroelectrics such as PZT, making BFO an attractive alternative for existing ferroelectric applications and allowing for new possible functions involving both ferroelectricity and magnetism. Additionally, though no net magnetic moment had been observed for BFO crystals, moments as large as 200 emu/cc have been measured in films. Large angle x-ray scans of these thin films showed diffraction peaks from only the substrate and the (001) pseudocubic reflections. No reflections indicated secondary phases. Throughout this chapter three classes of films will be addressed: ultra-thin films with thickness (t) < 20 nm, thin films that have 20 nm < t < 200 nm, and thick films that have t ~1 μm.

4.2.2 Exploring Reasons for Differences

Why should the properties of thin film BFO be significantly different from BFO crystals? Jiang and Qui used the Landau free energy function—commonly used for ferroelectrics—to investigate the ferroelectric and magnetic properties of epitaxial BFO thin films.[62] They found that the lattice parameter, polarization and magnetization of BFO are theoretically a function of strain as plotted in Figure 32. In very thin films, the lattice parameters of BFO attempt to match those of the substrate as long as the mismatch is not too large (Figure 32a). However, as films grow in thickness, this matching relaxes and eventually reaches bulk lattice parameters. Limited data fit relatively well to the theory, though no ultrathin films (thickness < 25 nm) were compared in this study. Theory suggests a large increase in the polarization and magnetization for small thicknesses. This theory fits well with past observations on pure ferroelectrics which found that although bulk ferroelectric oxides normally break long before they are strained to percent levels, such strains are readily applied to ferroelectric thin films through the use of epitaxy on appropriate substrates.[63] These strains can have a tremendous effect on the properties of ferroelectric thin films and superlattices. They can make materials that are not ferroelectric at any temperature ferroelectric and also change the ordering temperature by hundreds of degrees while simultaneously enhancing the remnant polarization.

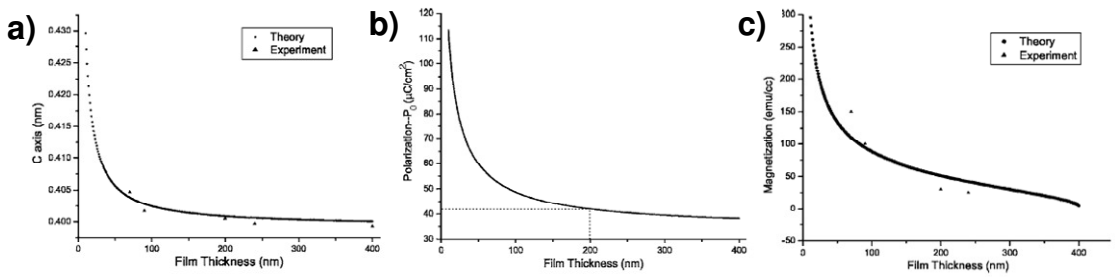

Figure 32 - Film thickness dependence of (a) *c*-axis lattice parameter, (b) spontaneous polarization P_0, and (c) saturation magnetization M_{sat} with the saturated magnetic field of 6000 Oe.

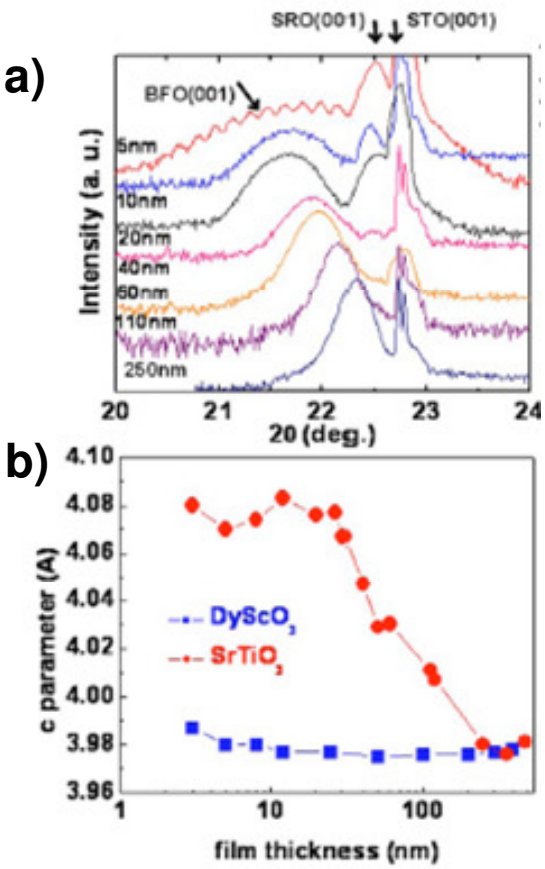

Figure 33 – (a) XRD *θ-2θ* scans for the BFO films of varying thickness on STO substrates and (b) out-of-plane lattice parameter as a function of thickness on STO and DSO substrates.[64]

These theoretical results were shortly confirmed for the lattice parameter and polarization of BFO by Chu *et. al*.[64] For film thicknesses greater than ~ 25 nm, a strong thicknesses dependence is observed through the XRD *θ-2θ* scans presented in Figure 33a. Figure 33b shows two distinct curves, one that changes dramatically and another that does not. Lattice mismatch between BFO (a_{BFO}=0.396 nm) and STO (a_{STO}=0.390 nm) results in an in-plane isotropic compressive strain that causes an elongation in the out-of-plane direction which gradually decreases with increasing film thickness. On the other hand, due to the small lattice mismatch between BFO and DSO (a_{DSO}=0.396 nm), BFO experiences less strain, and thus,the out-of-plane lattice parameter remains closer to the bulk value over the range of thickness. As expected, a large change in the polarization is seen for BFO on STO and the change is not as dramatic for films on DSO.

We saw a similar trend for magnetization,[61] but the source of this change was unclear. Recent work suggests that the magnetic spiral structure is suppressed in thin films,[65] but how does this effect the magnetic state? Recall that recent density functional theory

calculations for bulk BFO predict that the individual moments for each Fe-ion should lie along any one of six possible energetically-degenerate magnetic axes of the <1-10>- or <112>-type in an easy 111-type plane, which are perpendicular to the <111> polarization direction,[14] shown as the transparent red plane in Figure 34. This degeneracy of the magnetic axes is lifted if BFO becomes monoclinic, as would occur due to strains caused by growing on a substrate. The strain squeezes the 111 plane horizontally and allows it to stretch vertically.

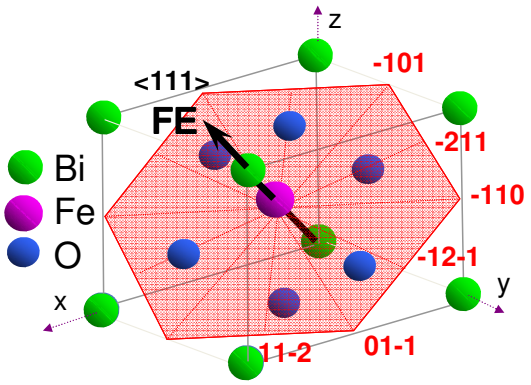

Figure 34 – Schematic showing six energetically preferred axes for BFO with ferroelectric polarization pointing along [111].

Why should this stretching and squeezing affect the magnetic behavior of BFO? Antiferromagnetism in BFO comes from superexchange mediated through the Fe-O-Fe bonds. The exchange constant is thought to depend strongly on distance, and therefore these small changes might have a drastic effect.[66] This choice of a preferred axis is not unheard of in other materials; strain-driven changes in magnetic structure have been observed previously in other magnetic oxide systems which exhibit a strong coupling among spin, charge, orbital and lattice degrees of freedom (for example, refs. 41 and 66). In these materials, strain-induced changes have been interpreted by considering the variation of the electronic hopping amplitude due to the change of bond lengths and bond angles.[66] Strain has been shown to affect the nature of antiferromagnetism in oxides such as NiO. It has been suggested that an orthorhombic contraction (i.e., that which would

result from an in-plane compressive strain) along [100] favors a <110> easy axis, whereas a monoclinic expansion (i.e., that which would result from an in-plane tensile strain) along [110] favors a <112> easy axis.[67]

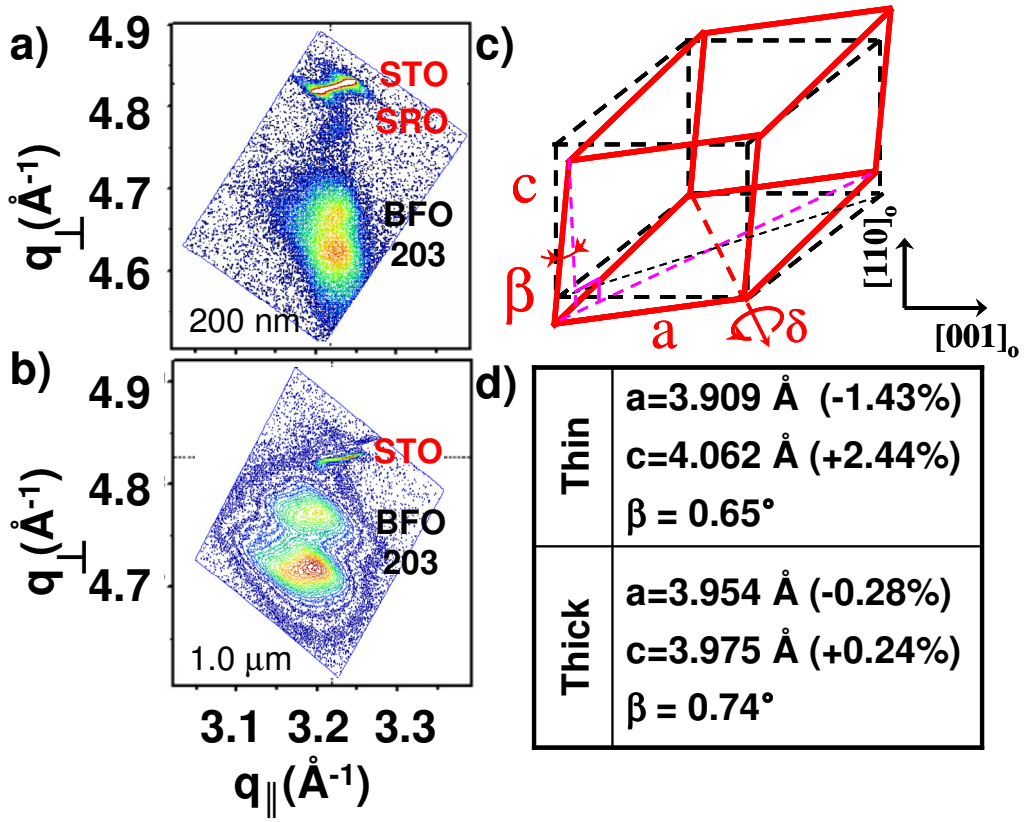

Figure 35 - The crystal structure of thin and thick BFO films grown on SRO/STO(001). RSMs for thin (a) and thick (b) BFO grown on SRO/STO(001). (c) Schematic illustrating the nature of the crystal structure of the BFO film, where *a* is the in-plane lattice parameter, *c* is the out-of-plane lattice parameter, and β is the monoclinic distortion angle. (d) Unit cell parameters, as determined by RSM, for both strained (thin) and relaxed (thick) films.

Recall that the lattice mismatch between BFO and STO (1.54%) imparts a compressive in-plane strain to the BFO film that is progressively relaxed as the film thickness is increased.[64] Using x-ray reciprocal space mapping (RSM) of the 203 BFO diffraction peak as shown in Figure 35a-b we have studied the strain state in such films as a function of film thickness. The in-plane (*a*) and out-of-plane (*c*) lattice parameters, as well as the monoclinic tilt angle (β), are shown in the table, along with a schematic describing the

nature of the structural distortions (Figures 35c and 35d). In the case of a 200 nm thick BFO/SRO/STO (001) film, the in-plane lattice parameters are matched with those of the substrate and the unit cell is under compressive strain (c/a-1 ~ +3.9%) [Figure 35a]. As the film thickness is increased to 1 μm, the lattice parameters gradually approach the bulk BFO value and the pseudo-tetragonality (c/a-1) becomes smaller (+0.53%) as measured from RSM (Figure 35b). β is derived from the peak splitting of the 203-peak and is calculated to be ~0.74°, close to the value measured in bulk BFO. The in-plane compressive strain lifts the degeneracy of magnetization in the 111-plane, as is also observed in the case of NiO thin films.[41] A preferred axis can also be understood in terms of the magnetostriction in BFO. The magnetostriction constant of BFO is positive,[68] meaning that the lattice constants expand along an applied magnetic field. Substrate-induced compressive strain is effectively the opposite of this effect and thus results in a preference of a magnetization direction that has the largest out-of-plane component while remaining in the (11-1), i.e, the <112>. However, another argument claimed that the 110 axis, which is in-plane, would be preferred because it can be shared by four different polarization directions and that would be efficient energetically.[47] To determine between these axes and other possible magnetic behaviors, we used angle-resolved, temperature-dependent PEEM measurements compared with ferroelectric PFM measurements.[69]

4.2.3 Angle-Dependent Measurements of BFO Thin Films

Single phase, epitaxial thin films of BFO were grown on a 50 nm thick conductive bottom electrode of $SrRuO_3$ (SRO) on $SrTiO_3$ (STO) (001) single crystal substrate via laser-molecular beam epitaxy and metalorganic chemical vapor deposition. Detailed x-ray diffraction studies coupled with transmission electron microscopy were used to establish the crystalline quality of the heterostructures; these films were found to be single phase and fully epitaxial.

As measured by PFM discussed previously, the in-plane ferroelectric domain structure of one BFO thin film is shown in Figure 36. The long axis of the ferroelectric domains (or direction of the domain walls) lies along the <100> of the underlying $SrTiO_3$ (001) substrate or the pseudocubic-<100> of BFO. The polarization direction of the various stripe-like domains lies along the <111> and the in-plane projection of those polarization directions lies along the <110>. The arrows in Figure 36 refer to the in-plane projection of the ferroelectric polarization directions (four variants) present in this model system. Such a model ferroelectric domain structure forms the reference frame for our photoemission measurements.

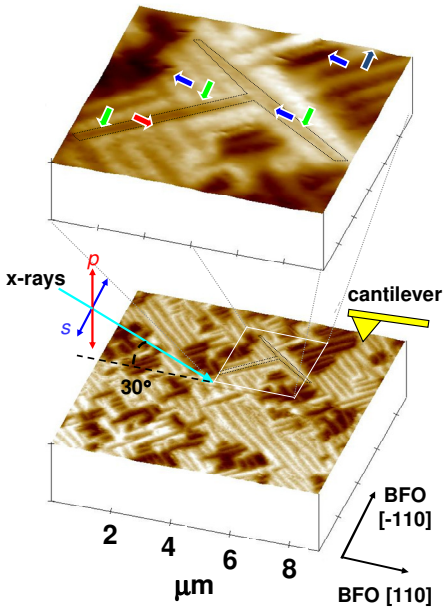

Figure 36 - PFM image of in-plane polarization projections with PFM and PEEM geometries (taken separately), showing incident x-rays 30 degrees from sample surface.

Once the ferroelectric domains are well characterized, the magnetic behavior can be studied. *L*-edge spectra depend on anisotropies in the charge or the spin in the material, and thus are sensitive to the relative orientation of the x-ray polarization and AFM axes which are then imaged by PEEM. Recognizing that x-ray linear dichroism can arise from any anisotropic distribution of charge in a material, (as discussed in sections 3.4 and 3.5 for the case of both ferroelectric and antiferromagnetic order), we have decoupled the contributions from these sources unambiguously through temperature- and angle-dependent measurements.

Figure 37a illustrates the x-ray polarization geometry in which the XLD-PEEM images in Figures 37b-e were taken. The images in Figures 37b-e are from the corresponding area shown in Fig.36 (the "T" shape in Figures 36 and 37b are outlined as an aid to the reader). Images result from dividing intensity maps taken at the Fe-L_3 absorption edge using linearly polarized light as the angle of the plane of linear incident polarization (α) varies from 0° (p polarization) to 90° (s polarization). The outlined arrows in Figure 37 show the in-plane projection of the four

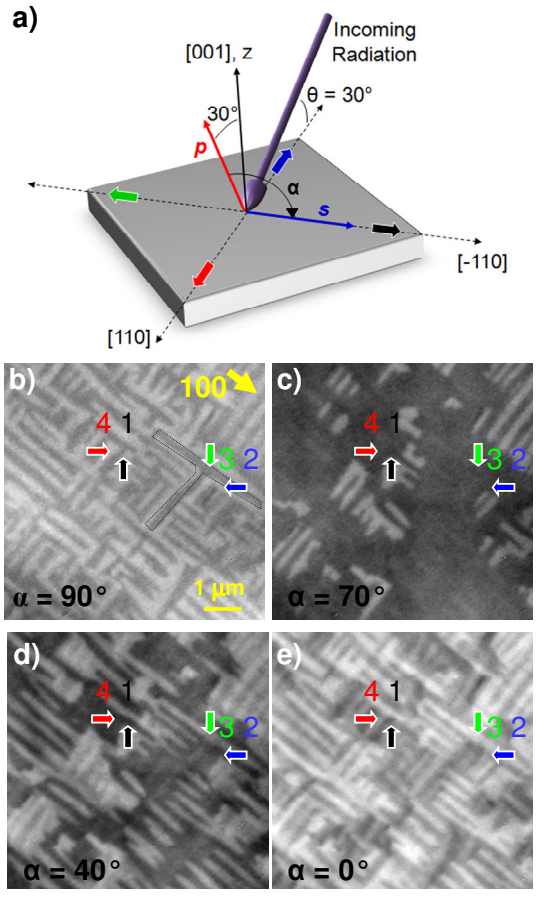

Figure 37 - PEEM images of BFO at several angles of the electric vector of incident linear polarization α. (a) Schematic illustrating the experimental geometries used to probe the angle dependent linear dichroism in BFO. The outlined arrows show the in-plane projection of the four ferroelectric directions. Images of domain structures taken at (b) α=90°, (c) α=70°, (d) α=40°, and (e) α=0°.

ferroelectric directions. When the x-rays are s-polarized (α = 90°), only two contrast scales [labeled as light (1 and 3) and dark (2 and 4) in Figure 37b] are observed. We have chosen a geometry such that the x-ray polarization vector for an s-polarized incident beam is along [-110], which maximizes the difference in intensity between the domains. In this geometry, the propagation vector of the incident x-rays is nearly parallel to [1 1 -1], as shown in 37a, due to the θ = 30° grazing angle from the sample surface. Figures 37b-e were obtained by changing the x-ray polarization angle α and keeping the grazing incidence angle θ fixed, which allowed us to gain insight into the magnetic structure by plotting the α-angle dependence of the x-ray dichroic signal. Individual ferroelectric directions can be preferentially identified by rotating the polarization relative to the crystal as demonstrated in Figure 37c. For example, in this figure, the technique highlights all [-1 1 -1]-type ferroelectric domains (black arrow). The angle dependence reveals that at α = 70°, three of the four <1 1 1> type domains have similar contrast while the intensity from [-1 1 -1] domains is much higher. Further rotation of the polarization to α = 40° (Figure 37d) results in an image where all four ferroelectric variants can be distinguished due to their differences in contrast. Contrast between certain domain types can also vanish at other x-ray polarization angles**,** such as the [1-1-1] and [-11-1]-type domains in Figure 37e for α = 0.

Focusing on the image in Figure 37c where we have controlled the relative orientation of the incidence x-ray polarization and the crystallographic orientation of BFO to preferentially observe one ferroelectric direction (in this case all ferroelectric domains of the [-11-1]-type), we gain insight into the nature of magnetism in BFO. We note again

that all individual domains of a specific ferroelectric direction exhibit identical contrast. This indicates that the antiferromagnetic order in a given set of identical ferroelectric domains is the same, and automatically rules out the possibility of a magnetic structure such as that in a bulk sample of BFO in which there is a 111-type easy plane of magnetization perpendicular to the polarization direction. PEEM imaging in this geometry would result in multiple contrast levels for a given set of identical ferroelectric domains if the antiferromagnetic domains were larger then the PEEM resolution (~30 nm). The formation of antiferromagnetic domains with sizes smaller than 30 nm is highly unlikely, purely due to energetic considerations.[70] Therefore, the data in Figure 37c is consistent with a magnetic structure in which an easy magnetic axis is formed in the {111}-magnetization plane of BFO, similar to what is observed in strained NiO films.[41]

4.2.4 Modeling Expected Domain Contrast

Simple models of the x-ray polarization angle (α) dependence of the dichroic domain contrast further support this conclusion. From a series of images (such as those in Fig. 37b-e), we can extract the α dependence of dichroic contrast (from both ferroelectric and magnetic contributions) for thin and thick films and compare this data to model calculations as a function of the x-ray polarization angle α. The angle dependence of the magnetic contribution to linear dichroism of an antiferromagnet has been modeled[36] previously as

$$I = (3\cos^2\Theta_M - 1) \langle M^2 \rangle_T \qquad (5)$$

where M is the magnetic moment at a temperature T and Θ_M is angle between the AF axis and the incident x-ray polarization vector axis. The ferroelectric contribution is also thought to exhibit a cosine-squared angular dependence[12,71] on the angle Θ_F between the ferroelectric polarization axis and the x-ray polarization axis. To test this hypothesis, a similar angular study was completed on purely ferroelectric $PbZr_{0.2}Ti_{0.8}O_3$ (PZT) films.

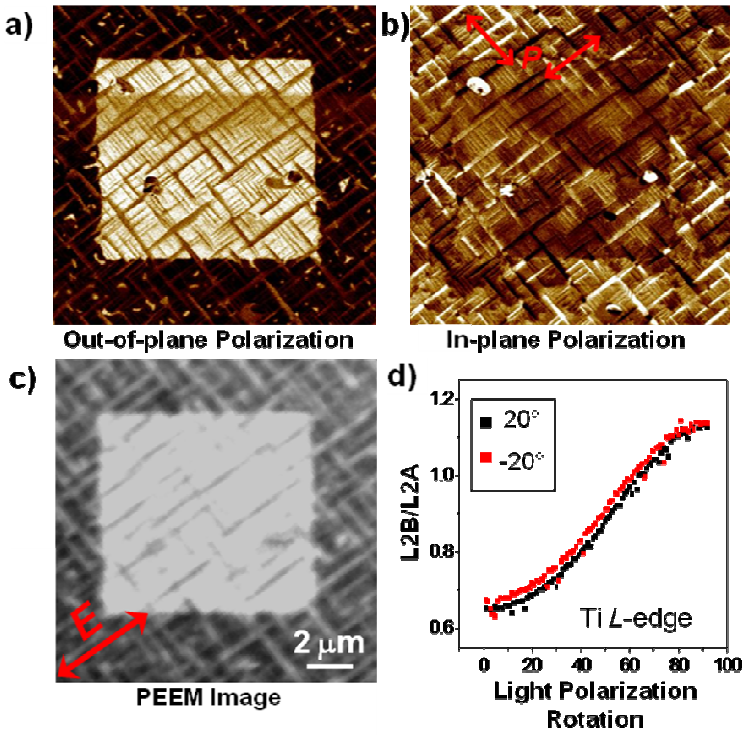

Figure 38 - PFM and x-ray measurements of ferroelectric domains on PZT. In the same location, we present (a) the out-of-plane and (b) in-plane projections of the ferroelectric directions, and (c) the PEEM dichroic contrast taken at the Ti L_2-edge. (d) The angular dependence of L_{2B}/L_{2A} as the light polarization axis is rotated by 90° taken at grazing angles of ±20°.

Measurements taken at PEEM2 reveal that there is a correlation between the ferroelectric properties and the contrast in PEEM measurements. PFM measurements, used to map the in-plane and out-of-plane projections of ferroelectric directions and also switch the out-of-plane polarization direction,[72] can easily distinguish the polarization direction(s) of each of the domains and are compared to PEEM measurements. In the same location, Figure 38 presents (a) the out-of-plane and (b) in-plane projections of the ferroelectric directions, and (c) the PEEM dichroic contrast taken at the Ti L_2-edge. Though the resolution at PEEM2 is close to the domain width, the ferroelectric directions can be clearly seen in the PEEM image. Represented by the arrows, the two in-plane ferroelectric axes make up the criss-cross pattern throughout the image.

There is also an out of plane polarization direction, best observed in Figure 38a. The out-of-plane ferroelectric direction (out of the plane or into the plane) can be controlled by application of an electric field via PFM, as was completed inside the bright box in Figure 38a in order to establish the sensitivity of dichroism to out-of-plane components as well as in-plane components. Now that this ferroelectric contribution is established with this example and other comparisions,[48] it is important to know the angular dependence of this contribution so that we can incorporate it into our dichroism model. Figure 38d shows the angular dependence of L_{2B}/L_{2A} as the light polarization axis is rotated by 90 degrees (between s- and p-polarized light). The two curves demonstrate that the same angular dependence is observed when the angle between the sample and incident light is 20 degrees on the two opposite sides of the sample surface, as would be expected if this is a ferroelectric effect due to having equivalent projections. The resulting angular behavior can be modeled by a cosine squared relation, suggesting that the ferroelectric behavior result in angular dependencies in dichroism similar to those observed due to magnetic properties.

Given this behavior, we have modeled the dichroism from a multiferroic material with both magnetic and ferroelectric order when linearly polarized light is incident upon the sample at a given temperature as

$$I_{XLD}=P\cos^2\Theta_F + Q\cos^2\Theta_M, \qquad (6)$$

where |P|+|Q|=1. Constants P and Q can be either positive or negative, where |P| and |Q| are, respectively, the percentage contribution of the polarization and magnetic components to the dichroism at the given temperature. We have considered both positive and negative values for the constants P and Q in the current study. The dashed lines in Figure 39a correspond to the selected images in Figure 37 and the colors of the curves match the in-plane projection of the ferroelectric directions and colored arrows displayed

in Figures 36 and 37. We have investigated a large number of possible magnetic structures encompassing many individual directions within the easy magnetization plane, combinations of these directions, and other possible directions not limited to that magnetization plane. Figure 39 summarizes the best matches with the data, though other possibilities are explored in Figures 40 and 41.

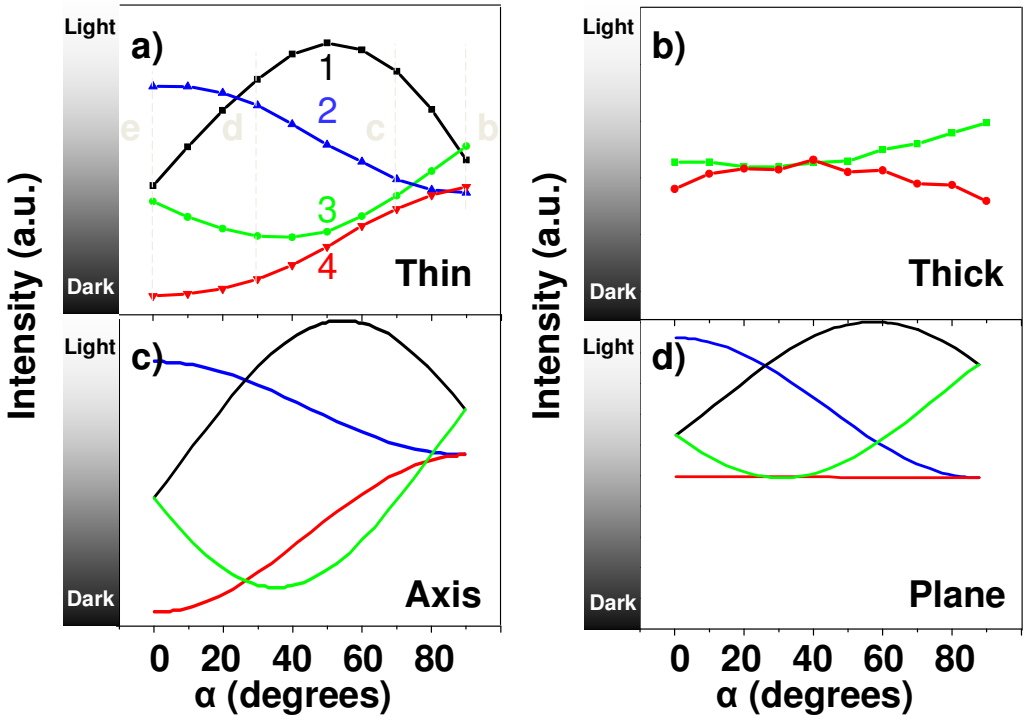

Figure 39- Comparison between experimentally measured and modeled angle dependent XLD contrast. Experimentally measured dichroic contrast as the x-ray polarization is rotated for both thin (a) and thick (b) BFO films. Models of XLD contrast for two magnetic structures, a unique magnetic axis (c) and an easy magnetic plane (d), are shown for the same sample orientation as in Figure 37.

Models of the x-ray polarization angle dependence of the dichroic contrast for the two candidate magnetic structures previously discussed—a unique magnetic axis versus an easy magnetic plane—are shown in Figures 39c and 39d, respectively. By comparing the experimentally-measured dichroic contrast (a thin film in Figure 39a and a thick film in Figure 39b) with that in the calculated angle dependencies, a clear correlation emerges.

For thin films, the data clearly indicates an easy magnetic *axis*; in contrast, for thick films, the data strongly suggests an easy magnetic *plane*. For example, the characteristic straight line expected for a ferroelectric direction along [11-1] is not observed for thin films. Also, the reduced variance between the contrast levels, demonstrated in Figure 39d is in fact observed in thicker films (Figure 39b). We note that data for only two variants are presented for the thick films (due to experimental constraints). Regardless, clear differences in the magnetic structure between thin and thick BFO films are observed, presenting the first evidence for the formation of an easy or preferred magnetic axis in epitaxially-strained thin films of BFO.

The angle-dependent data and model for thin films of BFO (Figure 3(a) and (c)) can only be achieved by two types of easy axes: [1-10] and [112] for a given [11-1]-polarization direction; other axes produce dramatically different curves. Since these two axes are perpendicular to each other, the image contrast for these two scenarios can look the same due to the fact that P and Q in Eq. **6** are variables. The sign of these variables was unknown, and therefore adding one axis is similar to subtracting the perpendicular axis. To further elucidate this fact, Figure 40a shows the resulting angular dependence if a) P = 52% and Q = -48% (112 case), or if b) P = 67% and Q = 33% (1-10 case). Note the sign difference between the Q values in the two cases, allowing these very different behaviors to result in the same angular dependence.

Figure 40 explores how the angular dependence changes for these two axes if we allow P and Q to vary. The gap circled in Figure 40a for $\alpha = 90°$ matches nicely with thin film

data (Figure 37a). However, as the P value is lowered for both axes (Figure 40b), this gap disappears, which does not fit the observed dependence for any thickness of BFO. As P is lowered further, this gap actually reverses as seen in Figure 40c. The act of increasing P (instead of lowering it) results in an enlargement of the gap (Figure 40d), which is also not found. It is clear that there is only a narrow range of P values that agree with the angular dependence and this range is consistent with prior data.

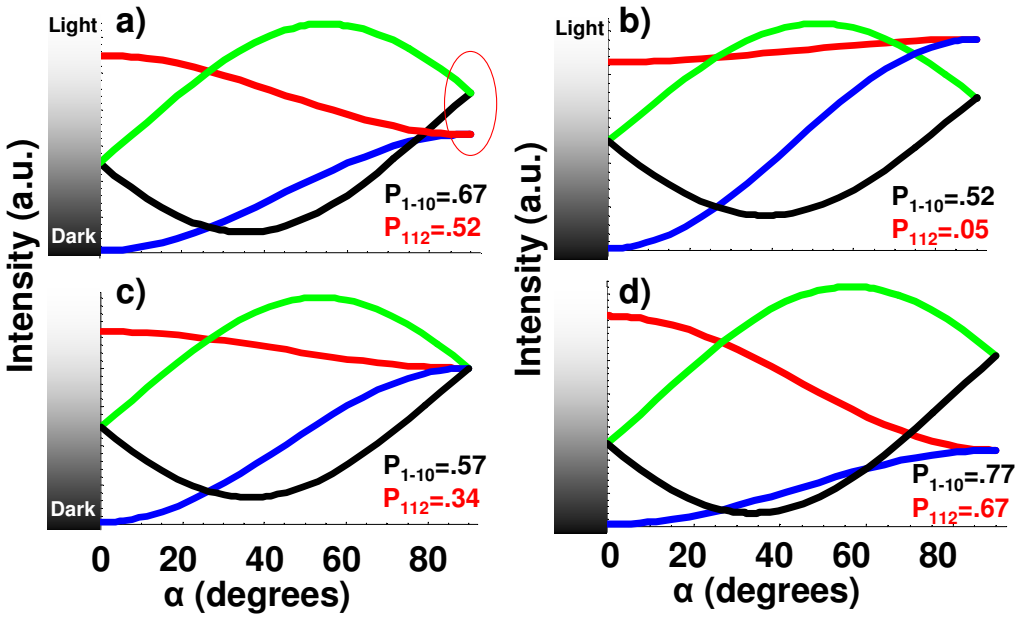

Figure 40 – The effect of the P values on the expected angular dependence of PEEM contrast for two possible magnetic axes: [1-10] (black) and [112] (red). The same curves are obtained for two different P values when the opposite magnetic axis is considered.

Previous temperature-dependent measurements (discussed in Chapter 3) have shown that the percentage of the dichroism at room temperature originating from the ferroelectric polarization (P) is approximately 60 ± 10%.[47] Unfortunately, the curves that best match the observed angular dependence result from one of two cases (P_{112}=.52 or $P_{1\text{-}10}$=.67) that are within the experimental error. In order to uniquely identify this axis, we have carried out a unique set of temperature-dependent measurements.

The two possible types of easy axes, <1-10> and <112>, should exhibit different temperature dependence of the intensity distribution when imaged, for instance at α=0° (Fig. 37a). For the case of a <1-10> preferred axis, the magnetic axis for the domains with the largest contrast (2 and 4 at section e in Figure 37a) is perpendicular to the electric field vector of the incident x-rays. Thus, the difference between these two domains is dependent only on the contribution from ferroelectric polarization (P), which does not change appreciably over this temperature range.[47] However, in the case of a <112> preferred axis, the axis is not perpendicular to the electric field vector of the x-rays, and therefore a definite temperature dependence arising from the magnetic contribution to the dichroism can be expected. Equation 6 can be adapted to variable temperature measurements by requiring both P and Q to be a function of temperature. Recognizing that the ferroelectric polarization in BFO does not change appreciably over the temperature range from room temperature to the Néel temperature (~370°C),[47] we focus on the temperature dependence of Q, which should go to zero at the Néel temperature.[73] From this, one can then estimate a ~40% reduction in total intensity at the Néel temperature (370°C) and, by interpolation, a ~20% reduction in contrast should be achieved from room temperature to 200°C.

Figure 41 illustrates the contrast between these domains (2 – light grey and 4 – black) that has been repeatedly taken at room temperature (Figure 41a) and at 200°C (Figure 41b). These images exhibit four shades—white, light grey, medium grey and black. Light grey and black correspond to the domains with the largest contrast (domains 2 and 4), whose temperature dependence determines which magnetic axis is present. The medium

grey is achieved for both 1 and 3 domains. As illustrated by the several 2/4 locations plotted in Figure 41c, the contrast was found to decrease by ~17% upon heating, which is in reasonable agreement with the <112> easy axis scenario. Continued contrast reduction was observed at higher temperatures, but sample damage at these temperatures began to threaten sample integrity and therefore data beyond 200°C has not been included. Measurements have been completed on a blank BFO film and also on films capped with a 2 nm thick layer of SRO pre-heated for one hour at 200°C in an attempt to minimize the impact of any surface chemistry effects. The same trend expected for the <112> case was observed in all cases.

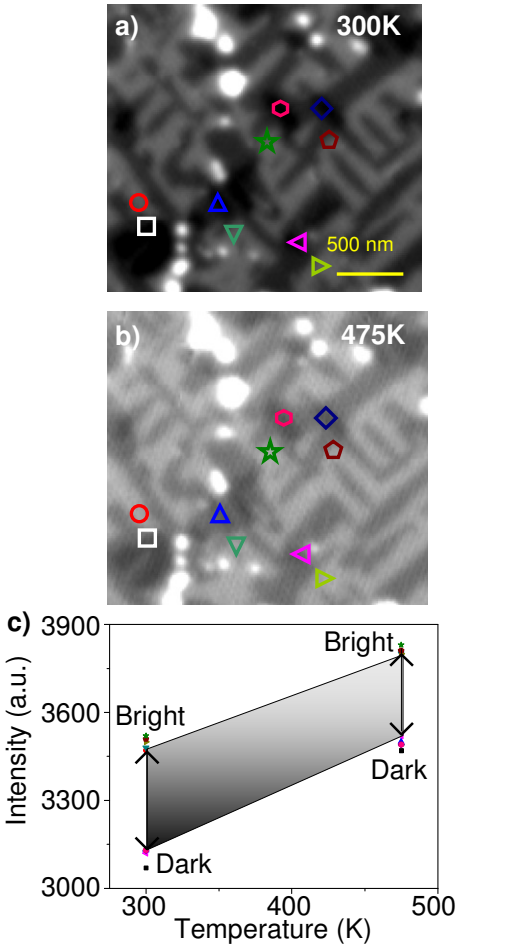

Figure 41 - Temperature dependent dichroism measurements of BFO. XLD images taken at (a) room temperature and (b) 200°C. The labeled spots in (a) and (b) represent a selection of locations used to probe the temperature dependent change in dichoric contrast. (c) Temperature dependent changes in intensity for type 2 and 4 domains for both temperatures reveals that the difference between the contrast from type 2 and 4 domains reduces by 17% at 200°C. This is expected for the presence of a preferred magnetic [112] axis.

Both angle- and temperature-dependent PEEM measurements support the case for a preferred [112] magnetic axis for BFO thin films grown on STO substrates, where a strain of ~1% exists. BFO films of thickness ~200 nm instead show magnetic behavior consistent with the magnetic plane observed in BFO single crystals. This change with thickness is not observed in BFO films grown on DSO, where the lattice mismatch is very small. The

strain in the DSO samples appears not to be large enough to affect the magnetic behavior. Finally, preliminary findings suggest that BFO films under tensile strain (for example, by epitaxial growth on Si) demonstrate the opposite axis preference within the (11-1), i.e., the in-plane <1-10>.

4.3 Ultrathin Films

What happens to the order parameters if larger strains are applied as can be found in ultrathin thin films of BFO (thickness < 20 nm) on STO? Size effects in magnetic[74-75] and ferroelectric[64,76] materials have been extensively studied over the years, and these studies have demonstrated that there is indeed a minimum thickness required to stabilize the order parameters needed for device functionality. Prior studies on size effects on ferroelectricity in ultra-thin BFO films[64] have demonstrated that ferroelectricity is present down to a film thickness of ~2 nm, but no study has yet examined the evolution of magnetic order in ultra-thin films. Figure 42 shows the XMLD asymmetry for BFO films ranging in thickness from 50 to 2 nm. The XMLD spectroscopic measurements were completed by comparing spectra taken at $\theta = 70°$ to $\theta = 33°$ ($\alpha = 90°$) at beamline 7.0.1 at the ALS and are fit based on thickness as the single exponential variable. There is a progressive decrease in the magnitude of the asymmetry at thicknesses below ~15-20 nm, which corresponds very closely to the onset of similar size effects in antiferromagnetic CoO.[74] Similar to the reduction of critical temperature observed in superconducting or ferroelectric thin films, antiferromagnets exhibit a loss in magnetic order when the film thickness approaches the material's correlation length. In turn, this diminished magnetic

order in these ultra-thin BFO films deleteriously affects the interactions of the BFO layer with a ferromagnet via exchange coupling at an interface.[77] Data in Fig.42 shows the magnitude of the exchange bias field for a 5nm thick ferromagnetic $La_{0.7}Sr_{0.3}MnO_3$ layer for various thicknesses of BFO. The magnitude of exchange bias (i.e., the anisotropic shift of the magnetic hysteresis loop of the ferromagnet) falls off concurrently with the diminished XMLD asymmetry (Fig. 42). Such a reduction in exchange bias as a result of diminished antiferromagnetic order has been observed in many classic exchange bias heterostructures.[37] Although exchange coupling with BFO is not the primary focus of this research, the fundamental mechanisms by which both the order parameters begin to be suppressed with dimensions (i.e., film thickness) is an area that merits further detailed studies. From an application perspective, it is clear that the evolution of magnetic order in thin films of multiferroics is a critical subject to study if researchers hope to develop a new generation of devices that utilize these exciting materials.

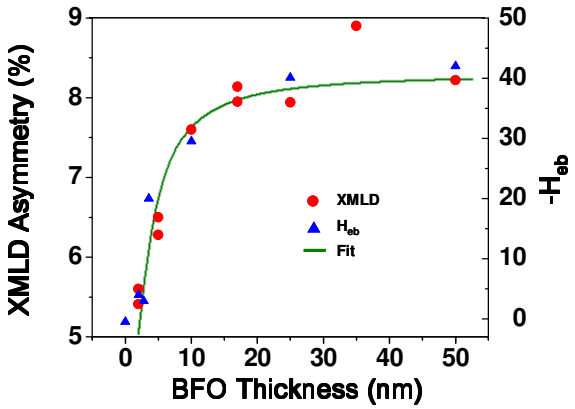

Figure 42 - (in red, left axis) The XMLD asymmetry as a function of thickness for BFO thin films. Below a BFO thickness of 20 nm, a reduction in the antiferromagnetic order is observed. Asymmetry was measured by comparing spectra taken at θ = 33° and θ = 70° (α = 90°). (in Blue, right axis) The anisotropic shift of the magnetic hysteresis loop of the ferromagnet $La_{0.7}Sr_{0.3}MnO_3$ on BFO falls off with BFO thickness, concurrently with the diminished XMLD asymmetry. The fit is based on a single exponential variable.

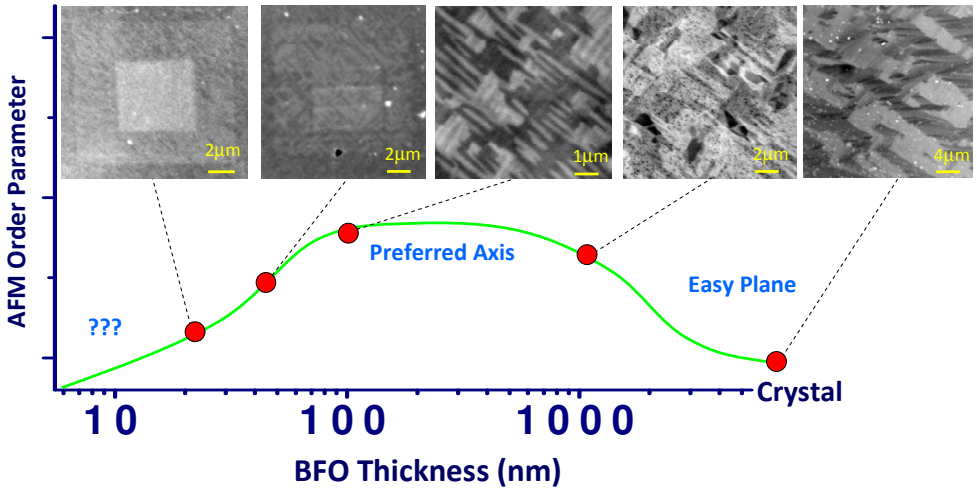

Figure 43 – Evolution of BFO magnetism. PEEM images of 5 representative samples of a variety of thicknesses are shown. The green line qualitatively describes the change in the magnetic order.

4.4 Summary of BFO Thickness Effects

The evolution of magnetism in BFO films discussed in this chapter is qualitatively summarized by the PEEM images of five BFO samples of different thicknesses (22 nm to bulk crystal) in Figure 43. The domain pattern changes quite considerably over this range of thicknesses. In the crystal, we see very large ferroelectric domains with variation within the domains, suggesting a rotation between axes consistent with the easy plane case. To my knowledge, this is the first PEEM image of a BFO crystal, likely due to the difficulty in obtaining a clear image when the surface is rough. As we reduce the thickness of BFO, this easy plane simplifies into a preferred axis, resulting in a strong magnetic anisotropy along that direction. Finally, at some ultrathin thickness, BFO starts to lose its antiferromagnetism. This progression demonstrates that use of both strain (controlled by film thickness and substrate choice) and electric field (discussed in Chapter 3) to control the magnetic directions and strength of BFO which will be vital for device design as illustrated in Figure 44.

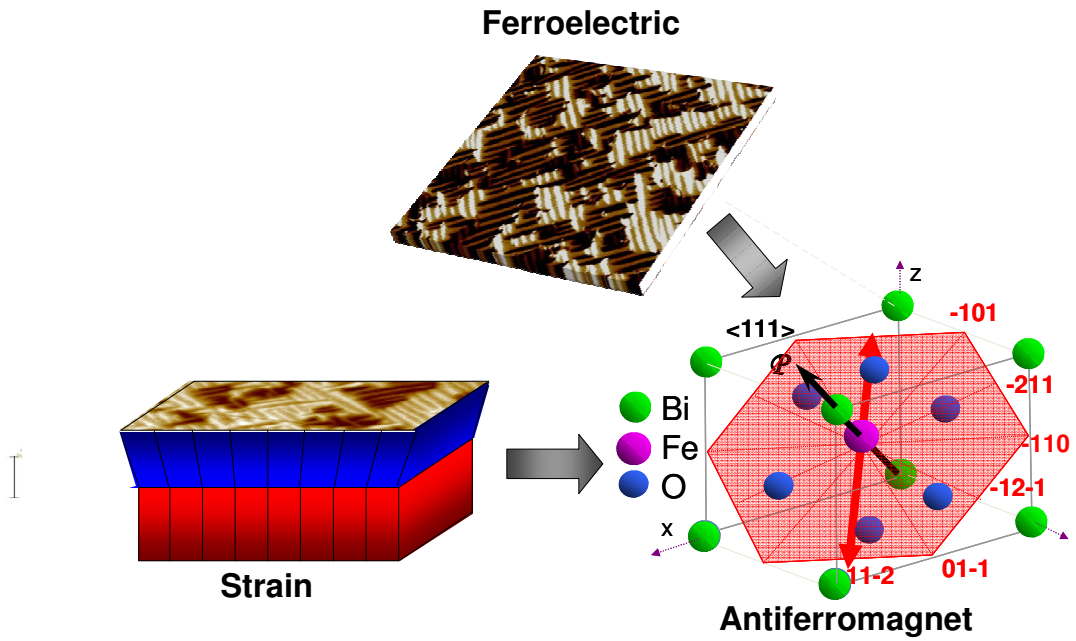

Figure 44 – Schematic illustrating that the antiferromagnetic properties of BFO(001) films can be controlled through both strain and the electric field control of the ferroelectric domains.

Chapter 5: Orientation Influences on Magnetic Order

This chapter introduces the influence of film orientation on the magnetic properties in BFO thin films. 110 and 111 orientations are introduced as alternatives to the 001 structure discussed throughout the rest of the thesis. The differences in the ferroelectric nature for each orientation are presented. XAS and PEEM are utilized to determine the magnetic behavior in the 110 and 111 orientations of BFO. Finally, the differences between the three orientations are summarized.

5.1 Comparison of Ferroelectricity in BFO Orientations

The previous chapter discussed the in-depth understanding of the magnetic behavior of BFO(001) films. This particular orientation of BFO was selected due to the several ferroelectric directions present in these films as shown by the unit cell schematic and IP PFM image in Figure 45a. By control of growth parameters presented in Appendix A, the number of ferroelectric directions present in the BFO(001) film can be selected; one can choose to create a sample having all 8 ferroelectric body diagonal directions, the four downward pointing directions, only two, or a monodomain sample. Though the presence of multiple ferroelectric directions in BFO(001) films was ideal for distinguishing the magnetic behavior, one could argue that fewer directions would be more ideal for most engineering applications. Now that several critical parameters in the 001 case have been determined, such as the sign and magnitude of the *p* value in the multiferroic dichroism formula, this knowledge can be applied to the study of other orientations of BFO.

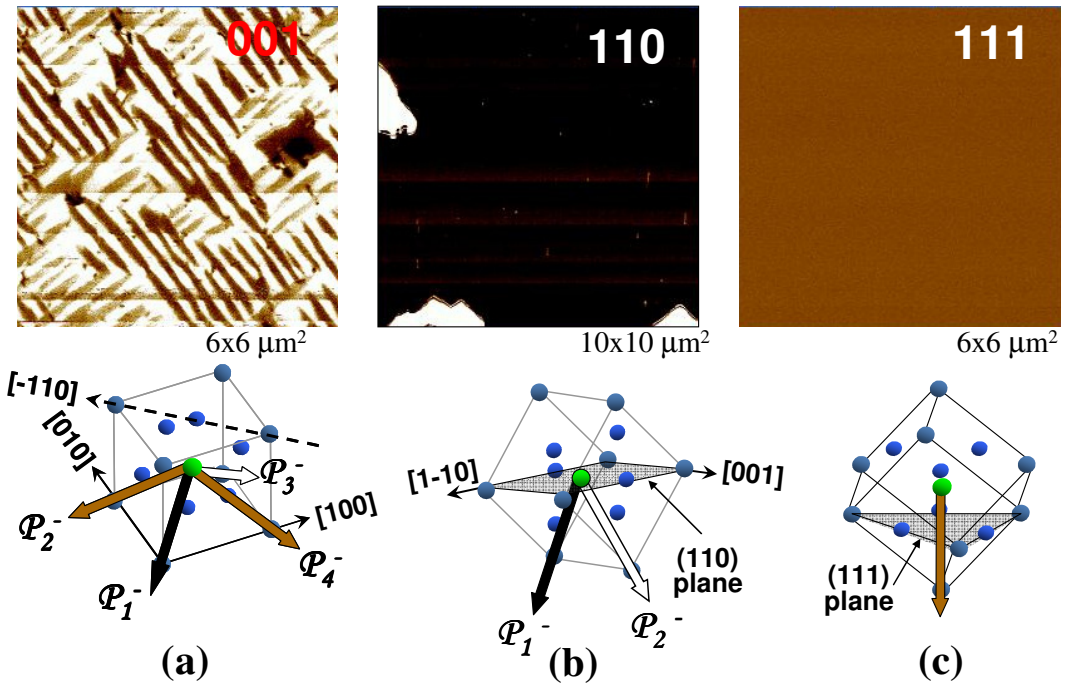

Figure 45 – Schematic and IP images of (a) 001, (b) 110, and (c) 111 orientations of BFO films.

110 and 111 orientations as well as their IP PFM images are shown in Figure 45b and c respectively. BFO(110) typically results in two ferroelectric directions. The percentage of each type of domain (from zero to one hundred percent) can be roughly selected based on growth parameters. BFO(111) is a monodomain sample with the ferroelectric direction pointing straight into the surface of the film. This OOP orientation is ideal for some device architectures.

5.2 Magnetism in 110 BFO films

Let us now investigate the case of the 110 orientation of BFO in greater detail. As for BFO(001) films, high-quality epitaxial $BiFeO_3$(110) thin films were grown via PLD on

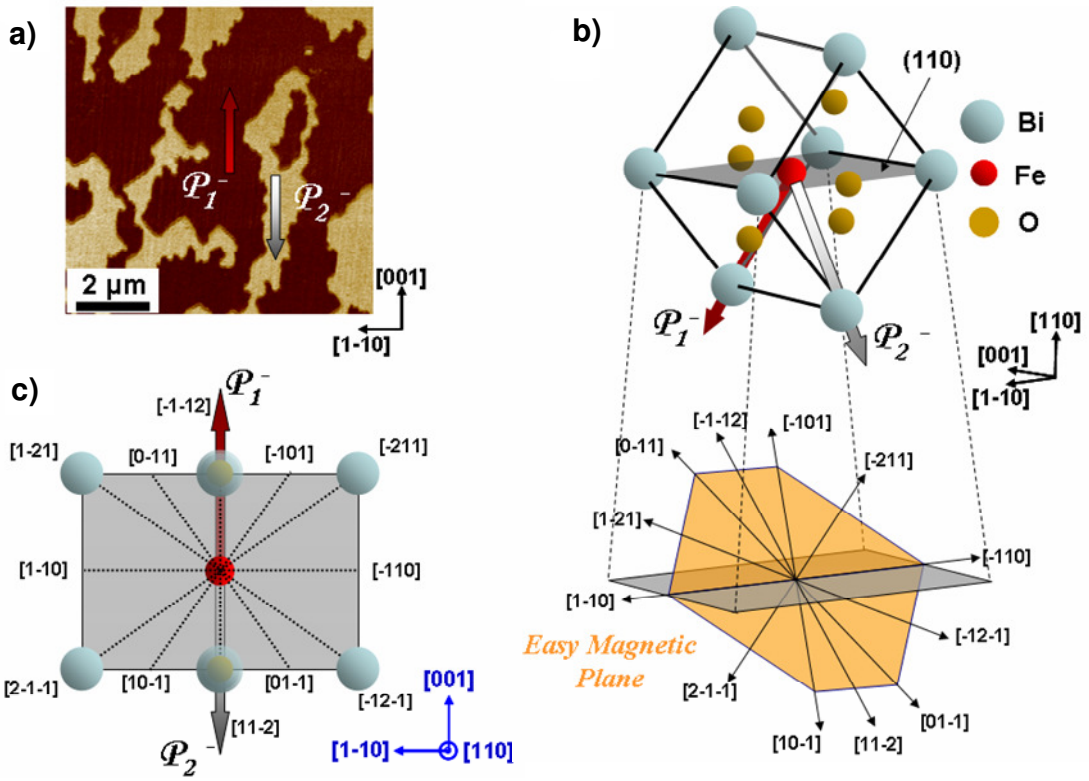

Figure 46 – BFO(110): IP PFM image of two ferroelectric domains (a) along with polarization and antiferromagnetic direction schematics (b) and projections onto the 110 surface (c).

$SrTiO_3$ substrates with a 50-nm-thick conducting $SrRuO_3$ bottom electrode and the resulting ferroelectric domain structures were studied by PFM. As illustrated in the in-plane PFM image in Figure 46a, films were controlled to have two ferroelectric directions of approximately equal volume fractions. The antiferromagnetic plane corresponding to one of the two polarization variants is schematically illustrated in Figure 46b. In Figure 46c, the projections of ferroelectric polarization directions (red and grey arrows) and their corresponding projections of the six degenerate directions in the antiferromagnetic (111) plane (dotted lines) are shown in the same figure.

The influence of strain is again studied through the systematic control of the thickness of BFO films, thereby manipulating lattice mismatch induced heteroepitaxial strain. Thin films of thicknesses varying from a few nm to several microns were prepared by both pulsed laser deposition and chemical vapor deposition. We specifically focused on two representative thicknesses, namely 120 nm (thin) and 800 nm (thick) for our photoemission experiments. The strain state of $BiFeO_3$ thin films was analyzed by using detailed four-circle x-ray diffraction measurements. Reciprocal space maps (RSM's)[78] were obtained around the (221) and (310) peaks for both samples The results of these scans are shown in Figure 47a-d. The black dashed lines in the RSMs are guides to identify the position of the reflection from the substrate. From these maps, we have extracted the lattice parameters for the BFO unit cell in both cases. The schematic diagram of the strained pseudo-cubic unit cells are presented in Figure 47e for the 120 nm film and in Figure 47f for the 800 nm film. Cyan rectangles represent the (110) plane of STO. To describe the strain states quantitatively, a monoclinic unit cell is introduced

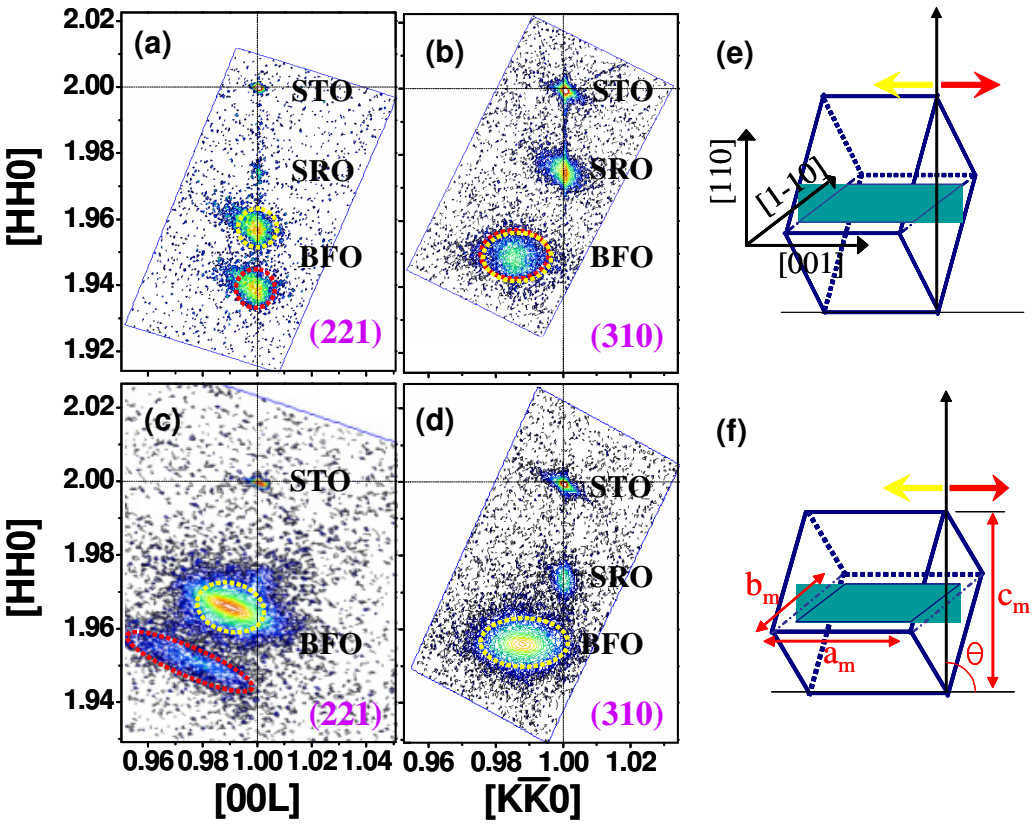

Figure 47 - X-ray diffraction results for BFO films grown on (110) STO. (a) RSM around (221) peak for 120 nm thick film; (b) RSM around (310) peak for 120 nm thick film; (c) RSM around (221) peak for 800 nm thick film; (d) RSM around (310) peak for 800 nm thick film. Black dashed lines in the RSMs are guide lines for the position of substrate. The schematic diagram of the strained pseudo-cubic unit cells are presented in (e) for 120 nm film and in (f) for 800 nm film. Cyan rectangles represent the (110) plane of STO.

whose lattice parameters (a_m, b_m, c_m, and θ) are described in Figure 47f. These x-ray measurements clearly reveal the following: the thinner film is fully strained in-plane along the [001] direction but is relaxed along the in-plane [1-10] direction. In contrast, in the thicker film, both in-plane directions are relaxed. The monoclinic *c*-axis is tilted toward [001] or [00-1], which are described respectively by yellow and red arrows in the schematics,. These tilts induce the BFO peak splitting in the (221) RSMs. The colors of the dashed circle in the RSMs indicate the origin of tilt direction. The calculated lattice parameters are a_m=3.905, b_m=5.609, c_m=5.670, and θ = 89.28 for 120 nm thin film; and

a_m=3.943, b_m=5.593, c_m=5.647, and θ = 89.20 for 800 nm thick film. Thus, the thinner film is under a higher compressive stress which is significantly relaxed in the thicker film. Furthermore, this stress appears to be anisotropic; it is essentially relaxed along the [1-10] in-plane direction, while it is fully strained along the [001] in-plane direction. This anisotropy is different from the BFO(001) film, which is strained in all in-plane directions, and this difference can result in different magnetic behavior.

To probe antiferromagnetism, we again use dichroism measured at beamline 4.0.2 of the Advanced Light Source. Angle-dependent x-ray absorption spectra were obtained in normal incidence by changing the polarization angle with respect to the substrate in-plane direction. Figure 48a shows typical absorption spectra at Fe L_3 and L_2 edges with an angle between the [1-10] crystallographic direction of the $SrTiO_3$ (STO) substrate and x-ray linear polarization vector of 0º and 90º. The XMLD spectrum (i.e. the difference between these two absorption spectra} is also shown in Figure 48a. We note that this XLD value is similar to that observed in the pure antiferromagnet, $LaFeO_3$.[79]

We next measured the azimuthal angle dependence of the Fe- absorption edge for the thin film (100nm), with a focus on the Fe L_{2A} and L_{2B} edges, as depicted in Figure 48b. When the x-ray linear polarization vector is parallel to the [1-10] crystallographic axis of STO(i.e., $\alpha = 0^o$), L_{2A} and L_{2B} peaks have the minimum and maximum intensities, respectively, and thus the L_{2A}/L_{2B} ratio shows the minimum value. By increasing the azimuthal angle, the L_{2A}/L_{2B} ratios continuously increased from 0.773 at $\alpha = 0^o$ to 1.279 at $\alpha = 90^o$; this trend of the spectral change is also found in Fe L_{3A} and L_{3B} edges. The

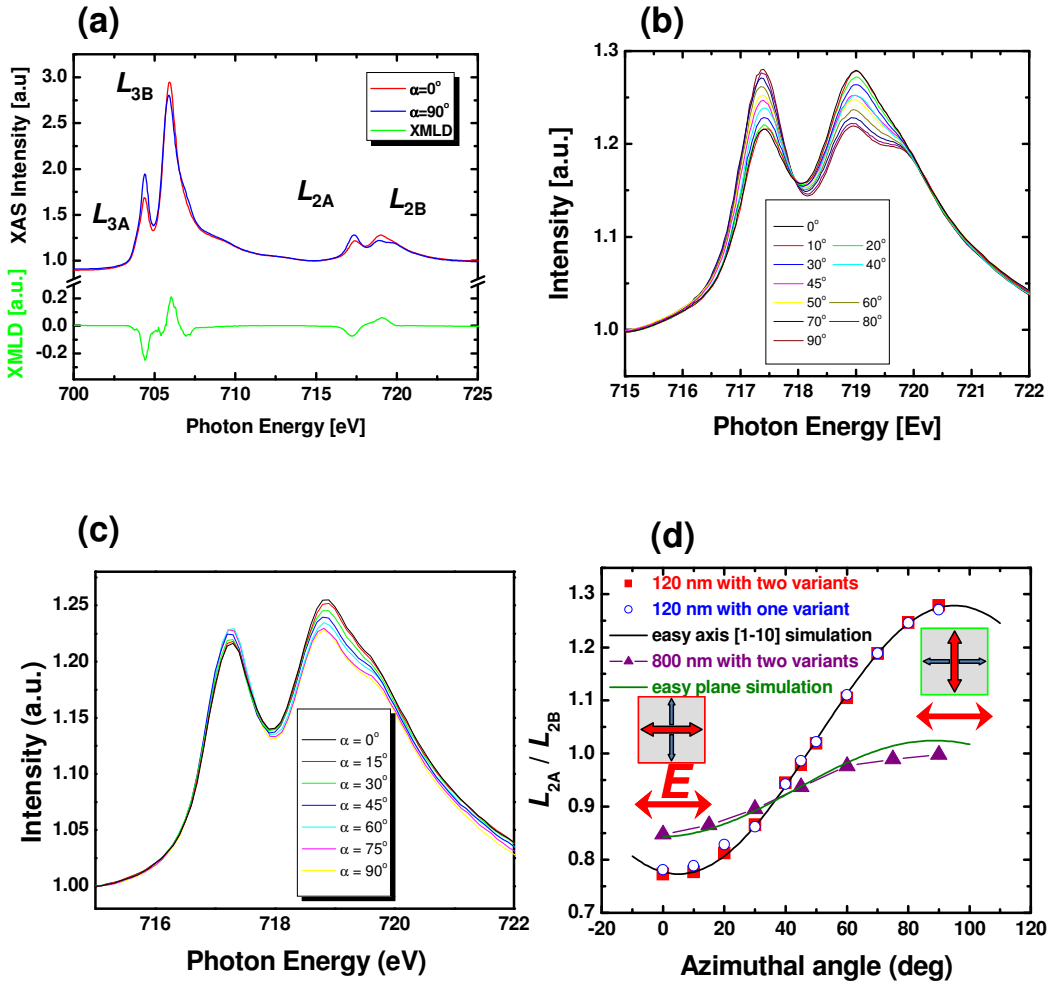

Figure 48 - (a) X-ray magnetic linear dichroism spectra (green) taken from the XAS at 0° (red) and 90° (blue) azimuthal angle. XAS near to Fe L_2 edge of $BiFeO_3$ thin films ((a)120 nm and (b) 800 nm) and with two ferroelectric domains as a function of azimuthal angle between [1-10] axis of $BiFeO_3$ thin film and x-ray linear polarization vector. (d) The calculated L_{2A}/L_{2B} peak intensity ratios (solid red square) from XAS of 120 nm $BiFeO_3$ as a function of azimuthal angle and fitted cosine square curve (line). The open blue circles represent the XAS of mono ferroelectric domain $BiFeO_3$ films. The solid purple triangles represent the XAS of 800 nm $BiFeO_3$ films. The green curve is the calculated angle dependence of the L_{2A}/L_{2B} ratios in the case of the easy plane of magnetization: the calculations were carried out using a simple averaging procedure.

corresponding angle dependence for the thick film (800nm) is shown in Figure 48c. Figure 48d summarizes and compares the angle dependence of the L_{2A}/L_{2B} ratio for the thin and thick films. There are two noteworthy features in this data: first, the L_{2A}/L_{2B} intensity ratio can again be described well with a $\cos^2\theta$ relation. More quantitatively, with the L_{2A}/L_{2B} ratios of 0.773 and 1.279 at their corresponding azimuthal angles of 0 and 90°, the L_{2A}/L_{2B} ratios can be fit to the functional form given by:

$I_{XMLD} = 1.279 - (1.279 - 0.773) \times \cos^2(\theta - 5)$. (The offset angle of 5° is likely due to a small but unavoidable misalignment of the sample with respect to the beamline.) The angle dependence of L_{2A}/L_{2B} ratios with $\cos^2\theta$ dependence on the in-plane angle strongly suggests the emergence of a unique magnetic anisotropy along either the [1-10] or [11-2] axis.

In contrast, for the 800nm thick film, the total magnitude of XLD is significantly reduced as shown in Figure 48d. The dramatic drop in the L_{2A}/L_{2B} ratios for the thicker sample is a key indicator of the evolution of the magnetic structure into an easy plane as a function of thickness. The angle dependence of the L_{2A}/L_{2B} ratios in the case of an easy plane of magnetization can be estimated (in a first approximation) as the weighted average of the individual contributions from each of the six possible magnetization directions in the (111) plane, where the preferred axis makes 50% of the magnetic directions. In the case of the (110) oriented film, one has to account for the projection of these directions onto the (110) plane (as described in Figure 46d) as well as the relative azimuthal angles between these projected directions and the x-ray polarization direction. The green curve in Figure 48d shows the calculated angle dependence of the L_{2A}/L_{2B} ratios for the easy plane scenario: the reasonably good agreement with the experimental data strongly suggests that the thicker sample indeed has evolved into an easy plane magnetic structure.

There is therefore strong evidence that a preferred magnetic axis is also present in thin BFO(110) films, but which axis is it? Again, the currently presented data is not sufficient to determine between there two perpendicular cases of [1-10] and [112]. The reason for

this is that the P value found for BFO(001) is so close to 50% that a small deviation results in the same behavior for each case, much like in the other BFO orientation.[69]

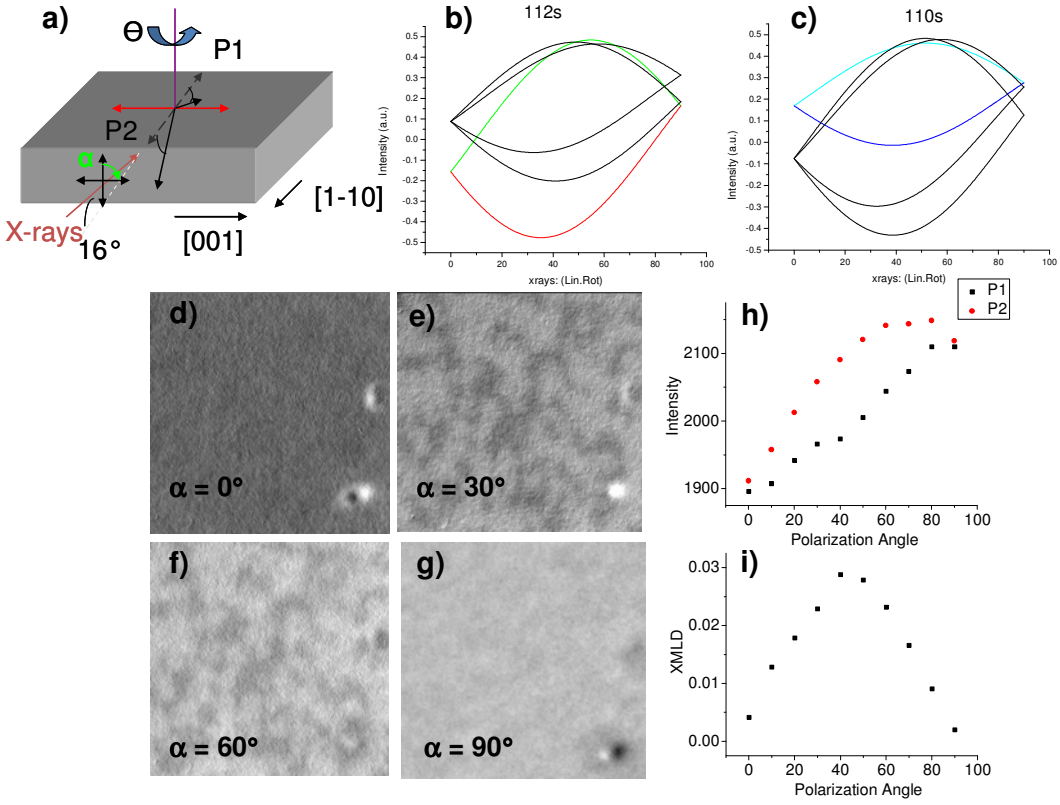

Figure 49 – X-ray incident at Θ=90° results in similar contrast expectations for both [1-10] and [112] case. a) Schematic illustrating experimental geometry. Expected curves for all (b) <112> and (c) <110> axes within the two present ferroelectric {111}. PEEM images for (d) α = 0°, (e) α = 30°, (f) α = 60°, and (g) α = 90°. Finally, the (h) intensity and (i) difference in intensity is plotted for both ferroelectric directions.

This point is further clarified by angular dependent PEEM images and the modeling of their contrast as displayed in Figure 49. Figure 49a shows the orientation of the incident x-rays. Note that the angle from the sample is now 16 degrees instead of 30 degrees, because these images were taken at the Swiss Light Source rather than the ALS. Figures 49b and c are the expected curves based on the multiferroic formula present in the last chapter (P = 50%) for all of the <112> and <110> axes within the two present

ferroelectric {111} planes. The colored curves in each set represent the two perpendicular [112] and [1-10] for each corresponding ferroelectric direction, and are therefore the expected two curves representing the angle dependences of the BFO domains. Unfortunately, they look exactly the same since we cannot determine the exact scale of the contrast. The behavior is approximately observed in PEEM images (Figures 49d-g). The intensities of these images (Figure 49h) and the difference between the two (Figure 49i) illustrate that the maximum difference between the domains is achieved at $\alpha = 45°$, as anticipated. Axes outside of the (111) plane would result in very different expectations.

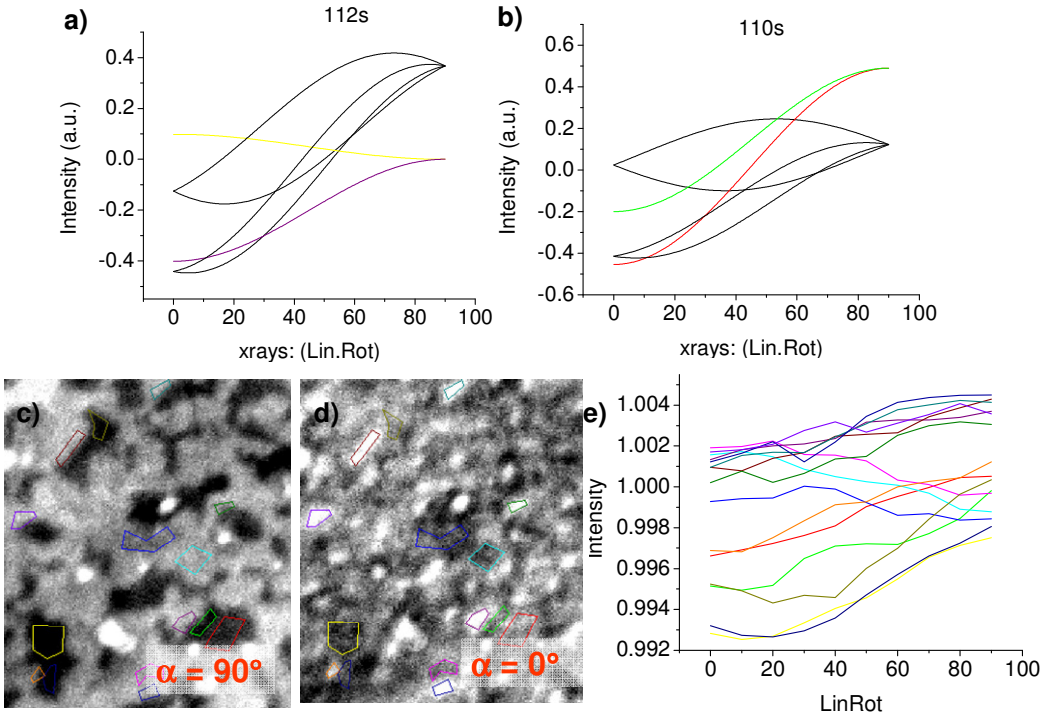

Figure 50 - X-ray incident at Θ=0° results in different contrast expectations for [1-10] and [112] cases. curves for all (a) <112> and (b) <110> axes within the two present ferroelectric {111}. PEEM images for (c) α = 90° and (d) α = 90°. The angular dependence with x-ray polarization rotation of the intensity for the colored boxes shown in (c-d) is shown in (e). Colors match lines.

To distinguish between these two axes, a sample rotation of 90° is necessary. This rotation results in vastly different behavior, as observed in Figure 50. First, note that the expected angular dependencies for <112> (Figure 50a) and <1-10> (Figure 50b) are quite different for the colored perpendicular axes. Figure 50c shows the same blotchy ferroelectric domain pattern as previous samples, but Figure 50d (taken in the same location for a different x-ray polarization) reveals new behavior. Though the contrast is weak in this image, one can see that the blotchy ferroelectric domain pattern has broken up. This variation suggests that in BFO(110) thin films, there may not be a single magnetic direction within each ferroelectric direction. Further analysis of the angular dependence of several locations, such as the individual domain intensities in Figure 50e, reveals a <112> easy axis behavior, as these directions are the only magnetic possibilities that have an angular dependence with a concave decrease in the intensity with increased x-ray polarization rotation (yellow in Figure 50e).

In summary, the microscopic and macroscopic antiferromagnetic anisotropy in multiferroic $BiFeO_3$ thin films on $SrRuO_3/SrTiO_3$(110) substrates was investigated by XAS-XLD. The large XLD due to the presence of antiferromagnetic axes along the <112> in an epitaxially-strained film was found by angle-dependent XAS. The antiferromagnetic domains appear to break up within the ferroelectric directions, which may not be ideal for devices as there would exist no specific magnetic direction. Thick BFO(110) films have angular dependencies consistent with the same plane behavior seen in BFO(001) films and crystals.

5.3 Magnetism in 111 BFO films

Unlike BFO(001) and BFO(111) films, BFO(111) films result in only one ferroelectric direction that points into the surface plane. Some believe that this perpendicular ferroelectric orientation is ideal for device applications, partly due to allowing the greatest out-of-plane spontaneous polarization. Due to this geometry, in-plane strain resulting from growth on a substrate would be symmetric across the perpendicular magnetic (111) plane. There is therefore no reason for the energy degeneracy of the six magnetic axes to be broken, and thus no magnetic axis should be selected. This hypothesis was tested using similar angle-dependent x-ray absorption measurements as have been presented previously.

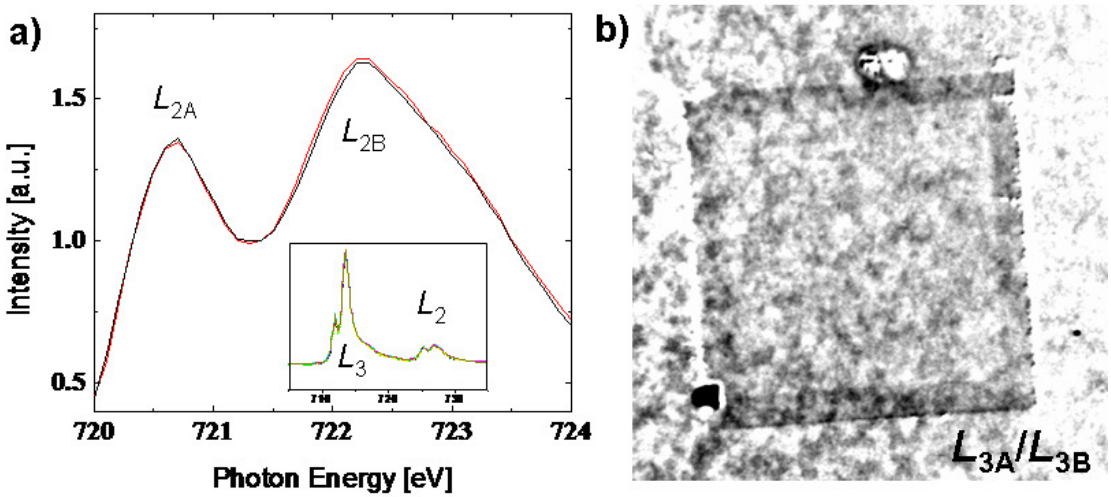

Figure 51 – X-ray absorption spectra and dichroism images of BFO(111) thin films. (a) Close-up of Fe L_2 edge along with full L-edge spectra (inset). (b) Fe L_3 PEEM image.

An initially curious result is observed—nothing. Despite several attempts and the same quality of films as other orientations of BFO (as determined by the same XRD and PFM quality control techniques), no dichroism is observed in any BFO(111) film. This lack of dichroism is observed through the sample's Fe L_2 edge spectra for horizontally and

vertically polarized light in Figure 51a. The inset of this figure demonstrates another example sample, showing no difference for both the L_3 and L_2 edges. Yet, when PEEM images were taken, the image was not uniform like PFM images, such as Figure 45c. Figure 51b is the PEEM image which resulted from dividing images from energies taken at the L_{3A} and L_{3B} peaks. The box shape visible in Figure 51b is due to electrically poling the sample OOP, which was performed to investigate possible differences after electric field poling; no differences were observed. The lack change between poled and unpoled areas is an indication that there may not be electrical control of the magnetism. Recall that electrical control is theoretically possible only for 71° and 109° ferroelectric switching, whereas the only switching allowed in BFO(111) is 180° switching. Though the (111) plane make limit the possible magnetic directions, no electrical control is observed.

The more curious behavior in Figure 51b is the large variation in PEEM contrast despite no dichroism from x-ray absorption spectroscopy. The variation in contrast is quite similar to the antiferromagnetic domains observed in $LaAlO_3$ thin films.[34] Since the ferroelectric contribution should be the same over the entire monodomain sample, we could then be sensitive to only the magnetic component. If we have magnetic contribution, why do we not observe something in the spectra? One might be tempted to believe that the antiferromagnetic directions are random, canceling out any dichroism in XAS. This cannot be the case because there would still be a ferroelectric contribution to the dichroism apparent in the spectra, which is not observed. All evidence points to the possibility that the magnetic and ferroelectric contributions are canceling each other.

After some thought, this is not so surprising. We now know that the percentage of ferroelectric contribution (P) is roughly 50%. Therefore, if we are summing contributions from [111] and the perpendicular magnetic plane with equal weights, they could easily cancel. The lack of dichroism in high-quality films coupled with the large variation in PEEM images in thin films of BFO(111) suggests that we also have easy magnetic plane behavior in this orientation. The reason for this magnetic easy plane behavior (instead of the easy axis behavior observed in 001 BFO) is likely due to the fact that the strain is applied symmetrically over the (111) magnetic plane and does not select any preferred axis.

5.4 Summary of Orientations

There are many differences between the three presented orientations of BFO. The number and direction of ferroelectric directions for each orientation is different, as summarized by Figure 45. Strain affects the perpendicular magnetic (111) plane in different ways, resulting in different magnetic behavior in thin films among the three orientations. Unlike BFO(001) thin films, BFO(110) and BFO(111) films have magnetic domains that do not correspond perfectly with the ferroelectric domains. Instead, the magnetic domains break up within each ferroelectric domain, presenting a potential problem for the manipulation of magnetism in devices. Nonetheless, this chapter illustrates that orientation [complementing electric field (Chapter 3) and strain (Chapter 4)] is another method for controlling magnetism in BFO.

Chapter 6: Electric Control of Ferromagnetism

Previous chapters have focused on the understanding and control of antiferromagnetism in BFO films. Despite much effort, no electrically controllable room temperature ferromagnetism had been achieved for BFO or any other material system. This desirable result was achieved through exchange bias of antiferromagnetic BFO with a ferromagnetic layer grown on top of it. This chapter will discuss the background of exchange bias, the concept behind electrically-controllable exchange bias, and the data supporting its existence in BFO/FM thin film heterostructures.

6.1 Exchange Bias Background

Exchange coupling between ferromagnetic and antiferromagnetic films across an interface can cause a shift in the ferromagnet's hysteresis loop, called exchange bias. Despite the use of exchange bias in a wide variety of applications, including magnetic recording media[80-81] and permanent magnets,[82] there are still many unresolved questions in the field involving the effects of film thickness, interface roughness, spin configurations, repetition (training), and interface disorder.[37] Notwithstanding the lack of consensus of the details influencing its behavior, qualitatively the idea behind exchange bias is intuitive. This behavior is summarized in Figure 52. Initially (1), a magnetic field **H** is applied. If the temperature is below T_c for the ferromagnet, the spins will align along the direction of the field. However, if the temperature is above the Neel temperature (T_N)

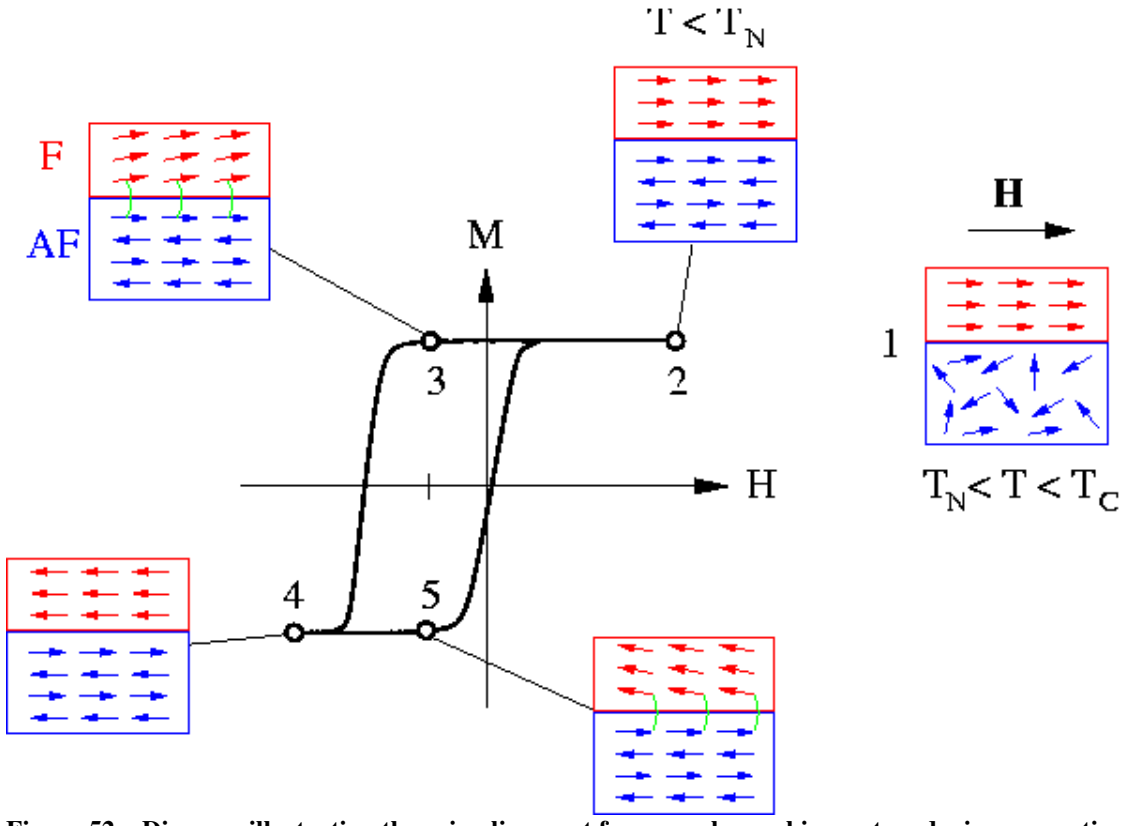

Figure 52 – Diagram illustrating the spin alignment for an exchange bias system during magnetic cycling.[83]

of the antiferromagnet, the spins in the AFM point randomly. If the external field remains while the heterostructure is brought to a temperature below T_N, the exchange interaction across the interface will cause the top layer of AFM spins to point parallel to the spins in the FM (2). As this alignment minimizes the energy of the system, so does the propagation of spin alignment—alternating between parallel and antiparallel—through the rest of the antiferromagnet leading to no net magnetization (2). Applying a small field in the opposite direction (3) would typically make a ferromagnet reverse its spin direction. Since the antiferromagnetic spin configuration will not change, the ferromagnet feels some pressure to remain aligned with the top antiferromagnetic layer. Continuing to increase this magnetic field (4) will eventually overcome the exchange energy at the interface and the FM will point in the direction of the applied field. However, if the field is reduced back down to a level at which this interfacial exchange energy is not overcome, then the spin will revert back to aligning with the AFM spins. The overall effect results in a magnetic hysteresis loop (Figure 52) that is shifted from the origin.

Exchange bias has been studied for over half a century. It was first discovered in 1956 by Meiklejohn and Bean through Co nanoparticles embedded in cobalt oxide.[37] Various material forms—nanoparticles, films and crystals—and a variety of techniques (SQUID, VSM, SMOKE, ferromagnetic resonance, torque magnetometry, neutron diffraction, MFM, Lorentz microscopy, Brillouin scattering, and magnetic dichroism) have all been used to gain insight into the details of the effect. Recently, there has been much interest in the electrical control of exchange bias. In principle, this is a simple extension of the work presented in the rest of this thesis. As depicted by Figure 53a, we have electrical control over the antiferromagnetism of BFO and some other multiferroics. We might combine this ME coupling with exchange

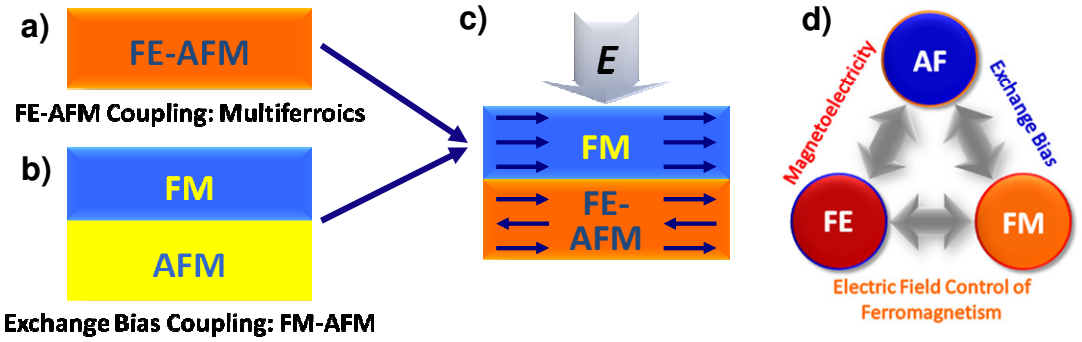

Figure 53 – Electric field control of exchange bias. Electric control of ferromagnetism (a) is combined with exchange bias between an antiferromagnet and a ferromagnet (b) to accomplish electric control of ferromagnetism (c). The different mechanisms and their relations can be visualized by (d).

coupling between an AFM and a FM (Figure 53b), resulting in electric control of ferromagnetism (Figure 53c-d). Since the magnetoelectric coupling of BFO occurs at room temperature, combination with a room temperature ferromagnet may result in an overall effect that could be used in devices without the need for cooling.

6.2 Interface Control

This combination of couplings is an ambitious plan; research has demonstrated that these two techniques—magnetoelectric and exchange coupling—work individually, but there is no guarantee that they can work cooperatively. The first step is to grow a high quality interface between a magnetoelectric with a ferromagnet of the appropriate critical temperatures (above room temperature). BFO is a clear choice since it is the only room temperature ferroelectric antiferromagnet. There are many possible choices for the ferromagnet. CoFe is one due to its favorable anisotropy and the multitude of studies that exist focusing on it. Figure 54a shows the heterostructure architecture. As in the previous work, BFO(001) was grown via PLD on top of a STO substrate with a SRO bottom

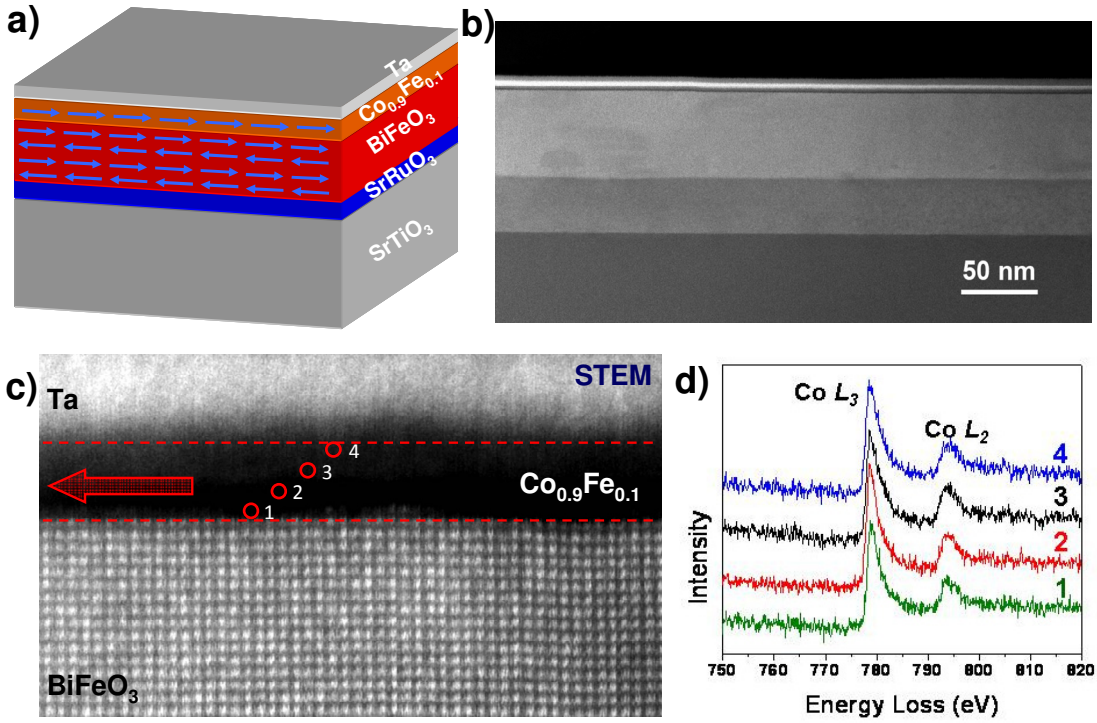

Figure 54 – Magnetoelectric exchange bias heterostructures and their interface. a) The materials and spin structure of the studied heterostructure. Low (b) and high (c) resolution TEM images of the samples. d) EELS measurement of the *L*-edge of cobalt.

electrode to force the ferroelectric variants of BFO to point along the downward pointing [11-1] directions. The CoFe and Ta films were then deposited via an *ex-situ* ion beam sputtering process in an ultra-high vacuum deposition system at Stanford University. The Ta layer serves as a capping layer to reduce any oxygen entering the ferromagnet from the surface of the heterostructure. Oxide could also come from the BFO layers, reducing the effectiveness of the coupling at the interface. As shown in Figure 54b-d, transmission electron microscopy (TEM) and electron energy loss spectroscopy (EELS) were performed to determine the quality of the interface. The low resolution TEM image (Figure 54b) revealed smooth interfaces throughout the heterostructure. The high resolution image (Figure 54c) allowed atomic resolution of the interface, and showed no evidence of interdiffusion between the CoFe and BFO layers. This lack of interdiffusion is considered to be important in achieving strong exchange interactions between layers.

EELS was used at various points throughout both the CoFe layer (Figure 54d) to confirm that there had been no oxidation of the CoFe film. Unlike traditional exchange bias systems, this heterostructure was not field cooled since this process resulted in significant interdiffusion. However, the application of a magnetic field during growth appears to have resulted in similar exchange behavior.[84]

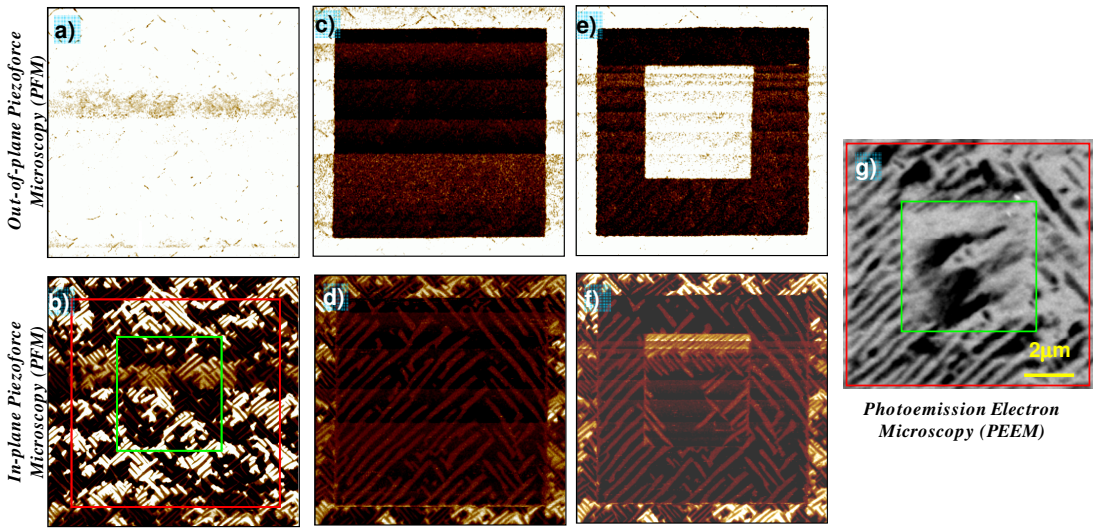

Figure 13 – PFM and PEEM images demonstrating coupling between BFO and CoFe. Out-of-plane and in-plane PFM images of a BFO thin film before poling (a-b), after poling (c-d), and after an additional poling (e-f) compared with a PEEM image taken at the Co *L*-edge (g).

6.3 Domain coupling between magnetoelectric BFO and ferromagnet CoFe

As completed in previously discussed BFO samples, the quality and ferroelectric domain structure of the BFO layer was established prior to metal growth [Qi] using a combination of atomic force microscopy and PFM and structural measurements. Figure 55a-b shows the out-of-plane (a) and in-plane (b) PFM images of a representative sample location of an as-grown BFO film. The white OOP image confirms that nearly all ferroelectric directions are pointing downward and the in-plane image reveals a

distribution of several in-plane ferroelectric directions. Figure 55c-d result from poling the red box out-of-plane, resulting in a solid brown OOP image within the poled area. Finally, a small area within the poled area was poled a second time in the opposite direction (Figure 55e-f). We know from our previous data that the antiferromagnetism of BFO follows these ferroelectric domains. By carefully marking the poled location, the same spot was found after growth of the metallic layers.[84]

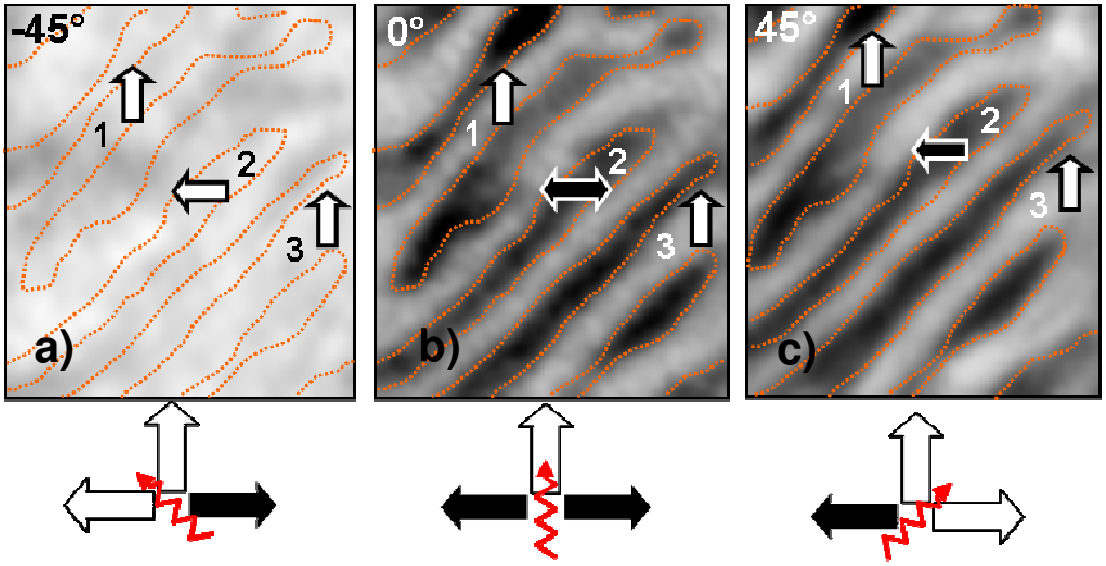

Figure 56 – PEEM determination of ferromagnetic directions. Co *L*-edge PEEM images of the CoFe layer at sample rotation angles of (a) α=-45°, (b) α=-0°, and (c) α=45°.

We observe in many samples that the CoFe magnetic domains (Figure 55g) taken by PEEM at the Co *L*-edge match quite nicely with the BFO ferroelectric domains, suggesting a coupling between the BFO domains and Co ferromagnetic domains. By rotating the sample 45 degrees in both directions and observing the change in PEEM contrast in images, the direction of the ferromagnetic domains can be determined. This rotation and determination of ferromagnetic directions is shown for a small section of Figure 55 in Figure 56. The domains with ferromagnetic directions along the direction of

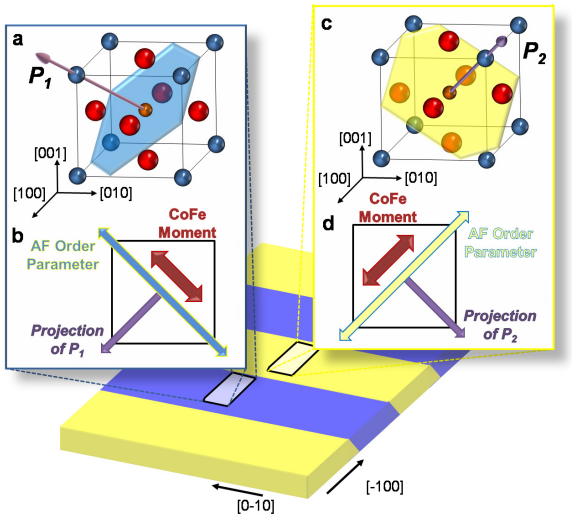

Figure 57 –Schematic diagrams of two adjacent domains (a,c) in the BFO(001) film, in which the [111] polarization directions as well as the perpendicular antiferromagnetic plane are identified as well as their projections onto the [001] surface and the corresponding M-directions in the CoFe layer (b,d).

the incoming x-rays (red arrows in Figure 56) have the largest intensity and therefore appear bright. Using this fact and the PFM images, we find that the ferromagnetic directions are aligned parallel with the AFM order parameter as illustrated in Figure 57. The choice of direction within the antiferromagnetic axis depends on the energetically preferable direction considering the domain walls and any field applied during growth of the ferromagnet.[84]

6.4 Horizontal Poling of BFO Domains

The next important question is whether these ferromagnetic domains can be changed if we were to apply the electric field after growth of the metallic layers. This question required a different approach since we cannot apply a vertical electric field through a top conducting layer. Due to this limitation, a horizontal poling process was developed. This new poling process made it necessary to first demonstrate a consistent poling process for BFO before adding metallic layers on top of it. Figure 58a-b illustrates the design idea behind our horizontal poling.

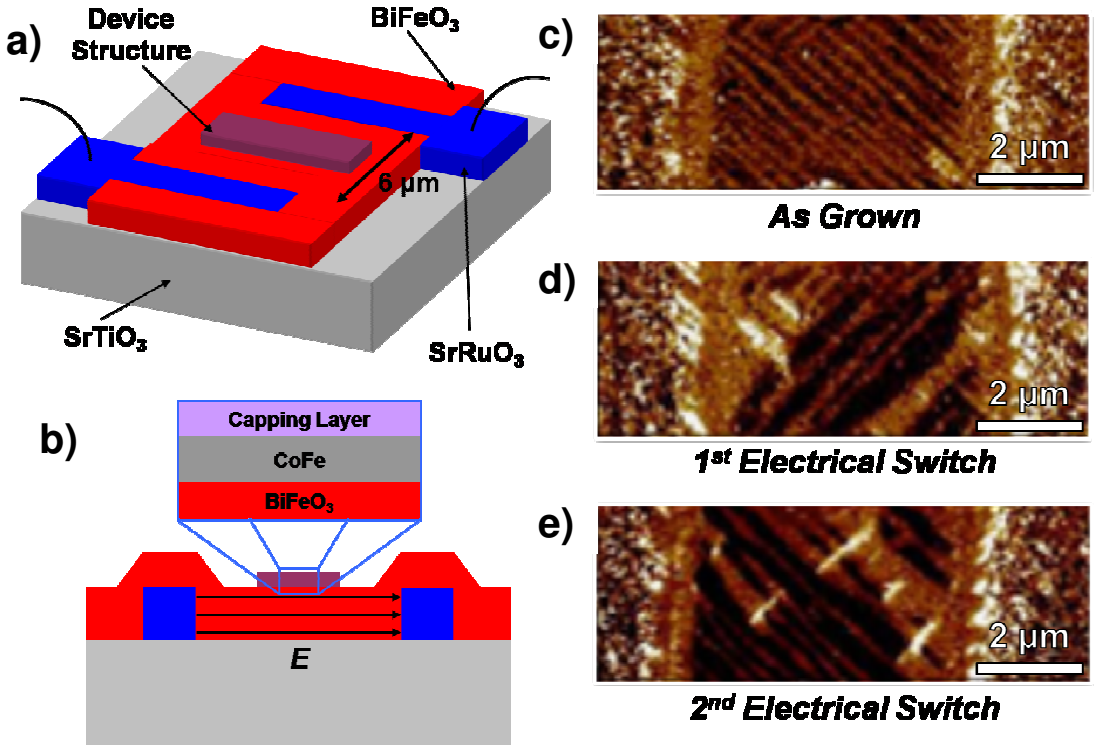

Figure 58 - Horizontal switching device structure. Three-dimensional (a) and cross-sectional (b) schematic diagrams of the coplanar epitaxial electrode device illustrating the structure that will enable controlled ferroelectric switching and electrical control of local ferromagnetism in the CoFe features. In-plane PFM images showing the ferroelectric domain structure for a device in the as-grown state (c), after the first electrical switch (d) and after the second electrical switch (e).

The bottom electrode SRO is grown in a manner consistent with previous samples; however, photolithography and ion milling is used to etch away most of the SRO, allowing the remainder to become our poling electrodes. 100-150 nm of BFO is then grown like a blanket on top of the SRO electrodes and space between. The metallic layers grown by ultra-high vacuum metal deposition as before are also taken through another round of photolithography and ion milling leaving behind only small stripes of CoFe on top of BFO and in between the SRO electrodes. This design allows us to change the BFO electrically and see what happens to the ferromagnetic on top.

The BFO domains in this architecture behave similarly to the BFO(001) domains previously discussed. Figure 58c illustrates that we get very nice controllable stripes that

make a 45 degree angle to the electrodes. This angle is actually due to the choice of aligning the electrodes along this direction. Rotation of the electrodes by 45 degrees resulted in unreliable control of both BFO and CoFe domains. The domains rotate by 90 degrees when poled with an electric field (Figure 58d). This process is also reversible when the electric field is applied along the opposite direction (Figure 58e). Thus, horizontal poling of BFO ferroelectric domains is controllable and reversible.[84]

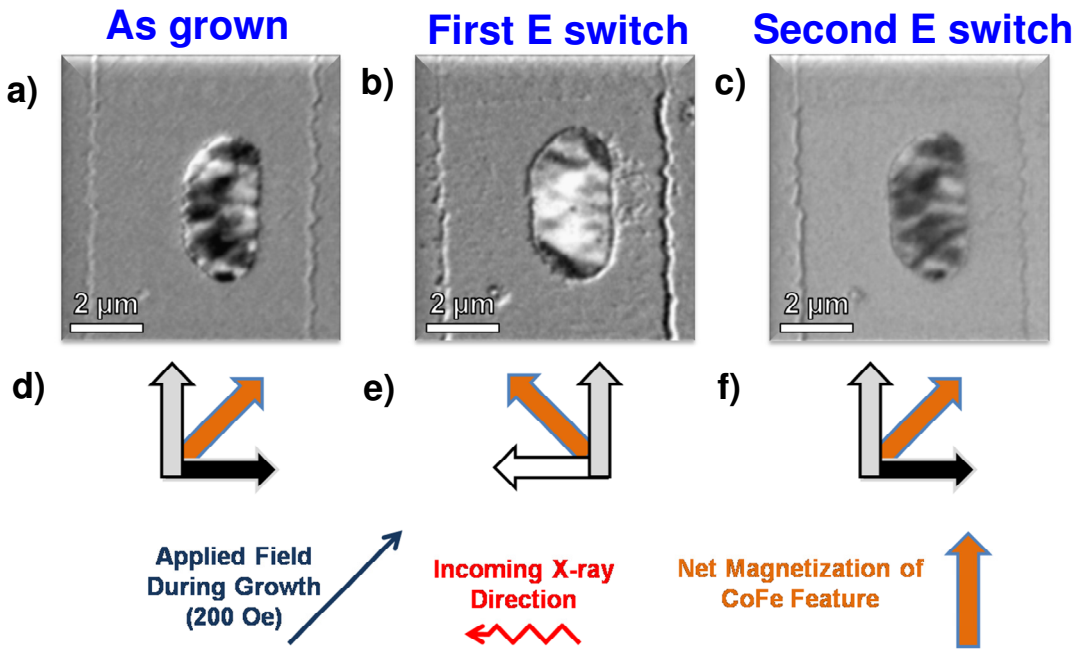

Figure 59 - Electrical control of local ferromagnetism. XMCD–PEEM images taken at the Co L-edge revealing the ferromagnetic domain structure of the CoFe features in the coplanar electrode device structure in the as-grown state (a), after the first electrical switch (b) and after the second electrical switch (c). Schematic descriptions of the observed magnetic contrast (grey, black and white) in the corresponding XMCD–PEEM images, respectively. Application of an electric field is found to rotate the next magnetization of the structures by 90° . The direction of the applied growth field and the incoming X-ray direction are labeled.

6.5 Electric Field Control of CoFe Ferromagnetism

Now that we are confident about our BFO processing, let us consider how the ferromagnetic domains change through this poling. The ovals in Figure 59a-c are the Co

stripes on top of BFO with the electrodes on the sides of the images. The variation of colors in the stripes represents the different ferromagnetic directions. In Figure 59a and 59d, the two as-grown ferromagnetic directions lie on either side of the applied magnetic field during growth of the ferromagnet, resulting in a net magnetization along the direction of applied field. When we apply an electric field across the electrodes, there is a clear change in the ferromagnetic domains. As demonstrated by the near reversal of contrast, the ferromagnetic directions and therefore net magnetization rotates by 90 degrees and rotates back after another poling in the opposite direction. Though admittedly not perfect, this is a demonstration of electrical control of ferromagnetism at room temperature.[84]

This is clearly a very exciting result, but there is still much more to determine. Why do the ferromagnetic domains not match the ferroelectric domains as in the vertical poling? What are the competing energies? For example, notice that the ferromagnetic domains do not always change on the ends of the metallic stripes. Why is there an apparent 180 degree reversal of some ferromagnetic domains and no change in others? Why would electrical control of an antiferromagnetic axis (which should have no preference between left or right) result in a change in the ferromagnetic direction? It seems likely that the picture is not as simple as magnetoelectric and then exchange coupling. It may very well be that strain mediates this effect, causing an imbalance between left and right directions. Many questions are left unanswered. Though clearly there is much room here for future work, it is important to point out that many questions also still remain in standard exchange bias even though the effect is a multi-billion dollar money maker in a wide

variety of applications. Perhaps this electrical control of ferromagnetism at room temperature can also be put to use well before intricacies are established, or this extra electric order parameter may allow a new perturbation of exchange bias that could unlock its mysteries.

Chapter 7: Summary of Results and Future Directions

7.1 Introduction

This thesis has focused on electric and strain control of antiferromagnetism, as well as ferromagnetism at room temperature through the use of multiferroic, magnetoelectric BFO films. Chapter 1 discussed what properties define a multiferroic and magnetoelectric material and touched on applications using these individual properties. BFO was introduced as a model system, being the only room temperature ferroelectric antiferromagnet. Finally, this chapter ended with a brief summary of the organization of this dissertation.

Though this work shows great promise for the use of BFO in practical applications, other magnetoelectrics should be considered. BFO has a clear advantage in being the only single phase room temperature ferroelectric antiferromagnet. However, the combination of two or more materials, such as a ferroelectric (like PZT) and a ferromagnet could result in a strong interfacial magnetoelectric effect and is a hot research area. In fact, it is possible that this could be achieved without the need of ferroelectric and magnetic layers. The appropriate use of strain and layering has resulted in thin film ferroelectrics (when the bulk material was not ferroelectric) and interfacial magnetism between non-magnetic materials. There is no reason to assume that such ideas could not also be used to create interfacial magnetoelectricity. Second harmonic generation, sensitive to both electric and magnetic fields at interfaces, would be a perfect tool to search for such behavior.

7.2 Techniques for Measurement

Chapter 2 gave the background required to understand the x-ray techniques used to study BFO in the rest of the thesis. Photoemission electron microscopy is a powerful technique that takes advantage of the sensitivity of x-ray absorption spectroscopy to excited states in materials. The dichroism effect observed in magnetic and ferroelectric materials is utilized in PEEM to image the domains. We use these domain images to study the control of magnetism in BFO in this research.

7.3 Electric Control of Antiferromagnetism in BFO

Chapter 3 began the discussion of the first experimental results in this work. A conceptual approach to electrically control of antiferromagnetism in BFO thin films was presented. PFM and PEEM images were compared to determine the effectiveness of this approach. The sensitivity of PEEM to ferroelectric domains and how one can separate this effect from the magnetic effect through temperature dependent measurements was addressed. Finally, this work was confirmed by electrical control of magnetism in BFO crystals by Lebeugle *et. al*. Though electric control has been proven for bulk and films greater than 100 nm, no conclusive result exists yet for thinner BFO films. This is largely due to the fact that the BFO domains get smaller with decreasing BFO thickness, eventually approaching the resolution limit of PEEM. As the resolution of PEEM improves, it would be interesting to study this coupling for ultrathin films where the ferroelectric and magnetic properties differ, as discussed in the next chapter.

7.4 Thickness Effect on Properties of BFO

Chapter 4 was a lengthy chapter representing the bulk of the effort in this research. Thin BFO films were observed to deviate from the behavior observed in bulk. Strain (via control of film thickness) was introduced as a method to further control (beyond the electric control presented in the last chapter) the magnetic properties of BFO. Though the measurements in the previous chapter were sufficient to demonstrate electric control of antiferromagnetism, the exact antiferromagnetic nature could not distinctly be determined. Much effort was taken to model the angular dependencies of many possible magnetic behaviors for BFO and determine the best experiment to distinguish between these possibilities. The ferroelectric contribution also had to be approximated to allow the correct angular dependencies. This ferroelectric research represents a large area for future research. PEEM imaging of ferroelectrics has not been largely investigated. Though the ferroelectric angular dependence appears to be similar to magnetic contributions, questions remain. For example, it is observed that polarization domains pointing out of the sample versus into it result in dramatically different PEEM contrast, despite being a difference of 180 degrees. In magnetic contrast, a change of 180 degrees cannot be determined through linear dichroism measurements.

An approximate formula for the angular dependence of PEEM contrast in a multiferroic was created and used to distinguish a preferred [112]-type magnetic axis in BFO thin films, as opposed to the easy magnetic plane seen in bulk. It is important to note that the

concepts behind this formula can be used not only for other multiferroics but also for other materials with more than one angle- or temperature-dependent contribution to linear dichroism. This formulation is particularly important when it has recently been discovered[85] that crystallographic directions play a significant role in x-ray absorption measurements. It should be noted, however, that though dichroism images are derived from x-ray absorption spectroscopy, the division of images and comparison of domains with the same crystallographic contributions in PEEM can result in a cancellation of some components.

Finally, Chapter 4 investigated the change of ferroelectric and magnetic properties in ultathin films with film thickness less than 20 nm. The ferroelectric and magnetic properties weaken as the film thickness becomes quite small, an effect found by both PFM and XAS. This observation is in agreement and correlates well with the reduction of exchange bias seen in ferromagnets on very thin antiferromagnets.

7.5 Orientation Effects on the Ferroelectric and Magnetic Properties of BFO

Chapter 5 studied the differences in ferroelectric and magnetic properties between different orientations of BFO thin films. 110 and 111 orientations were introduced as alternatives to the 001 structure discussed throughout the rest of the thesis. Thick BFO(110) films show easy plane behavior as opposed to <112> axes selected in thin films. BFO(111) films reveal no dichroism but variation in PEEM images, meaning easy

plane behavior for all thicknesses. No preferred axis is selected in this orientation since the strain is applied symmetrically across the perpendicular magnetic plane.

7.6 Exchange Bias with BFO

Chapter 6 utilized the knowledge from the previous chapters to establish electric control of ferromagnetism. This was accomplished through a combination of magnetoelectric coupling and exchange bias. The growth of high-quality films allowed strong coupling between BFO domains and the ferromagnetic domains of CoFe. A horiztonal poling device was created in order to observe the effect on a top layer of CoFe when BFO was electrically pole underneath. A near-reversal of ferromagnetic domains was observed, providing strong evidence for the possibility of electrical control of ferromagnetism at room temperature—the goal of this thesis.

There are many ways this electrically assisted exchange bias research could be enhanced. For example, other ferromagnetic materials should be studied to find the most efficient control. Pure Co was attempted with little success. However, some believe better coupling could be achieved with an oxide such as LSMO. Both BFO and LSMO have perovskite structures and could be grown in-situ to get epitaxial structure, and therefore have the advantage of maintaining the chemical structure across the interface. One could expect that such heterostructure has stronger exchange interaction than the amorphous BFO/CoFe structure. Moreover, since the dramatic physics properties of both BFO (multiferroic) and LSMO (well-known colossal magnetoresistance oxide) are well

studied, the interaction between these two materials will involve spin and orbital orders and will likely result in fascinating physics.

The mechanisms and magnitudes of competing energies most relevant in electric exchange bias are not known. For instance, shape anisotropy was considered by varying the length to width ratio of the CoFe stripes. The only clear result of this study was that domain wall pinning was more common on the short edges of each stripe. Why? What other energies are most important? Is the electric control just the result of magnetoelectric coupling and exchange bias, or is there a mediating effect such as strain?

7.7 Overall Summary

Electric and strain control of antiferromagnetism and ferromagnetism at room temperature using magnetoelectric BFO thin films has been demonstrated and modeled. PFM and PEEM techniques were used to correlate ferroelectric and antiferromagnetic domains. A formula was established and applied to determine magnetic behavior. The effect of thickness and orientation on ferroelectric and magnetic properties was studied. Finally, this knowledge was used in the making of a magnetoelectric-ferromagnetic heterostructure in which electrically-assisted exchange bias was observed. This toolbox of control parameters gives us a very strong benefit for the making of new and improved devices, particularly in the computing industry where the traditional magnetic field controlled devices are reaching their limits.

Appendix A: Growth of Epitaxial BFO Thin Films

Epitaxial growth is the extended single-crystal film formation on top of a crystalline substrate. High quality epitaxial growth has only recently become a common practice and has allowed significant improvement in computing and other device functionality. Although there are many methods that allow high quality film growth, nearly all films in this research were obtained by pulsed laser deposition. In PLD, a laser shines onto a target powder that that has all of the atoms desired for the final film. The laser creates a highly directional plume of atoms that deposit on a substrate that can be heated in a gaseous environment. The combination of temperature and gas pressure control allows for a wide range of thermodynamic conditions. The majority of the BFO films in this study were grown using PLD at 700°C in 100 mTorr partial pressure of oxygen and then cooled at 5°C/minute to room temperature in 760 Torr pressure of oxygen. XRD measurements allowed measurements of lattice constants and verified that the films were single phase. Before growth of the BFO layer, a SRO layer is deposited on a high quality single crystal heterostructure (typically STO or DSO due to their close lattice match with BFO). The SRO layer serves to break the energy degeneracy between the different ferroelectric directions. In BFO(001) films, this results in only four downward pointing ferroelectric directions instead of all eight possible directions. The degeneracy between the four directions can be further broken by growing on a miscut substate. Since a miscut substrate is not flat, but instead slants at a small angle, the BFO ferroelectric direction pointing along the miscut will be present in a monodomain film. A miscut in-between two ferroelectric directions will result in a film with two ferroelectric directions, creating a stripe domain pattern.

Appendix B: Piezoelectric Force Microscopy

Piezoelectric force microscopy measures both the out of plane force and the torque on the PFM tip when the tip has an oscillating voltage applied to it.[10-11] The out of plane mode will determines whether the material one of the four up- or downward pointing body diagonal directions. The in plane mode distinguishes between these four directions. By comparing these two modes, one can distinguish which polarization direction is present.[12] For example, Figure 60 shows the out of plane (a and c) and in-plane (b and d) PFM images before (a and b) and after (c and d) applying an external electric field of 12 V. The cantilever tip comes in from the right of the images. In the in-plane images, the colors black, white and brown represent whether the cantilever tip is torqued right, left or not horizontally. This color determines the in plane direction of the polarization. The white color in Figure 60a, demonstrates that only downward pointing ferroelectric directions are present before poling, but the application of the external electric field results in only upward (black) pointing

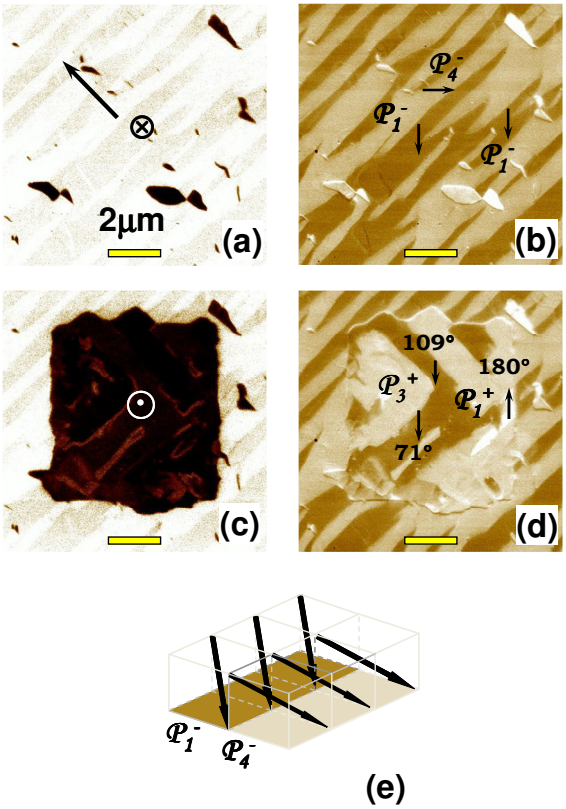

Figure 60 - Out-of-plane (a) and in-plane (b) PFM images of the as-grown BFO film. Out-of-plane (c) and in-plane (d) PFM images taken after applying an electric field perpendicular to the film on the same area as in a and b. Different polarization switching mechanisms are shown by the arrows in (d). A side view of two observed ferroelectric variants (e).

ferroelectric directions within the poled box. The arrows in Figure 60d indicate new in-plane polarization directions after ferroelectric switching. Different polarization switching mechanisms (71°, 109° and 180°) are labeled in Figure 60d. Figure 60e illustrates the side view of two predominant polarization directions in this film.

REFERENCES

1. H.-U. Habermeier, *Materials Today* **10** (10), 34 (2007).
2. E. Dagotta, *Science* **309**, 257 (2005).
3. Y. Tokura and N. Nagosa, *Science* **288**, 462 (2000).
4. W. Känzig, "Ferroelectrics and Antiferroelectrics". in Frederick Seitz, T. P. Das, David Turnbull, E.L. Hahn, *Solid State Physics*. **4**. Academic Press. p. 5. (1957).
5. M. Lines and A. Glass, *Principles and applications of ferroelectrics and related materials*. Clarendon Press, Oxford (1979).
6. K. Aizu, Phys. Rev. B **2**, 754 (1970).
7. J.F. Scott, *Ferroelectric Memories*. Springer (2000).
8. M. Dawber, K.M. Rabe, and J.F. Scott, *Reviews of Modern Physics* **77**: 1083 (2005).
9. S.V. Kiselev, *et al.*, *Soviet Phys.-Doklady* **7**:742-744 (1963).
10. P. Günther, *et al.*, *Appl. Phys. Lett*. **61**, 1137 (1992).
11. A. Gruverman, *et al.*, *Annu. Rev. Mater. Sci*. **28**, 101 (1998).
12. F. Zavaliche, *et al.*, *Phase Transit*. **79**, 991 (2006).
13. L. Fritsche and B. Weimert, *Phys. Stat. Sol. B* **208**, 287 (1998).
14. C. Ederer and N. Spaldin, *Phys. Rev. B* **95,** 224103 (2005).
15. R. Ramesh, *et al., Nature Mater*. **6**, 21 (2007).
16. S.-W. Cheong, *et al., Nature Mater*. **6**, 13 (2007).
17. N.A. Hill, *J. Phys. Chem. B* **104**, 6694 (2000).
18. M. Fiebig, *J. Phys. D Appl Phys*. **38** R1123 (2005).
19. W. Eerenstein, *et al.*, *Nature* **442**, 759 (2006).
20. V.E. Wood and A.E. Austin, *et al.*, *Int. J. Magn*. **5**, 303 (1973).

21. G.C. Baldwin, *Physics Today* **28** (1), 9 (1975).

22. J. Stohr and S. Anders, *IBM J. Res. Develop*. **44** (4), 535 (2000).

23. E. Brüche, *Z. Phys*. **86**, 448 (1933).

24. G. Schonhense, *J.Phys.: Condens. Matter* **11**, 9517-9547 (1999).

25. E. Bauer, *J. Phys. Cond*. Mat. **13**, 11391 (2001).

26. B.P. Tonner and G.R. Harp, *Rev. Sci. Instrum.* **59**, 853 (1988).

27. W. Engel, *et al*., *Ultramicroscopy* **36**, 148 (1991).

28. S. Anders et al., *Rev. of Sci Inst*, **70**, 10 (1999).

29. G. van der Laan and B. T. Thole, *Phys. Rev. B* **43**, 13401 (1991).

30. B.T. Thole, et al., *Phys .Rev. Lett.* **68** 1943 (1992).

31. J. Stohr, *J. Magn. Magn. Mater.* **200**, 470 (1999).

32. H. Ohldag, et al., *J. Elec. Spect. Rel Phen*., **114**, 765 (2001).

33. F.U. Hillebrecht, et al., *Phys Rev. Lett*., **86**, 152878 (2001).

34. A. Scholl, et al, *Science* **287,** 1014 (2000).

35. D. Spanke, et al., *Phys. Rev. B* **58**, 5201 (1998).

36. J. Stohr, *Phys. Rev. Lett*., **83**, 1862 (1999).

37. J. Nogues, *J. Magn. Magn. Mater*. **192**, 203 (1999).

38. M. Kiwi, *J. Magn. Magn. Mater*. **234**, 584 (2001).

39. J.C.S. Kools, *IEEE Trans. Magn*. **32**, 3165 (1996).

40. N. Smith, "Science with Soft X-rays," *Physics Today*, January (2001).

41. H. Ohldag, *Phys. Rev. Lett*. **87** 247201 (2001).

42. H. Ohldag, *Appl. Phys.Lett*. **76**, 2928 (2000).

43. K. Takano, et al*., Phys. Rev. Lett*. **78**, 1130 (1997).

44. N.C. Koon, *Phys. Rev. Lett*. **78**, 4865 (1997).

45. T.C. Schulthess, *Phys. Rev. Lett*. **81**, 4516 (1998).

46. P. Miltenyi, et al., , *Phys. Rev. Lett.* **84**, 4224 (2000).

47. T. Zhao, *et al*., *Nature Mat.* **5**, 825 (2005).

48. W.-C. Yang, *et. al.*, *Appl Phys. Lett.* **85** (12), 2316 (2004).

49. C. Ederer and N. Spaldin, *Phys. Rev. Lett.* **95,** 257601 (2005).

50. R.R. Das, *et al*., *Appl. Phys. Lett.* **88,** 242904 (2006).

51. M. Fiebig, *et al*., *Nature* **419,** 818 (2002).

52. J. Dho, *et al*., *Adv. Mater.* **18,** 1445–1448 (2006).

53. D. Lebeugle, *et. al*., *Phys. Rev. Lett*. **100**, 227602 (2007).

54. S. V. Kiselev, R. P. Ozerov, and G. S. Zhdanov, *Sov. Phys. Dokl*. **7**, 742 (1963).

55. J. R. Teague, R. Gerson, and W. J. James, *Solid State Commun*. **8**, 1073 (1970).

56. I. Sosnowska, *et al.*, *J. Phys. C* **15**, 4835 (1982).

57. S. Lee, *et al.*, *Phys. Rev. B* **78**, 100101(R) (2008).

58. B. Ruette, *et. al*., *Phys. Rev. B* **69**, 064114 (2004).

59. C. Tabares-Munoz, *et al*., *Ferroelectrics* **55**, 235-238 (1984).

60. Y.F. Popov, *et. al., Low Temperature Physics* **27** (4), 478 (2001).

61. J. Wang et. al., *Science* **299** 1719 (2003).

62. Q. Jiang and J.H. Qui, *J. of Appl. Phys*. **99**, 103901 (2006).

63. D.G. Schlom, *et. al., Annu. Rev. Mater. Res.* **37**, 589 (2007).

64. Y.H. Chu, *et al*., *Appl. Phys. Lett*. **90**, 252906 (2007).

65. C. Ternon, *et al*., *Thin Solid Films* **515** (2), 481 (2006).

66. A.J. Millis, *et al*., *J. of Appl. Phys.* **83** (3):1588-1591 (1998).

67. T. Yamada, *J. Phys. Soc. Jpn.* **21**, 664 (1966).

68. A.K. Zvezdin, *et al*., *Jour. of Magnetism and Magnetic Mat.* **300** (1), 224 (2006).

69. M.B. Holcomb, *et al*.,*Phys. Rev. B*, in revision (2009).

70. J. Stohr and H.C. Siegmann, *Magnetism From Fundamentals to Nanoscale Dynamics* (Springer: New York, 2006).

71. T. Tsuboi, *Phys. Rev. B* **39**, 2842 (1989).

72. A. Gruverman, *et al.*, *Annu. Rev. Mater. Sci*. **28**, 101 (1998).

73. A. Scholl, *et al.*, *Rev. Of Sci. Instr*. **73** (3), 1362 (2002).

74. T. Ambrose and C.L. Chien, *Phys. Rev. Lett.* **76**(10), 1743 (1996).

75. J.W. Seo, *et al*., (2008) *J. Phys. Cond. Mat.* **20**, 264014 (2008).

76. N. Setter, *et al*., *J. of Appl. Phys.* **100**, 051606 (2006).

77. M. Huijben, *et al*., *Phys. Rev. B* **78**, 094413 (2008).

78. G. Xu, J. Li, and D. Viehland, *Appl. Phys. Lett.* **89**, 222901 (2006).

79. J. Lüning, *et al*.,, *Phys. Rev. B* **67**, 214433 (2003).

80. M. Ohkoshi, *et al.*, *IEEE Transl. J. Magn. Jpn*. **1**, 37 (1985).

81. A. A. Glazer, *et al.*, *Sov. Phys. JETP Lett*. **15**, 259 (1972).

82. F. S. Lubrosky, *Electro-Technology*, 102 (Sept. 1962).

83. M. Kirschner, http://magnet.atp.tuwien.ac.at/gallery/exchbias/intuitive.html

84. Y. H. Chu, *et al*., *Nat. Mat.,* **7** (6) 478 (2008).

85. E. Arenholz, *et al*., *Phys. Rev. B* **74**, 094407 (2006).